University of Stuttgart
Institute of Nuclear Technology
and Energy Systems

Analytical Investigations on a Core Catcher Concept for Ex-vessel Melt Retention by Water Injection through Porous Concrete from Below

Özlem Yılmaz

December 2022 IKE 2-169

University of Stuttgart
Institute of Nuclear Technology
and Energy Systems

Analytical Investigations on a Core Catcher Concept for Ex-vessel Melt Retention by Water Injection through Porous Concrete from Below

von der Fakultät Energie-, Verfahrens- und Biotechnik der Universität Stuttgart zur Erlangung der Würde eines Doktor-Ingenieurs (Dr.-Ing.) genehmigte Abhandlung

vorgelegt von

Özlem Yılmaz

geboren in Fatih, Türkei

Hauptberichter: Prof. Dr.-Ing. Jörg Starflinger
Mitberichter: Prof. Dr.-Ing. Marco K. Koch

Tag der Einreichung: 16.05.2022
Tag der mündlichen Prüfung: 01.12.2022

ISSN – 0173 – 6892

December 2022 **IKE 2-169**

Erklärung über die Eigenständigkeit der Dissertation

Ich versichere, dass ich die vorliegende Arbeit mit dem Titel

„Analytical Investigations on a Core Catcher Concept for Ex-vessel Melt Retention by Water Injection through Porous Concrete from Below"

selbstständig verfasst und keine anderen als die angegebenen Quellen und Hilfsmittel benutzt habe; aus fremden Quellen entnommene Passagen und Gedanken sind als solche kenntlich gemacht.

Declaration of Authorship

I hereby certify that the dissertation with the title

„Analytical Investigations on a Core Catcher Concept for Ex-vessel Melt Retention by Water Injection through Porous Concrete from Below"

is entirely my own work except where otherwise indicated. Passages and ideas from other sources have been clearly indicated.

Böblingen, 15.05.2022 Özlem Yılmaz

Acknowledgments

Creating this work has been a great experience and during this time I have gained a very valuable new perspective not only on science but also on life, which I will always cherish. At this point, I would like to take the opportunity to thank all those people who have given me their time and energy along the way, and made this work possible.

First and foremost, I would like to express my deepest gratitude to my doctoral supervisor, Prof. Jörg Starflinger, for the opportunity to work on this highly interesting topic. During the course of my research and writing, he has provided a great work environment with his kind supervision, and contributed to this work with his valuable advice. I will always be grateful for his continuous guidance and encouragement throughout the years.

I would like to extend my sincere thanks to my co-examiner Prof. Marco K. Koch and the chair of my exam Prof. Stefan Weihe for their time and interest in my work. I am thankful to both of them for the valuable discussions and their friendly manner.

I am extremely grateful to Dr. Michael Buck for his valuable support and patience. His immense knowledge in the field helped me to not only to overcome the problems during my research but also to be better at critical thinking. I certainly have learned a lot from him during long hours of discussions at the institute and I am very thankful to him for this. I also would like to thank Georg Pohlner for his support and helpful discussions especially at the initial phase of my research.

This work has been performed with the financial help of the French government through the "Programme d'Investissement d'Avenir" within a project co-funded by CEA, EDF and AREVA. I would like to extend my gratitude to them for funding my research and their support. In particular, I would like to thank Dr. Christophe Journeau for the insightful discussions.

I also would like to thank the Research Institute of Nuclear Technology and Energy Conversion for the scholarship that financed the final stage of my research.

I would like to thank sincerely Prof. Eckart Laurien and Dr. Rudi Kulenovic for the very valuable discussions and advice as I was working on the experimental part of my work. In this context, I also would like to thank the whole laboratory team of the Institute of Nuclear Technologies and Energy Systems for their support during experiment set-up, and to Dennis Barbarossa for his contribution to measurements within the framework of his Bachelor Thesis.

I would like to thank all current and previous staff of the severe accident research group at the Karlsruhe Institute of Technology, in particular: Beatrix Fluhrer, Thomas Cron, Dr. Alexei Miassoedov, Dr. Jerzy Foit, for providing the samples that I have used in my work, and all the valuable information on the COMET and CometPC research and experiment data.

I am very thankful to all current and previous staff of the Institute of Nuclear Technology and Energy Systems, especially to my fellow doctoral students, for their support and the great work environment. I am very grateful for the friendships we have built over the years and will always cherish the time we have had during and after work.

My very special thanks go to my beloved partner, Martin Bauer, for always being there for me, his tireless emotional support and being my rock during the most challenging times. I am very grateful for his kindness and love.

Last but most certainly not least, my heartfelt gratitude goes to my parents, Müzeyyen and Sabahattin Yılmaz. Their love, support and belief in me enabled me to go beyond borders (literally and figuratively) pursuing my education and what I want in life. None of my achievements would have been possible without them.

Abstract

The aim of this work is to investigate important aspects of ex-vessel molten corium cooling by bottom flooding through a porous concrete core catcher. These are the transport of cooling water through the porous concrete to the melt and the fragmentation and porosity formation in the melt due to the interaction with cooling water/steam.

Firstly, this work investigates the hydraulic parameters of the porous concrete core catcher. Cooling water flow simulations are performed by means of the code COCOMO3D for the passive distribution of the cooling water into the melt layer from below with sufficient flow rates over the large reactor cavity. These investigations show that the permeability values of two different layers of the porous concrete and their relation to one another have a significant effect on the rising superficial velocity of the cooling water and on the required pressure head for the coolant supply. A methodology is developed in this work in order to optimize the core catcher for hydraulic properties, which can be applied to various boundary conditions. Based on this methodology, for the inlet configuration that provides the cooling water around to the core catcher over the whole perimeter, various concrete pairings can be chosen to provide sufficient cooling water into the molten corium uniformly, with a feasible pressure head.

Due to the restrictions on the design for back fitting, in these cases the water supply can be provided to the core catcher only from a very small inlet connection. Thus, very high velocities of cooling water are expected around the inlet region, and the linear friction laws are not adequate anymore. To gather the needed data for improving the modelling a dedicated experiment set-up is built within the framework of this work, and the relation between pressure and superficial velocity of water for porous concrete samples from CometPC core catcher, which are provided by KIT, is measured. The falling head method is used which enables the measurements for a wide range of pressure values. The non-linear friction law with the values for permeability and passability obtained from the measurements is then implemented into COCOMO3D. The simulations are performed for restricted water inlet case with the quadratic friction law for porous concretes. These simulations show that back fitting of the porous concrete core catcher device with limited water inlet configuration can raise many challenges. Increasing the area of the water inlet

and providing the water uniformly from the perimeter of the porous core catcher device is the more feasible approach for the reactor application.

Finally, the fragmentation and porosity formation phenomenon caused by bottom flooding is modelled in this work. The initial molten corium-steam interaction is assumed as the decisive phenomenon having a lasting effect on the fragmentation. Therefore, the fragmentation is modelled as a void fraction modeling of the two-phase flow of molten corium and steam in thermal equilibrium. In order to simulate this two-phase flow a new model for the interfacial friction force for molten corium-steam two-phase flow has been necessary. A new Bubbly-Channel two-phase flow interfacial friction force model is developed in this work in order to model the porosity formation during corium cooling by bottom flooding.

With a stand-alone simulation program, this new model is validated against the COMET and CometPC experiments with varying boundary conditions and material properties. The results show very good agreement with the final porosity range achieved in the experiments. The new interfacial friction model and the material properties of liquid corium are implemented into COCOMO3D code. The COCOMO3D simulations of two-phase flow of molten corium and steam are performed for CometPC plus experiment data. The flow pattern of steam and melt during these simulations shows good replication of the post-test morphology of solidified porous thermite from the experiments as well as the dispersion and ejection that happened during the experiment. Two further cases are simulated for the reactor case, which show that the partial ablation of the sacrificial concrete between core catcher and molten corium has an effect on the coolant distribution in the compact melt layer.

These investigations show that being able to simulate molten corium as a moving liquid, due to the new model, provides more realistic modelling of coolant ingression into the compact melt layer via bottom flooding and the space that coolant actually occupies, hence the fragmentation phenomenon. The two-phase flow modelling of molten corium and steam presented in this work can be extended further in the future to three-phase flow of molten corium-steam-water with evaporation phenomenon in order to model the entire cooling and solidification process by bottom cooling.

Kurzfassung

Ziel der Arbeit ist die Untersuchung der wesentlichen Aspekte bei der Kühlung einer Kernschmelze in der Ex-Vessel-Phase durch Flutung von unten in einem Core Catcher aus porösem Beton. Diese sind der Transport von Kühlwasser durch den porösen Beton zur Schmelze und die Fragmentierung und Porositätsbildung der Schmelze aufgrund der Wechselwirkung mit Kühlwasser/Dampf.

Zunächst werden die wichtigsten hydraulischen Parameter des Core Catchers aus porösem Beton untersucht. Mit Hilfe des Computercodes COCOMO3D wird die passive Verteilung des Kühlwassers und die Zufuhr zur Schmelze in ausreichender Rate über die ganze Reaktorgrube hinweg simuliert. Dies zeigt, dass die Permeabilitätswerte der beiden Schichten porösen Betons und ihr Verhältnis zueinander ein entscheidender Faktor für die Lehrrohrgeschwindigkeit des aufsteigenden Kühlwassers und des benötigten Überdrucks für die Zuführung des Kühlwassers sind. Es wird eine Methodologie entwickelt, um die hydraulischen Eigenschaften des Core Catchers für verschiedene Randbedingungen zu optimieren. Basierend darauf können für eine Einlasskonfiguration mit Kühlwasserzufuhr von allen Seiten verschiede Paarungen von Betonarten ausgewählt werden, um eine Kühlwasserzufuhr zur Schmelze in ausreichender Menge und Uniformität bei einem realisierbaren Überdruck zu ermöglichen.

Im Falle der Nachrüstung eines Core Catchers ist das mögliche Design der Wasserzufuhr sehr eingeschränkt und die Zufuhr kann nur über eine sehr kleine Einlassfläche erfolgen. Daher sind sehr hohe Strömungsgeschwindigkeiten in der Nähe des Einlasses zu erwarten und lineare Reibungsmodelle sind nicht mehr ausreichend. Um die benötigen Daten für eine verbesserte Modellierung zu gewinnen wird im Rahmen dieser Arbeit ein Experiment aufgebaut und für vom KIT zur Verfügung gestellte Proben aus porösem Beton des Core Catchers aus dem CometPC-Experiment die Abhängigkeit der Lehrrohrgeschwindigkeit vom Druck bestimmt. Für diese Messung wird die sog. “Falling Head”-Methode benutzt, die die Messung über einen großen Druckbereich hinweg ermöglicht. Das nichtlineare Reibungsmodell mit den aus den Messungen gewonnen Werten für Permeabilität und Durchgängigkeit wird dann in COCOMO3D implementiert. Damit wird der Fall eines auf eine kleine Fläche beschränkten Einlasses mit dem quadratischen

Reibungsgesetz für porösen Beton simuliert. Die Ergebnisse zeigen, dass die Nachrüstung eines Core Catchers aus Beton mit begrenzter Wassereinlassgeometrie problematisch sein kann. Eine Erhöhung der Fläche des Wassereinlasses und die Wasserzufuhr über den ganzen Umfang des porösen Core Catchers ist ein besserer Ansatz für eine Anwendung in einem Kraftwerk.

Schließlich wird in dieser Arbeit das Phänomen der Fragmentierung der Schmelze und der Bildung der Porosität aufgrund des Flutens von unten modelliert. Die anfängliche Wechselwirkung zwischen Corium und Dampf wird als entscheidendes Phänomen mit nachhaltiger Auswirkung auf die Fragmentierung angenommen. Somit wird die Fragmentierung als Blasenanteil der Zweiphasenströmung aus Dampf und geschmolzenem Corium im thermischen Gleichgewicht modelliert. Die Simulation dieser Zweiphasenströmung macht ein neues Modell für die Grenzflächenreibung erforderlich. Ein neues „Bubbly Channel"-Modell für die Grenzflächenreibung wird in dieser Arbeit entwickelt um die Porositätsbildung bei der Kühlung von Corium bei Flutung von unten zu modellieren.

Mit einem Stand-Alone Simlutionsprogramm wird dieses neue Modell gegen COMET- und CometPC-Experimente mit verschiedenen Randbedingungen und Materialeigenschaften validiert. Die Ergebnisse zeigen eine sehr gute Übereinstimmung mit dem in den Experimenten gefundenen Porositätsbereich. Das neue Modell für Grenzflächenreibung und die Materialeigenschaften von flüssigem Corium werden dann in COCOMO3D implementiert. COCOMO3D-Simulationen der Zweiphasenströmung von geschmolzenem Corium und Dampf werden für die Bedingungen im CometPC plus-Experiment durchgeführt. Die in den Simulationen auftretenden Strömungsmuster geben die im Experiment gefundene Morphologie des erstarrten, porösen Thermits gut wieder. Auch die im Experiment aufgetretene Dispersion und Auswurf von Schmelze wird von der Simulation wiedergegeben. Zwei weitere Fälle werden simuliert, um den Anwendungsfall im Kraftwerk zu untersuchen. Diese zeigen, dass eine nicht vollständige Ablation von Opferbeton zwischen Core Catcher und geschmolzenem Corium Einfluss auf die Verteilung des Kühlwassers in der kompakten Schmelzeschicht hat.

Diese Untersuchungen zeigen, dass die aufgrund des neuen Modells mögliche Simulation von geschmolzenem Corium als sich bewegendes Fluid eine realistischere Modellierung der Phänomene beim Eindringen von Kühlwasser in eine kompakte Schmelzeschicht beim Fluten von unten und der Bestimmung des tatsächlich vom Kühlmittel eingenommenen Raums, und damit letztendlich des Phänomens der Fragmentierung ermöglicht. Die in dieser Arbeit vorgestellte Modellierung von Corium und Dampf als Zweiphasenströmung kann in der Zukunft auf eine Dreiphasenströmung von Corium, Wasser und Dampf mit Verdampfung erweitert werden, um so den ganzen Prozess von Kühlung und Verfestigung der Schmelze bei der Kühlung durch Fluten von unten zu modellieren.

Table of Contents

List of Tables

List of Figures

Nomenclature

Latin Symbols

A	[m²]	Cross-sectional area in flow direction
A_c	[m²]	Surface area of the core catcher
A_d	[m²]	Cross-sectional area of a typical particle in dispersed phase (bubble or droplet)
C_D	[-]	Drag coefficient
C_0	[-]	Distribution parameter
$c_1, c_2, c_3,$	[-]	Coefficients for polynomial fit
d	[m]	Diameter
d_c	[m]	Diameter of the core catcher
D_p	[m]	Characteristic diameter of aggregates in porous media
F	[kg/m²s²]	Interfacial friction force per unit volume
f_f	[Pa/m]	Pressure loss due to friction per unit length
f_{mst}	[-]	Interfacial friction coefficient for channel flow
g	[m/s²]	Gravitational force
h	[m]	Height
h_l	[m]	Height of the lower layer of core catcher
h_s	[m]	Height of the sacrificial concrete
h_u	[m]	Height of the upper layer of core catcher
h_w	[m]	Height of the water inlet opening on the side of the core catcher
j	[m/s]	Superficial velocity
K	[kg/m³s]	Friction factor for the interfacial friction force

k	[m²]	Permeability
m_w	[kg/s]	Mass flow rate of the cooling water for COCOMO3D simulations
N_{Re}	[-]	Reynold number for the multi-particle system
p	[Pa]	Pressure
p_{atm}	[Pa]	Atmospheric pressure
p_{dif}	[bar]	Measured differential pressure
$p_{hyd,c}$	[Pa]	Hydrostatic pressure of liquid corium layer
p_{rel}	[bar]	Measured relative pressure
p_{sys}	[Pa]	System pressure
p_f	[Pa]	Pressure loss due to friction
q	[-]	Ratio of gas phase velocities in different flow regions
u		Uncertainty
r_c	[m]	Radius of the core catcher
r_d	[m]	Characteristic radius of a particle in dispersed phase (bubble or droplet)
t	[s]	Time
V	[m³]	Volume
$\dot{V}$	[m³/s]	Volumetric flow rate
v	[m/s]	Velocity
V_d	[m³]	Volume of a typical particle in dispersed phase (bubble or droplet)
v_r	[m/s]	Relative velocity in two-phase flow
V_{gj}	[m/s]	Average local draft velocity
X		Measured value
Y		Parameters dependent on the measured value
z	[m]	Position on axial direction (elevation)
Z	[-]	Weighing coefficient

Greek Symbols

α	[-]	Void fraction
ε	[-]	Porosity
η	[1/m]	Passability
K_k	[m/s]	Fluid conductivity (of a porous medium)
μ	[kg/ms]	Dynamic viscosity
μ_{mix}	[kg/ms]	Mixture viscosity for two-phase flow
ρ	[kg/m^3]	Density
φ	[kg/m^{2}s]	Mass flux

Superscripts and Subscripts

0, 1	Arbitrary positions
a, b	Arbitrary positions
bb	Bubbly flow region
c	For continuous phase of two-phase flow
ch	Channel flow region
ct	Churn turbulent flow region
D	Drag
d	For dispersed phase of two-phase flow
dt	Droplet flow region
f	Fluid
g	Gas
gl	Gas-liquid interface
gs	Gas-solid interface
l	Liquid
lam	Laminar flow
ls	Liquid-solid interface
m	Molten corium
mst	Molten corium-steam interface
r	Relative
s	Solid
st	Steam

tr	Transition flow region
$turb$	Turbulent flow
vi	Visible
vis	Viscous flow regime
w	Water

List of Abbreviations

ANL	Argonne National Laboratory
ANS	American Nuclear Society
BiMAC	Basemat internal Melt Arrest and Coolability Device
BWR	Boiling Water Reactor
CEA	Commissariat à l'Energie Atomique
COCOMO3D	COrium COolability MOdel 3 Dimensional
COMET	COolability of MElT
COMET-H	COMET sustained Heating experiments
COMET-T	COMET Transient experiments
CometPC	COMET Porous Concrete core catcher
ECCS	Emergency Core Cooling System
EPR	European Pressurized water Reactor
ESBWR	Economically Simplified Boiling Water Reactor
IKE	Institut für Kernenergetik und Energiesysteme
JEMI	JEt fragmentation and preMIxing
KIT	Karlsruhe Institute of Technology
LOCA	Loss Of Coolant Accident
LWR	Light Water Reactor
MCCI	Molten Corium - Concrete Interaction
MEWA	MElt-WAter
MESOCO	MElting SOlidification COde
MIT3BAR	MITigation 3rd BARrier
NPP	Nuclear Power Plant

PWR	Pressurized Water Reactor
RPV	Reactor Pressure Vessel
SCRAM	System for Emergency Shutdown of the Reactor Core
SBO	Station Black Out
TMI-2	Three Mile Island-2
VVER	Water-Water Energetic Reactor
WABE	WAter-BEd

1 Introduction

1.1 Motivation and Background

Nuclear Power Plants (NPPs) generate 10% of the world's electricity (as of December 2018) [1]. Among several different types of reactors, Light Water Reactors (LWRs), which use ordinary water as cooling medium (coolant), are the most common type used in commercial NPPs worldwide [2]. While power generation by nuclear energy is highly beneficial due to CO_2 emission-free, continuous and efficient operation, utilizing nuclear fission during this operation is also safety critical due to large amounts of fissile material used as fuel in the nuclear reactor core. The NPPs are therefore designed, constructed and operated in such a way as to prevent potential abnormal and emergency situations and limit their consequences [3]. Reactor configurations in NPPs consist of successive physical barriers in order to prevent radioactive material (fission products) release to the environment. In a generic LWR, these physical barriers are the cladding of the fuel element, where the fission products are generated; the reactor pressure vessel (RPV) and cooling circuit, which is the boundary of the reactor cooling water and contains all the fuel elements forming a reactor core; and the leak-tight containment, which is supposed to keep any fission products inside the containment from escaping to the environment [4]. Systems such as emergency shut down of core (SCRAM) or emergency core cooling system (ECCS) are provided in LWR designs in order to assure the integrity of these barriers. Assuring the integrity of each of these physical barriers in any accident scenario establishes the defense-in-depth approach in nuclear safety against the release of radioactivity to the environment [5].

However, despite all measures taken, the two major accidents in LWR history, Three Mile Island Unit 2 (TMI-2) (USA 1979) and Fukushima Dai-ichi Nuclear Power Station (Japan 2011), showed that the possibility of an accident resulting in partial or complete melting of the nuclear reactor core and subsequent radioactive material release to the environment cannot be excluded. When an accident or operation abnormality happens in a nuclear reactor, the reactor core will be shut down; meaning, the nuclear fission will be interrupted. However, due to ongoing decay of the fission products in the reactor core, it will continue to heat up with the residual decay heat. In LWRs, main cooling

circuit and emergency cooling systems are employed to ensure a continuous and sufficient flow of cooling water into the reactor core in order to remove the generated decay heat until long after the shutdown. Although it is very unlikely, if the events of an accident are beyond the design of safety measures of the reactor and unexpectedly cause the failure of cooling systems or systems, the reactor core will continue to heat up resulting in reactor meltdown. In this highly unlikely event of a core-melt accident, or so-called severe accident, subsequent failure of safety barriers and emergency measures might lead the radioactive molten core interior (core melt or corium) to migrate outside of the RPV inside the containment and eventually to the environment.

In the TMI-2 accident, the sequence of certain events such as equipment malfunctions, design-related problems, and operator errors led to a partial meltdown of the reactor core, resulting in the release of a very small amount of radioactive material into the environment [6] [7]. The accident was terminated by re-flooding of the core, which did not immediately stop further core melting, but did prevent the core from melting through the RPV, and safe stable state was reached without failure of either the RPV or the reactor containment [5] [6].

The most recent LWR severe accident, Fukushima Dai-ichi accident, was a result of an extremely high magnitude earthquake accompanied by a tsunami [8]. These extreme natural events caused a long-duration station black out (SBO) in reactor units of the plant, which hindered the operation of reactor cooling systems. Subsequent failure of main cooling systems, back up and emergency cooling systems (due to the long duration of the power loss, battery supplied systems were also shut down after a while), caused the reactor core to continue to heat up. This led eventually to the melting of the fuel claddings [9]. As molten corium dropped into the bottom of the RPV and then into the bottom of the primary containment vessel, the interaction between heated zirconium cladding of the fuel and steam caused hydrogen built up inside the reactor building. Subsequently, the hydrogen explosions in the reactor buildings resulted in a large release of radioactive material to the environment [8] [10].

After the TMI-2 accident, the focus of the LWR safety research shifted to severe accidents. This accident has shown that not only the large-break loss-of-coolant accident (LOCA), which is the design basis for LWR safety, but also the malfunctions in operations and transients such as small break LOCA can jeopardize the safety of an LWR. In the wake of the TMI-2 accident, some improvements in terms of severe accident management were made in existing plants in order to reduce the probability of a severe accident. The new reactor designs (Generation III / III+) have been employing severe accident mitigation systems in each barrier of the plant in order to strengthen the defense-in-depth. On the other hand, the disaster of Fukushima demonstrated the consequences of extraordinary events. In the aftermath of these both accidents, it was clear that the focus of the severe accident management should not only be reducing the probability of a severe accident to occur, but also to reduce the consequences of a severe accident by providing systems to mitigate the progression of any imaginable severe accident.

The majority of LWR reactors currently in operation are Generation II reactors, such as the reactors of Fukushima. The previous generation reactors that are in operation may not have all the severe accident mitigation systems operating when needed to ensure the prevention of large release of radioactivity.

The reactor containment is the last barrier between radioactivity and environment. If core melt and RPV failure could not be prevented in the course of a severe accident, the corium outside the RPV (so-called ex-vessel) should be stabilized and cooled timely and for longer periods of time. Otherwise, it may lead to containment failure and radioactivity release to the environment due to core melt attacking the concrete containment structure that is known as the Molten Corium - Concrete Interaction (MCCI).

1.1.1 Molten Corium - Concrete Interaction

For a severe accident scenario where the RPV damage happens under low pressure, the core melt relocates from the bottom of the RPV into the reactor containment cavity where it attacks the concrete basemat structure, as roughly illustrated in Figure 1.1. This contact between core melt and concrete leads to the phenomenon called MCCI. This interaction generates steam, H_2, CO and CO_2. H_2 and CO are flammable gases, which poses a threat. In addition, H_2, CO and CO_2 are non-condensable gases which causes the pressurization of the containment. Over-pressurization of the containment might threaten its integrity and cause radioactive aerosols to leak to the environment. Meanwhile, progressive ablation of the concrete basemat structure due to residual decay heat of corium might eventually lead the corium to melt through the containment to the earth underneath.

The composition of the corium that is released from the RPV consists of UO_2, ZrO_2, RPV structural metals (Zr, Fe) and fission products. Its temperature reaches up to 2700 °C leading to the formation of a molten corium pool with temperatures exceeding the decomposition temperature of the concrete [3]. The residual heat released by fission products within the corium cannot be removed by conduction via the basemat due to its thickness and the very low thermal conductivity of concrete. If it remains uncooled, the corium pool could penetrate through the basemat entirely within one or several days, depending on the actual accident scenario and the resulting corium amount in the cavity. The initial decay heat of corium immediately after shutdown is approximately 6% of the reactor thermal operating power [11]. Although it decreases by the time, it remains to be a substantial source of heat for months. Figure 1.2 shows the change in decay heat power in an LWR with respect to thermal operational power of the reactor vs. time after reactor shutdown according to the standard model of the American Nuclear Society (ANS) [11].

Based on these ratios, the generated decay heat for two different types of French PWRs, a 900MWe reactor and a European Pressurized Water Reactor (EPR) with 1650MWe, is presented in Table 1.1. This demonstrate the range of decay heat which needs to be removed during an accident. The amount of corium that relocates into the reactor cavity during a severe accident is highly dependent on the accident scenario. The values calculated for Table 1.1 assume the entire fuel inventory of the reactor to be in reactor cavity as a conservative approach.

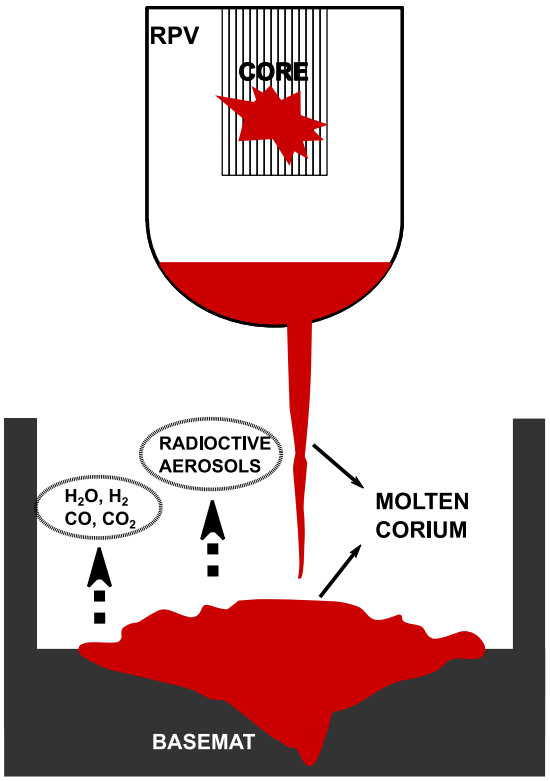

Figure 1.1 Illustration of molten corium relocating from damaged RPV to reactor cavity and MCCI.

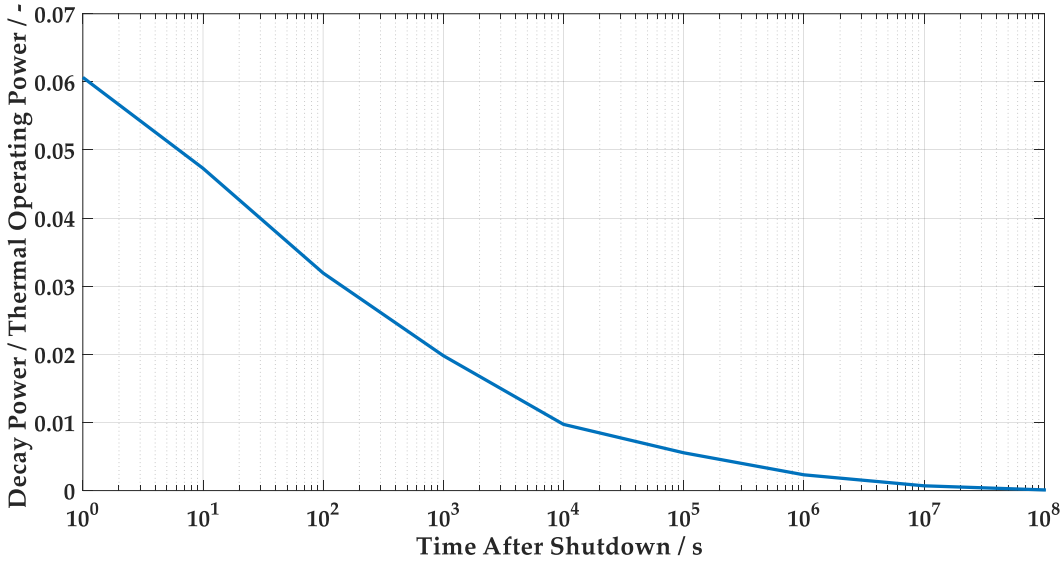

Figure 1.2 Ratio of power produced by decay heat in corium to thermal operational power of an LWR reactor by the time after reactor shutdown.

Table 1.1 Potential decay heat that could be generated in two different type of PWRs after reactor shutdown.

	Thermal operating power of the reactor [MWth]	
	2700 (900MWe Reactor)	4500 (EPR)
Time after shutdown [s]	Corresponding Decay heat power [MW]	
1	164	273
10	128	213
100	86.2	144
1000	53.5	89.1
10000	26.2	43.7
100000	15	25

The highlighted row in Table 1.1 corresponds to approximately 2.8 hours after shutdown, which roughly corresponds to decay heat generated during MCCI if the entire core inventory relocates to the basemat. Without the ECCS, approximately 3 hours after shutdown severe accident progresses into the ex-vessel phase [5]. Depending on the reactor type and accident scenario, this amounts to around 40 MW initial decay heat power that requires to be removed together with the sensible and the latent heat of the corium, and continuous generation of heat in the MW range for months. Therefore, the molten corium released from the RPV should be retained, stabilized and sufficiently cooled for a long period after severe accident.

This thesis investigates an ex-vessel severe accident mitigation system that retains and stabilizes molten corium within the reactor containment building while providing long-term uninterrupted cooling in order to prevent containment failure and radioactivity release to the environment due to MCCI.

In the light of the severe accident management strategies discussed above, it is important that an ex-vessel melt retention system brings flexibility to new designs, such as operating in a passive manner without relying on power supply or human factor, and suited for back fitting to reactors in operation that lack an ex-vessel mitigation system. Ex-vessel molten corium retention is crucial for the integrity of the last barrier of an LWR.

1.2 State of the Art

1.2.1 Ex-vessel Melt Cooling and Retention – an Overview

Terminating the severe accident in the ex-vessel phase requires control over the corium and is conventionally called “the coolability issue”. Resolving the coolability issue does

not only require the removal of the internal (sensible and latent) heat of the corium, but especially extracting the fission product decay heat, which is a long-lasting source of internal heat generation. By extracting both, internal and the nuclear decay heat, from the corium, the basemat attack can be stopped and the containment failure by downward penetration or over-pressurization can be excluded.

Melt is considered "coolable" once a sufficiently low steady state temperature is reached by removing the decay heat [5]. The coolability of a melt pool in the reactor cavity has been a challenging issue and was investigated in severe accident research since 1980. Figure 1.3 demonstrates different ex-vessel corium cooling and retention strategies. During early research in the topic, the coolability of molten corium in the reactor cavity by cooling water overlay (top flooding) was investigated extensively [5] [12] [13], see Figure 3.1.a. It was assumed that pouring the cooling water over the molten corium after it reached the reactor cavity would cool it and be sufficient to prevent the basemat penetration in Generation II LWRs (except Boiling Water Reactors BWRs). However, as a mostly oxide material, corium has a rather low thermal conductivity, which creates a great challenge to remove large amounts of heat by simply overlaying it with a cooling water. Through the investigations, it was found that an insulating crust layer formed on top of the melt layer, which prevented further melt-cooling water contact. Below the formed crust, almost still half of the corium volume stayed molten and kept penetrating through the basemat [5] [12] [13].

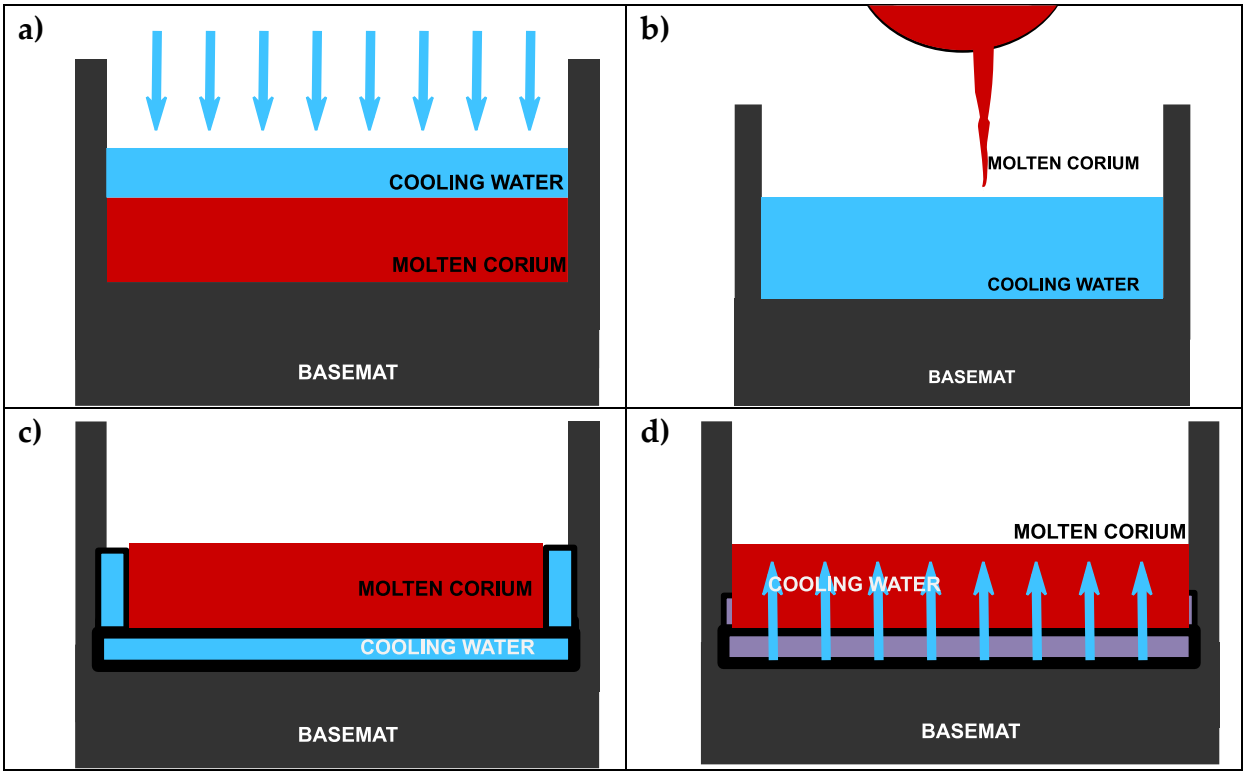

Figure 1.3 Illustration of different ex-vessel corium cooling and retention strategies. a) Top flooding b) Wet-cavity concept c) Envelope type enclosure cooling core catcher d) Bottom flooding

As opposed to providing cooling water after corium arrival to the reactor cavity, the Swedish and Finnish type BWRs operate with a reactor cavity which is already filled with cooling water underneath the RPV as an ex-vessel corium retention strategy [14], see Figure 1.3.b. In case of an RPV damage, corium would pour into an already existing cooling water pool, which is expected to cause fragmentation of corium that increases its contact with water, hence a more efficient cooling. The advantage of such a retention strategy is that it is simple and does not require any additional construction while the cooling water would be readily available for corium. The disadvantage is that while melt breaks into melt particles, the sudden increase in the surface area of contact between melt and cooling water can lead to a steam explosion in the reactor containment. Moreover, the particles that are formed can accumulate as one heap of debris on the bottom, which again decreases the surface area of contact, therefore diminishing the cooling advantage of the strategy [5].

New reactor designs, Generation III / III+, are implementing enhanced mitigation systems and strategies for stabilization and cooling of the molten corium released from the RPV. One strategy is based on the enclosure of the melt combined with external cooling, see Figure 3.1.c. In the enclosure concept, the molten corium is caught and collected in a vessel-like structure in the reactor cavity (a core catcher), which is externally cooled or retained from all borders, sometimes combined with top flooding. The EPR concept core catcher [15] [16] allows the melt to spread on a large area to bring some surface increase. Upon release from the RPV the melt is mixed with a sacrificial concrete layer to reduce the viscosity and the temperature. The melt could then spread on the wide core catcher which is cooled via boundaries and the melt itself is flooded from top. However, the melt layer still stays relatively thick and uncooled molten parts in corium can exist over weeks or months until the decay heat is removed.

Another enclosure concept is the TianWan core catcher [5] [17], which was designed for Russian Water-Water Energetic Reactor (VVER). The TianWan core catcher is a steel vessel that collects the corium which is released from the RPV directly under the RPV in a more traditional sense of a core catcher and provides cooling externally. The corium is mixed with sacrificial material (Fe_2O_3) in the core catcher, which reduces the power density while increasing the surface for heat removal. However, similar to the EPR concept, the corium stays in molten state for even longer times.

The Basemat internal Melt Arrest and Coolability Device (BiMAC), was developed for European Simplified Boiling Water Reactor (ESBWR) [18], and is another core catcher in the traditional sense that aims to collect corium underneath RPV while providing the external heat removal via a pipe system surrounding the core catcher. This concept and design are still under evaluation, however, similar to the concepts above, the corium would stay mostly in the molten state for long period without a proper cooling water ingression.

The enclosure (or core catcher) systems provide an initial retention of molten corium that is released from the RPV into the containment. However, having the corium mostly in

liquid form while producing substantial decay heat for weeks and months might create a risk of failure during this long period after severe accident. Moreover, having a more elaborated design and requiring more space, such devices are not suitable for back fitting to existing reactors that do not have an ex-vessel retention system.

As an alternative to these retention strategies, Karlsruhe Institute of Technology (KIT) has developed a core catcher concept that retains corium and passively injects water to corium from below (COMET concept) [19] [20], see Figure 1.3.d. The experimental investigations of the concept have shown that bottom flooding stabilizes and cools the corium effectively [20] [21] [22] [23] [24] [25] [26] [27].

During bottom-flooding, as the water and steam raises upward, the corium moves downwards due to its high density which provides a constant mixing of the corium and the coolant. This mixing and penetration of the coolant into the corium during bottom-flooding leads to higher fragmentation of the molten corium than in the case of top flooding. This higher fragmentation during bottom-flooding increases the heat exchange surface of the corium and provides cooling water to the entire molten corium bulk and even into the deeper layers. This leads to rapid cooling and solidification of the corium into a porous structure. Corium that solidifies as a porous structure can then be cooled for a long-term as the cooling water can continue to flow through the solidified corium.

1.2.2 Bottom-Cooling and CometPC Core Catcher

Bottom-Cooling Concept

In the original design of the COMET bottom-cooling concept, the cooling water percolates the melt from below through pre-installed plastic nozzles that are embedded in a concrete layer. These nozzles are connected to a water reservoir that is pressurized by static water head [21] [22]. A sacrificial concrete layer is initially on top of these nozzles. This both prevents water to flow pre-maturely and improves the coolability of the corium when mixed with it by decreasing the viscosity and the power density of the corium. Upon arrival of the melt, the sacrificial layer on the nozzles erodes and the cooling water begins to flow in a passive manner driven by the hydrostatic pressure head of the water.

Bottom-Cooling Experiments

To represent the molten corium properties, thermite simulants were used to generate high temperature melts of iron and aluminum oxide. The series of experiments that were performed by KIT have shown the COMET concept to be efficient for corium arrest and cooling, therefore promising for reactor application [20] [26]. The transient experiments where the thermite material only has an initial heat and not supplied with constant heat

(COMET-T) were performed in a circular test set-up with approximately 0.35 m diameter. These experiments were important for demonstrating the effects of flooding water pressure on cooling and fragmentation of the melt layer. It was demonstrated that the cooling water should be provided with an effective overpressure, which is the difference between hydrostatic head of the cooling water reservoir over the core catcher surface and the hydrostatic pressure of melt layer. The experiments with 0.2 bar (20 kPa) effective overpressure resulted in more efficient cooling and fragmentation of the melt layer with rapid cooling and solidification.

With the same original design, COMET research continued with experiments using the same thermite material with sustained induction heating. This provided a constant heat source that replicates the decay heat during severe accident. These experiments, called COMET-H, were performed in a circular test set-up with approximately 1-meter diameter. During these experiments, molten oxide and metal layers up to 0.5-meter-high have been safely arrested and cooled through bottom flooding [20] [26]. The effective overpressure of cooling water of 0.2 bar (20 kPa) provided between 1-2 kg/(m^2s) (approximately $1x10^{-3}$ - $2x10^{-3}$ m/s for completely open flow path) flooding rate that resulted in high cooling rates up to 3 MW/m^2. This cooling rate is sufficiently higher than the generated decay power rate in a reactor cavity with approximately 6 m diameter, which yields to be around 1.4 MW/m^2 for an assumed maximum decay power heat of 40 MW. For higher flooding rates of water, shorter solidification time is observed. Moreover, the melt solidifies into a porous structure with an average porosity of 50% [20], which consists of large openings filled with evaporating cooling water that provide large surfaces for heat transfer from melt and a safe long-term cooling.

Bottom cooling was also investigated in the DECOBI program [28] with a core catcher design similar to COMET core catcher with nozzles. These experiments were performed in relatively small test set-up with 20 cm diameter. Medium temperature and high temperature experiments were performed with simulants of pure molten lead and with oxide mixtures respectively and water as a coolant. The experiments with various coolant flow rates and melt layer heights resulted in successful cooling and fragmentation of the melt [28]. Coolability by bottom flooding of more realistic corium material with UO_2 and ZrO_2 was also investigated at Argonne National Laboratory (ANL), in USA [29] [30] [31] and at Le Commissariat à l'énergie atomique et aux énergies alternatives (CEA) [25] facilities in France. These experiments with real corium material showed promising results in terms of safe cooling and fragmentation of the high temperature corium with decay heat production.

CometPC Core Catcher and CometPC Experiments

The promising results delivered by bottom cooling in COMET research has motivated for advancing the concept for reactor applicability, especially for back-fitting constrictions. A design alternative to the original COMET concept, CometPC, has been de-

veloped by KIT with the idea of having the advantages of bottom-flooding and also having a core catcher design that is technically relatively simple to install and therefore could be more suitable for back-fitting to existing reactors [32] [33]. As shown by Figure 1.4, instead of embedded nozzles, CometPC design relies on porous concrete layers to provide the cooling water from below into the molten corium.

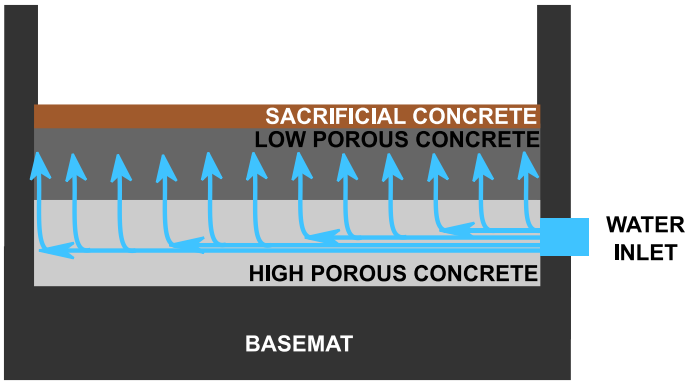

Figure 1.4 Illustration of CometPC core catcher on basemat of reactor cavity.

As can be seen on Figure 1.4, the CometPC core catcher device consists of two concrete layers with different porosities with a sacrificial layer on top and placed right on the basemat of reactor cavity underneath the RPV. The lower concrete layer of the core catcher is a high porous concrete with high water permeability. The cooling water supply is provided on the side of this layer. Due to the high porosity and high water permeability, the water is distributed along the large reactor cavity horizontally through the high porous concrete layer. The vertical flow of the cooling water upwards toward the melt is limited by the low porous upper concrete layer.

The upper concrete layer of the device has a lower water permeability than the lower concrete layer, which aims to control the upwards flow of cooling water to a desired flow rate.

Initially there is a leak tight sacrificial concrete layer on top of the low porous concrete layer, which both serves to prevent a pre-mature coolant flow to the cavity and to improve the coolability of the corium as in the original COMET design. Prior to the possible accident and corium discharge the sacrificial layer is intact and the pores of the CometPC are filled with cooling water, which is provided from a storage with a hydraulic head. Upon arrival of the molten corium and ablation of the sacrificial layer, the cooling water percolates into the melt passively due to the pressure difference of the hydraulic head.

Although not as extensively as the original COMET concept, the coolability of corium by bottom flooding through CometPC core catcher has been investigated by KIT. Similar to the original COMET program, a few transient experiments (CometPC-T) were performed in a circular test set-up with approximately 0.35 m diameter [32]. After success of these transient experiments a few experiments were performed in a circular test set-up with approximately 1 m diameter, with sustained heat simulating the decay heat. A

simulant similar to previous COMET experiments (CometPC-H), a mix of metal and oxide melts, was used in CometPC experiments as well. During these sustained heat experiments, melt layers between 30 cm – 50 cm were cooled and solidified successfully [23] [24] [27]. An overview and some important data for a few of these CometPC experiments can be seen in Table 1.2. These data are a good representation of the parameter range of COMET and CometPC research as well. The effective overpressure (the difference between hydrostatic head of the cooling water reservoir over the core catcher surface and the static pressure of melt layer) of the cooling water was between 0.1 and 0.2 bar for different experiments, which provided a flow rate between 1-2 l/s. Cooled and solidified melt layers had approximately 50% porosity, similar to that of COMET experiments, according to post-test analysis [23] [24] [27].

Table 1.2 Important data from a few of the CometPC experiments.

	CometPC H4	CometPC H5	CometPC Plus
Height of Sacrificial Layer [m]	0.10	0.08	0.05
Height of Low Porous/Upper Layer [m]	0.06	0.06	0.23
Height of High Porous/Lower Layer [m]	0.06	0.06	0.08
Diameter of CometPC Surface [m]	0.92	0.92	0.92
Melt Type	Al_2O_3+CaO+ Fe+Ni	Al_2O_3+CaO+ Fe+Ni	Al_2O_3+CaO+ Fe+Zr
Simulated Decay Power [kW]	350	350	~400
Initial Melt Temperature [K]	2073	2163	2173
Effective Overpressure [bar]	0.1	0.1	0.2
Total Water Inflow Rate [l/s]	1.2	1.0	1.4
Height of Initial Melt Layer [m]	0.35	0.5	0.50
Total Porosity of Solidified Melt [%]	~50	~50	47

The sustained heat experiments with the CometPC device were performed in a set-up that has a relatively large geometry for an experimental investigation. However, compared to a generic containment cavity with approximately 6 m diameter, a test-up that has only 1 m diameter could be considered small. As a passive system, the CometPC device inherently relies on the water permeability of a porous concrete, hence the geometry and the structure of the porous concrete itself have a significant effect on the melt coolability. The performance of a porous concrete for radial distribution of the cooling water over the large cavity in a reactor is still not clear from these experiments. For effective cooling, a corium retention system should ideally provide the cooling water to the corium at every point of the reactor cavity. Therefore, it is essential to comprehend the performance and working principle of a porous concrete system in a large geometry. Especially, for back-fitting cases where the cooling water might be provided to the CometPC device in a more restricted way, e.g. limited or narrow connection to the water reservoir, it is important to investigate the limitations of a porous concrete core catcher system. Overall, the impacts of a porous concrete core catcher device on corium coolability by bottom flooding should be assessed for reactor applications.

1.2.3 Corium Fragmentation by Bottom-Flooding

The crucial process for successful cooling by bottom flooding is a sufficient breakup of the compact molten corium layer and the formation of a coolable porous structure. Previous studies have concluded that the dominant part of cooling mechanism of molten corium by bottom flooding is fragmentation of the melt and formation of the porosities. However, the exact process of fragmentation is yet to be fully understood.

After bottom cooling experiments, the solidified melt blocks that the experiment were performed on were cut across the middle vertically in order to observe the morphology of the formed porosity. Figure 1.5 shows the pictures from various bottom cooling experiment post-test cross-sections for better understanding of the mentioned porous structure. Figure 1.5 a) is the cross-section of solidified oxide and metal melt mix from the COMET-H 1.3 experiment. Figure 1.5 b) is the cross-section of the solidified oxide and metal melt mix from COMET-H 2.2 experiment. Figure 1.5 c) is the cross-section of the solidified oxide and metal melt mix from CometPC-H5 experiment which also shows the cross-section of CometPC core catcher below the solidified layer. Figure 1.5 d) is the solidified oxide melt form DECOBI-HT CB7 experiment.

Figure 1.6 shows pictures from most recent CometPC experiment (CometPC Plus) performed by KIT as a part of the MIT3BAR (Mitigation 3rd Barrier) project. Figure 1.6 a) is a picture taken when the water inflow was initiated, it also shows the ejection of the melt. Figure 1.6 b) is the cross-section of the solidified oxide-melt layer, and cross-section of CometPC core catcher below.

As can be seen in post-test pictures, the melt layer solidified into a porous structure. In addition, for the case of these experiments, the solidification occurred with rather well

distributed openings through the solidified melt. A molten corium layer that solidifies with porous structure comparable to these experiments would bring a successful corium arrest and long-term cooling, as it did during these experiments. The majority of post-test analyses of the solidified and cooled melt layers show that the void in the solidified structure is a combination of vertical channels and more round pores throughout the block. Nonetheless, the morphology of these openings is relatively random.

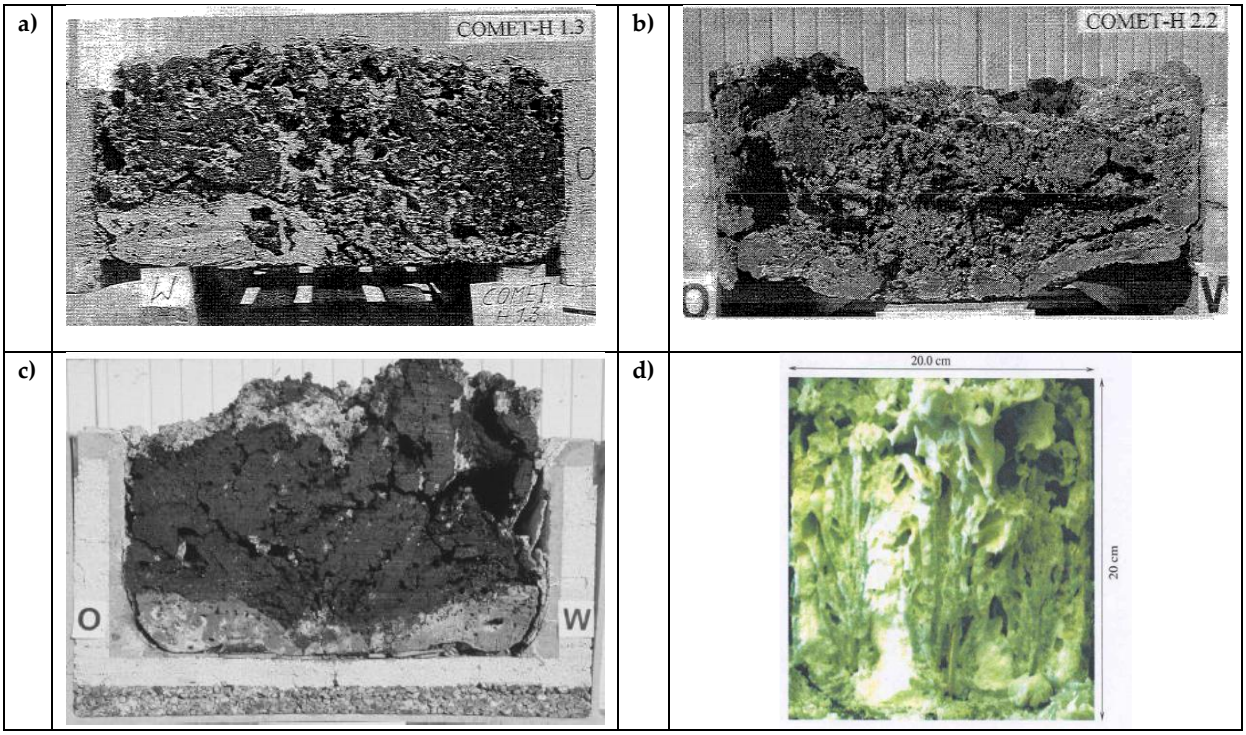

Figure 1.5 Post-test cross-sections of solidified melts from various bottom cooling experiments. a) COMET-H 1.3 [20] b) COMET-H 2.2 [20] c) CometPC-H5 [24] d) DECOBI-HT CB7 [28].

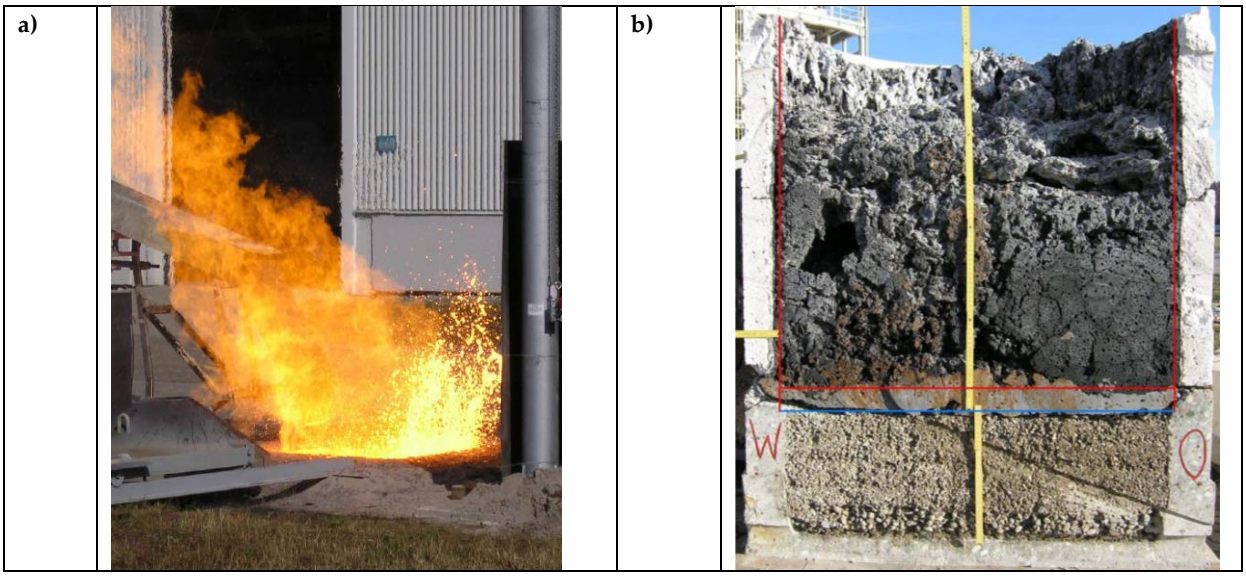

Figure 1.6 Pictures from CometPC Plus experiment [27]. a) Melt ejection during initial water flow into the melt, b) Post-test cross-section of solidified melt.

There were a few experiments that ended up having one or two large main voids in the solidified form as a result of so-called volcanos formed during cooling. It was concluded that these volcanos happen as a result of thin crust formation on top of the melt layer and anchoring to the test set-up walls, which then causes the accumulated cooling water to exit with an eruption. The crust anchoring was considered to be the artifact of a small experiment set-up. Therefore, this phenomenon and the resulting formation of a single volcano could be excluded for reactor case considerations. Cooling water mixing into the very hot melt is a violent process that also results in dispersion and ejection of small melt particles. The effect of dispersion might be different for reactor case conditions and for smaller scale experiments as well. During the experiments performed in small test set-ups, the dispersed particles tended to stick and solidify on the walls of the test set-up or being ejected from the test-set up, which might be misleading for evaluating the final porosity of the solidified melt. The dispersion might happen in reactor case, too. However, for the large cavity, they would return and mix into the molten pool. For analyzing the fragmentation and cooling of the melt layer in case of a real accident in a reactor, the focus should be the evaluation of the formation of channels and pores.

The COMET research has shown that a higher evaporation rate of the coolant and a lower viscosity of the melt enhance the fragmentation of the compact melt layer. High pressure for water ingression and high melt temperature lead to fast evaporation of cooling water and likely to an increased fragmentation rate. However, a high fragmentation rate and the causing factors might not necessarily result in high porosity for the solidified melt. If the steam that evaporates from cooling water has a high velocity, it might just escape the compact melt layer without much interaction to cause porosities by leaving only channels behind. Based on the observations during the COMET experiments with both metal and oxide melt layer, it was concluded that fragmentation is more intense in the metal layer which has a low viscosity compared to the oxide layer. However, post-test cross-sections showed a higher porosity build up in the oxide layer than the metal layer.

This could be interpreted as an effect of viscosity; although a lower viscosity for melt is beneficial for fragmentation the open voids could be also filled back rapidly because of the low viscosity. Another interpretation of higher porosity build-up in the oxide layer could be the solidification range, due to the larger solidification range of oxide melt cooing water and steam has more time to interact with melt to create voids. Although both of these effects seem to be related to melt property, the manner that cooling water and steam move through the melt could also be seen as the common parameter that determines the porosity build up. As a low viscous melt layer allows cooling water and steam to escape faster, there would be no long interactions and the steam will leave quickly through channels without porosity build up. Whereas cooling water and steam will leave the high viscous melt slower, spend more time passing through the melt and interacting longer causing more porosity build up while solidifying. In a similar way, a higher solidification range as in the case of oxide melts, causes slower evaporation of water, gives more chance for interaction between cooling water and melt layer to interact, thus causing higher porosity build up.

The strong interactions between melt layer and cooling water observed in DECOBI program for low water flow rates, can also be an indication that the velocity of cooling water is an essential parameter and decisive for porosity build up in a melt layer. Furthermore, in the post-test cross-sections of COMET and CometPC experiments, channels were observed in the metal layer while there were more pores in the oxide layer. This also supports the argument that rapid evaporation, high steam and coolant velocities causes the coolant to escape through channels without much interaction with the melt whereas low velocities of steam and coolant results in porosity build up in the melt layer.

It is crucial to model the above described phenomena physically, not only phenomenologically, in order to predict the cooling process of the corium layer in reactor cavity by bottom flooding successfully. Although the experiments resulted in complete solidification and cooling of the melt layers, the dimensions of the performed experiments are relatively small compared to the size of a reactor cavity. The large dimension of the reactor cavity and the accumulated melt pool require evenly distributed fragmentation of the compact melt layer and evenly distributed voids and open channels in the solidified melt in order to provide continuous heat removal from corium. Therefore, it is essential to predict the fragmentation of the molten corium and the morphology of the solidified corium in the reactor cavity by more realistic representative modelling for simulations.

Modelling of Porosity Formation

As the post-test solidified melt structures do not define a clear systematic morphology and the void patterns are relatively random, the exact modelling of the formation of these openings for the reactor case is not possible. Even an approximate modelling of porosity formation for the reactor case is highly challenging and still under discussion in the community. The prior efforts for modelling these phenomena in the bottom cooling research have their shortcomings and improvements are still necessary.

A standalone model for porosity build up was developed by Widmann [34] [35] [36] at the Institute of Nuclear Technology and Energy systems (IKE) for simulating the corium cooling by bottom flooding with the MEWA-COMET code, which is developed at the Institute as well. The model calculates the porosity build-up rate in a fixed porous corium block based on the local pressure difference of the coolant flowing through the pores and the material properties of liquid corium [34] [35]. The biggest drawback of the model is that it assumes corium as a fixed liquid matrix with initial porosity, and the change in porosity is introduced artificially based on local pressure difference in this liquid. With this assumption, the porosities and openings can exist in parts of the molten corium where in reality there would have been no fragmentation. As the corium is not modelled as a moving liquid, the physical representation of these pores and their places might be misleading. Moreover, the influence of the corium viscosity in the model is such that low viscosity leads to higher porosity build up in the corium. As it was discussed earlier, phenomenologically, a low viscosity leads to low porosity and singular channels in the

solidified corium. Overall, this modelling can be seen insufficient for both, the physical and phenomenological representation of the porosity formation in the corium layer.

Another porosity model for corium was developed by Paladino, as a part of the DECOBI program. This model focuses on channels formed in the solidified corium and assumes channel-like openings in the solidified corium with the diameter of nozzles that the coolant flows through, and the regions between these channels are assumed as solid blocks without pores [28]. Although this model can be seen as a conservative approach, it does not model the corium as a moving liquid. Moreover, a porosity value based on nozzle diameter of the experiment is not a universal representation of bottom cooling phenomena. For a real accident simulation, the behavior of molten corium during bottom flooding cannot be represented with this model, which does not model the corium as moving liquid.

A porosity formation model for bottom flooding of corium that models molten corium as a moving liquid still does not exist. Such a model where molten corium is represented as a fluid could predict the bottom cooling more accurately for the reactor simulations, where very large corium pools could exist. Based on the experimental investigations, although without a common morphology, the solidified melt has void regions that are a mix of channels and pores. Closer representation of the morphology that occurred during the bottom cooling experiments together with better representation of corium physical properties would lead to more accurate simulations for corium fragmentation and porosity build up in the in the reactor cavity. This would then facilitate a better understanding of the coolability.

1.3 Aim of the Present Work

The overarching goal of this work is to obtain a better understanding of coolability of molten corium in the reactor cavity by bottom cooling through a porous concrete core catcher. In order to achieve this understanding, this work investigates multiple aspects of the concept with emphasis on the following points and objectives:

- This work aims to determine the major design parameters and required properties for a bottom cooling concept using a structure of two porous concrete layers considering the dimensions of a generic pressurized water reactor (PWR) of Gen II. Although the experimental investigations of such a concept show a success for bottom cooling, the requirements and challenges for adequate cooling in a large reactor geometry require a comprehensive evaluation. In addition, the determination of the relation between design aim and porous concrete properties is required for a better evaluation of the applicability of this concept to reactors. With respect to these needs, the present work aims to develop a methodology for optimization of the hydraulic parameters of a porous concrete core catcher device for reactor application.

- Furthermore, this work aims to obtain a better understanding of the cooling process in the CometPC experiments by measuring the permeability of concrete samples from these experiments. Using these measurement results to simulate the CometPC experiments can enlighten the effect of other unknown parameters from the experiments. Moreover, reactor scale simulation with the measurement results of concretes can help to evaluate the applicability of CometPC device from experiments directly to a reactor.

- Finally, this work aims to develop an improved model that represents porosity build up in the melt layer due to bottom flooding that provides a better representation of the physics of the melt layer and the phenomenology of the fragmentation and porosity build up observed in the experiments. In order to achieve this, it is aimed to model molten corium as a moving liquid with its density and viscosity. This model development allows a more realistic approach for the simulation and the prediction of the cooling of the corium layers by bottom flooding in case of a severe accident in an LWR.

Outline of the Work

Chapter 2 introduces the simulation code and the theory that is used in this work. The theory from the literature that is included in this chapter serves as the basis of the analysis performed in this work. The methods and models developed by this work are implemented in the in-house system code COCOMO3D for simulation of various scenarios and parameters. Therefore, this chapter also gives a short introduction to the code.

Chapter 3 analyzes the hydraulics of a porous concrete core catcher system. The chapter begins with the technical definition of the porous concrete core catcher for reactor application, then evaluates the cooling water distribution within the core catcher for various configurations and boundary conditions, presents the simulation results and discusses the limitations. Furthermore, this chapter presents a methodology for optimizing the porous concrete core catcher layers in order to achieve sufficient cooling water rates delivered to the melt layer along the entire core catcher surface.

Chapter 4 shows an experimental and numerical investigation on permeability of porous concrete samples used in the CometPC experiments. The first part of the chapter shows the experiment set-up, measurement methodology and results. The second part of the chapter discusses the applicability of this porous concrete core catcher device in a reactor geometry by simulating the cooling water distribution with the measured permeability. The third part of the chapter applies the measurement results to simulations of CometPC experiments and evaluates the outcomes.

Chapter 5 shows the development of a fragmentation model for molten corium by void fraction modeling of molten corium-steam two-phase flow. The chapter starts with introducing the simplified one-dimensional two-phase flow momentum exchange model. A standalone simulation code was written in order to solve this simplified one-dimen-

sional two-phase flow model for various interfacial friction closure models from literature based on drag-force and drift flux approaches for molten corium and steam properties. The resulting void values are compared with COMET and CometPC experiment range. The new interfacial friction closure model is developed for the improved molten corium-steam two-phase flow momentum exchange modelling. The void fraction outcome as a result of the new friction model is validated against experiment data range from COMET and CometPC with a standalone simulation code. The two-phase flow simulations with the new friction model and the results for CometPC and reactor case are presented. Finally, the assumptions and limitations of the improved momentum transfer model are discussed.

Chapter 6 gives a short conclusive summary of the work and the obtained results, and an outlook on foreseen improvements.

2 Theory and Simulation Code for the Investigations

This chapter introduces the theory and the simulation code that was used during the investigations in this work. The investigation of coolant flow through the porous concrete core catcher device and the optimization for large geometries requires understanding of the friction laws for fluid flow through porous media. The dynamics of a single-phase flow through porous media that is used as a base for this work will be briefly introduced and discussed in this chapter. For the model development of fragmentation in molten corium layer, two-phase flow momentum exchange modelling from literature is used as a foundation for this work. Two main approaches for interface friction closure for momentum exchange modelling of two-phase flow will be briefly introduced in this chapter as well.

The system simulation code COCOMO3D that is being developed in IKE, was used as a simulation tool for the investigations in this work. The models and methods that were developed by this work were implemented in COCOMO3D with the aim of improving the simulation capability of a severe accident scenario in a nuclear reactor. Basic simulation principles of the code and models that already exist in it that were used in this work will be introduced and discussed for a better understanding of the simulation results that are shown in this work.

2.1 Water Flow through Porous Media

As a fluid flows through the openings of a porous medium, the rough, tortuous structure of the porous medium will cause a loss of energy due to friction. This energy loss with respect to fluid velocity can be mathematically described by Darcy's Law [37] [38], which originates from ground water research, as follows:

$$\dot{V} = \mathrm{K}_k A \left(\frac{\Delta z}{h}\right) \tag{2.1}$$

Equation (2.1) applies to the unidirectional steady and sufficiently slow flow of a fluid through a porous medium, with cross-sectional area of A and a length (or height) of h. The volumetric flow rate, $\dot{V}$ (in the literature can be also indicated as Q), is linearly correlated to the energy loss per unit weight, Δz, which is the sum of pressure head and elevation head that is commonly described as hydraulic head for the case of water flow. K_k is the fluid conductivity (or in case of water flow; hydraulic conductivity) which describes the ability of a porous medium to conduct liquid through it. Fluid conductivity of a porous medium depends both on the pore structure of the porous medium and physical properties of the fluid [39].

Permeability is a measure of the ease with which fluids pass through a porous material. Permeability, or intrinsic permeability, depends solely on properties of the porous medium such as pore or grain size and distribution, shape of grains or pores, tortuosity and porosity. It is independent of the density and viscosity of the fluid and is described as follows with respect to fluid conductivity [39]:

$$k = K_k \frac{\mu}{\rho g} \tag{2.2}$$

Where k is the permeability of the porous medium, μ is the dynamic viscosity of the fluid, ρ is the density of the fluid and g is the gravitational acceleration. With permeability, the Equation (2.1) can be rewritten as follows:

$$\dot{V} = A \frac{k}{\mu} \frac{\Delta p}{h} \tag{2.3}$$

Where Δp is the total pressure loss of the fluid. The term $\frac{\Delta p}{h}$ indicates the total pressure loss the fluid experiences per unit length of the porous medium which in this case can be described as the pressure gradient or in case of water; hydraulic gradient. The volume flow rate per unit area of the porous medium is the volumetric flux, or superficial velocity of the fluid, which is described as follows:

$$\frac{\dot{V}}{A} = j_f \tag{2.4}$$

The Equation (2.3) can be rewritten for relation between superficial velocity and pressure gradient as follows:

$$\frac{\Delta p}{h} = \frac{\mu}{k} j_f \tag{2.5}$$

Where j_f is the superficial velocity of the fluid.

For flow through packed beds, if the aggregate size and porosity is known, Darcy's Law also suggests the equation to determine the permeability as follows [37]:

$$k = \frac{\varepsilon^3 {D_p}^2}{180(1-\varepsilon)^2} \tag{2.6}$$

Where ε is the porosity and D_p is the characteristic diameter of the aggregates.

As mentioned above, Darcy's Law has its roots in the ground water research, where the flow of water is very slow. While it approximates viscous creeping flow quite successfully, for higher flow rates of the fluid the linear dependency of the pressure gradient on the fluid velocity is no longer valid [37]. For higher velocities of the fluid, especially when the distortion in the streamline occurs, the inertial forces become significant compared with viscous forces. In this case, an inertial term that accounts for the nonlinear behavior of the hydraulic gradient against fluid flow should be added to the Equation (2.5) as follows [39]:

$$\frac{\Delta p}{h} = \frac{\mu}{k} j_f + \frac{\rho}{\eta} {j_f}^2 \tag{2.7}$$

The second term on the right-hand side of Equation (2.7) is known as the Forchheimer term [39] [40]. The Forchheimer term represents the inertial forces during fluid flow through a porous medium, where the parameter η represents the inertial permeability, better known as passability. For this non-linear dependency, Ergun's Law [41] can be applied to flow through packed beds for known aggregate size and porosity in order to determine permeability and passability as follows:

$$k = \frac{\varepsilon^3 {D_p}^2}{150(1-\varepsilon)^2} \tag{2.8}$$

$$\eta = \frac{\varepsilon^3 D_p}{1.75(1-\varepsilon)} \tag{2.9}$$

A porous concrete core catcher as in this work inherently relies on the passive pressure hydraulic head of the cooling water reservoir connected to it, to provide the cooling water into the molten corium. As it is presented in this section, the permeability of the porous concrete (or in the case of higher flow rates: permeability and passability of the porous concrete) is the decisive factor for the resulting water flow rate under a certain

pressure applied. Therefore, the structure of the porous concrete is an important component while evaluating the system parameters for a porous concrete core catcher. A porous concrete is a consolidated porous medium which means the cementation has as much effect on the permeability and passability as the aggregate size. While the empirical models in Equations (2.6), (2.8) and (2.9) might approximate the permeability and passability for packed beds, in case of porous concrete it is best to determine them for each individual medium via measurements.

2.2 Interfacial Momentum Exchange and Friction in Two-phase Flow

The major relations that describes the physics of interactions at the interfaces of a two-phase flow are: interfacial momentum transfer, interfacial heat transfer, wall friction and wall heat transfer. The two-phase flow that is considered in this work is the interaction between coolant and molten corium pool in ex-vessel. Due to geometry, the wall friction and wall heat transfer that applies to pipe flows are neglected during the analysis in this work. Moreover, the analysis was carried out with the assumption of coolant and corium being in thermal equilibrium, considering only the momentum interaction in the fluid-fluid two-phase interface. Therefore, the focus of this section is momentum interactions at the interface for determining the void fraction.

The void fraction is one of the most fundamental geometrical parameters in two-phase flow analysis. The void fraction, α, which is the ratio of gas volume to the total volume of gas and liquid in the system can be calculated as follows:

$$\alpha = \frac{V_g}{V_l + V_g} \tag{2.10}$$

Where V_g is the volume of gas phase in two-phase flow and V_l is the volume of liquid phase.

Void fraction is an essential part of modelling the relative motion and the friction between different phases as well as the transfer at the interfaces of a two-phase flow. In this work, modelling and determining the void fraction and its structure for corium-coolant interaction means modelling how molten corium fragmentation occurs and how the coolant penetrates into the molten corium during bottom cooling. This knowledge can then provide the basis for understanding how molten corium and later solidified corium is cooled via coolant in this void.

Depending on the two-phase flow modelling approach, different constitutive equations for momentum and the closure equations for the momentum transfer exist in the literature for defining the interaction and friction between the phases. It is essential to apply the suitable approach for momentum balance, relative motion and friction between the

phases, in order to determine the void fraction of the system accurately. In this current work, two approaches were considered to model friction between the fluids: drag coefficient approach and drift velocity approach.

Drag coefficient approach is part of the two-fluid modelling of two-phase flow [42] [43] [44] [45]. The two-fluid model describes the phases separately with their own conservative equations governing the balance for mass, momentum and energy of each phase. The interfacial momentum transfer between the phases is modelled by the constitutive relation that is called generalized drag force. Generalized drag force, which specifies the interfacial surface forces between two phases when one is dispersed in the other, consists of standard drag force and transient forces. The part of the constitutive equation responsible for the steady state drag, the standard drag force, is predominantly responsible for describing the degree of momentum equilibrium between the phases [44] [46]. Transient forces, such as the virtual mass force, are added to improve numerical stability. This work focuses on the steady state closure of the interfacial drag in two-phase flow. The generalized drag force for standard drag force in multi particle dispersed flow is modelled according to Ishii and Hibiki [44] [45] as follows:

$$F_d^D = -\frac{1}{2}\frac{s_d}{V_d} A_d C_D \rho_c v_r |v_r| \tag{2.11}$$

Where F_d^D *is* the drag force on the dispersed phase per unit volume of the two-phase flow, s_d is the volume fraction of the dispersed phase, ρ_c is the density of the continuous phase, C_D is the drag coefficient, v_r is the relative velocity, A_d is the cross-section area of a typical particle in dispersed phase and V_d is the volume of a typical particle in dispersed phase (in the literature can be also indicated as B_d). With the assumption of a spherical shape for a typical particle, with a characteristic representative radius r_d, A_d and V_d can be described as follows respectively:

$$A_d = \pi {r_d}^2 \tag{2.12}$$

$$V_d = \frac{4}{3}\pi {r_d}^3 \tag{2.13}$$

Equation (2.11) can be re-written as follows:

$$F_d^D = -\frac{3}{8}\frac{s_d}{r_d} C_D \rho_c v_r |v_r| \tag{2.14}$$

Where, r_d is the characteristic radius of a typical particle in a dispersed phase. Depending on the modelling method, r_d can be assumed to have a constant value during flow

or assumed to be changing with the relative velocity of the flow based on the Taylor instability of droplets and bubbles. The relative velocity, v_r, is defined as follows:

$$v_r = v_g - v_l \tag{2.15}$$

Where v_g is the velocity of the gas phase and v_l is the velocity of the liquid phase.

The drag coefficient, C_D, in the Equations (2.11) and (2.14) is a dimensionless number that describes the drag correlation for the dispersed flow depending on the particle shape, flow regime and pattern. The drag coefficient correlations will be discussed further in Chapter 5 during modeling of molten corium and coolant two-phase flow.

The two-fluid model provides the most detailed and accurate macroscopic formulation of two-phase systems and is often used for LWR accident system analysis simulation codes [46] [47] [48], albeit for the two-phase modelling of coolant not the coolant and liquid corium. In terms of applicability range for different materials and flow conditions, the drag force approach brings certain flexibility, which poses an advantage for the model development in this work. However, the accurate modelling remains challenging for this approach as it depends on the flow regime mapping and transition criteria.

The other approach that is considered in this work for modelling of interfacial transfer closure for corium and coolant two-phase flow is the drift velocity approach. The drift velocity approach is part of the drift flux modelling of two-phase flow where the liquid and gas phases are regarded as a mixture [45] [49] [50] [51]. There is one set of balance equations for mass, momentum and energy that governs the mixture. While modelling the mixture momentum the interfacial interaction between liquid and gas is described with drift velocity. For pool flow, where the gas flows into an existing liquid pool, the drift velocity is modelled according to Kataoka and Ishii [51] as follows:

$$(1 - \alpha)v_r = (C_0 - 1)j + V_{gj} \tag{2.16}$$

Where α is the void fraction, v_r is the relative velocity, j is the total volumetric flux (total superficial velocity), C_0 is a dimensionless number that is called distribution parameter and V_{gj} is the average local drift velocity. The total volumetric fluxes of the phases are calculated as follows:

$$j = j_g + j_l \tag{2.17}$$

Where j_g is the volumetric flux of the gas phase and j_l is the volumetric flux of the liquid phase. j_g and j_l can be described in terms of velocities of each phase and the void as follows:

$$j_g = v_g\,\alpha \tag{2.18}$$

$$j_l = v_l(\,1-\alpha) \tag{2.19}$$

The constitutive relations for both C_0 and V_{gj} are modelled in literature based on flow pattern and properties, and fluid properties, which will be discussed further in Chapter 5.

Although drift velocity and drift flux modelling bring a relatively simpler approach on void fraction modelling in two-phase flow, the key constitutive relations that exist in the literature are highly dependent on the flow properties. Therefore, the application range of each relation is limited. Such modelling was used in MCCI research for void fraction determination in corium due to release of gases from heating up concrete, where the gas flow rates are extremely low [52] [53]. During bottom cooling, the steam flows upwards through the molten corium with high flow rates, therefore the flow range limitations of existing drift flux models should be considered.

2.3 COCOMO 3D Code

COCOMO3D (COrium COolability MOdel - 3 Dimensional) is a three-dimensional integral thermal-hydraulic code being developed in IKE for simulating the processes during the late phase of a severe accident in LWR. COCCOMO3D integrates the features of the existing codes JEMI (Jet Fragmentation and Premixing) [54] and MEWA (MElt and WAter) [55]. The code JEMI, which was developed at IKE, describes the fragmentation of a molten jet pouring into the water, mixing, cooling the fragments and the formation of a debris bed [56]. The code MEWA, also developed at IKE, describes the two-phase flow of steam and water in a porous geometry resulting from degradation of core or from formation of a particulate debris bed by melt-water interaction, in-vessel or ex-vessel [57]. The code MEWA consists of the modules MESOCO (MElting SOlidification COde) [58], describing the processes in the core with massive melting, melt relocation, molten pool formation and behavior, and WABE (WAter and BEd) [59] [60], which describes the thermal-hydraulics of water and steam in a porous medium.

The current work investigates the hydraulics of liquid coolant flow through porous concrete and porosity build up in liquid corium upon interaction with coolant. The investigations are done with the assumption of isothermal conditions, focusing on the friction and momentum exchange. Therefore, the emphasis of this section will be on momentum exchange modelling in the code and relevant constitutive laws.

2.3.1 Conservation of Momentum

The current modelling in COCOMO3D adopts a multiphase, multi-component description based on the quasi-continuum approach. The phases/components (or fields) considered are viewed as interpenetrating quasi-continuous media, which are described by averaged conservation equations for mass, momentum and energy. Mass, momentum and energy fluxes that are exchanged locally at internal boundaries are considered in the form of volumetric sources or sinks for the respective phases or components. In the current modelling there are three phases considered: solid, liquid and gas. These phases are considered to fill the total volume as follows:

$$V = V_s + V_l + V_g \tag{2.20}$$

Prior to this work corium has been modelled in COCOMO3D as solid, either as moving solid particles or as fixed porous bed (debris bed). Cooling water is modelled as liquid and gas. For modelling of fluid flow through porous media the volume ratio of fluids to total volume is described as follows:

$$\varepsilon = \frac{V_l + V_g}{V_s + V_l + V_g} \tag{2.21}$$

Where ε is the porosity. The ratio of gas or liquid phase to the total fluid volume is described as follows:

$$s_i = \frac{V_i}{V_l + V_g} \quad , \qquad i = g, l \tag{2.22}$$

Where s is the saturation and indices g, l stand for gas and liquid phases respectively. For the pool flow where there are no solid media the saturation would be the volume fraction of each fluid phase. In this case, the volume fraction of gas, s_g, in other words the void fraction, α, is:

$$\alpha = s_g = \frac{V_g}{V_l + V_g} \tag{2.23}$$

The general expressions for the momentum conservation of gas and liquid in COCOMO3D are in non-conservative form. Meaning, they consider time derivatives, inertial terms, pressure gradient, gravity force, friction with fixed solid phase and interfacial friction between gas and liquid. The momentum conservation for gas phase and liquid phase are described respectively as follows:

$$\rho_g \left(\frac{\partial \vec{v}_g}{\partial t} + (\vec{v}_g \cdot \nabla)\vec{v}_g \right) = -\nabla p_g + \rho_g \vec{g} - K_{gs}\vec{v}_g - \frac{K_{gl}}{s_g}(\vec{v}_g - \vec{v}_l) \tag{2.24}$$

$$\rho_l \left(\frac{\partial \vec{v}_l}{\partial t} + (\vec{v}_l \cdot \nabla)\vec{v}_l \right) = -\nabla p_l + \rho_l \vec{g} - K_{ls}\vec{v}_l + \frac{K_{gl}}{s_l}(\vec{v}_g - \vec{v}_l) \tag{2.25}$$

Where ρ is density, $\vec{v}$ is the velocity vector, p is pressure, $\vec{g}$ is the gravitational acceleration, t is time and the indices g, l, s stand for gas, liquid and solid phases respectively. The left hand sides of the Equations (2.24) and (2.25) have the time derivatives and inertial terms, the right hand side of the equations have the terms for pressure gradient, gravity force, friction force between the fluid flow and fixed solid phase, and friction force between the fluids respectively. K_{gs}, K_{ls}, and K_{gl} are friction factors for friction forces between gas and porous fixed solid, liquid and porous fixed solid, and between liquid and gas respectively.

For modelling fluid flow through porous solid media, as in the Chapter 3 and Chapter 4 of this work, the momentum equations are governed mostly by pressure gradient, gravity force and friction with the solid phase. Therefore, the effects of time derivatives and inertial terms can be neglected. For the case of a pool flow however, as in the simulations for Chapter 5 of this work, the inertial terms and time derivatives of the momentum would have an effect on the momentum exchange between the liquid and gas phases. Therefore, for the two-phase pool flow, momentum conservation for gas phase and liquid phases are governed by pressure gradient, gravity force, interfacial friction between gas and liquid as well as the inertia terms and time derivatives. However as there are no solid materials involved in the two-phase pool flow, the forces due to friction with the solid phase can be neglected. The form of the momentum conservation equations that govern the simulations in the upcoming chapters of this work will be described explicitly in the relevant chapters.

2.3.2 Friction Laws

This section will provide a brief overview of the friction modelling in COCOMO3D for the cases relevant to this work, namely the liquid flow through porous media and the pool flow. The friction factors K_{gs}, K_{ls}, and K_{gl} in Equations (2.24) and (2.25) are assumed to have the following form that takes laminar and turbulent contributions to friction into account:

$$K_{gs} = K_{gs}^{lam} + K_{gs}^{turb}|\vec{v}_g| \tag{2.26}$$

$$K_{ls} = K_{ls}^{lam} + K_{ls}^{turb}|\vec{v}_l| \tag{2.27}$$

$$K_{gl} = K_{gl}^{lam} + K_{gl}^{turb}\left|\vec{v}_g - \vec{v}_l\right| \tag{2.28}$$

Superscripts lam and $turb$ are representing linear and turbulent contributions of the friction to the momentum. As it can be seen in these equations the turbulent term has the velocity in it, which results in the dependency of the momentum force on the square of the velocity when K_{gs}, K_{ls}, and K_{gl} are placed in the Equations (2.24) and (2.25).

In the existing modelling of flow through porous media in COCOMO3D, which models the coolant flow through a fixed debris bed, the coefficients K_{ls}^{lam} and K_{ls}^{turb} are described for single phase liquid flow as follows:

$$K_{ls}^{lam} = \frac{\mu}{k} \quad ; \quad K_{ls}^{turb} = \frac{\rho}{\eta} \tag{2.29}$$

It can be seen that the coefficients K_{ls}^{lam} and K_{ls}^{turb} are based on Darcy's law and the Forchheimer Equation, see Equations (2.5) and (2.7). With the existing modelling of the code, permeability and passability values in the coefficients are calculated based on porosity and particle diameter of the packed bed. However, due to being a consolidated porous material, this approach may not be accurate for porous concrete, therefore permeability and passability values are traditionally determined experimentally. Chapter 3 and Chapter 4 of this work will discuss the applicability of these friction laws for flow through porous media and Chapter 4 will investigate experimentally the actual friction relations for prototypical porous concretes.

In the existing code, two-phase pool flow for steam and water is modelled based on the two-fluid method. In this modelling, the two-phase flow between water and steam is assumed to have three flow regimes: a bubbly dispersed flow regime up to 0.3 void fraction (gas volume ratio), a droplet dispersed flow regime beyond 0.7 void fraction, and a transition regime in between. The transition regime assumes a co-existence of bubbly and droplet flow. The velocity of the gas phase, $\vec{v}_g$, and the velocity of the liquid phase $\vec{v}_l$ have single value respectively across different flow regimes at any given time. This is also reflected in momentum conservation Equations (2.24) and (2.25) as there is just one set of conservation equations with a single value of velocity for each phase.

The friction force between water and steam in the momentum equation is modeled based on Ishii's modelling of standard drag force in multi particle dispersed flow, see Equation (2.14). As the drag coefficient in the drag force equation inherently bring the effects of laminar and turbulent flow, K_{gl}^{lam} for the pool flow is assumed as $K_{gl}^{lam} = 0$ in COCOMO3D. For the dispersed flow regimes (bubbly and droplet flow) K_{gl}^{turb} is modelled as a function of drag coefficient C_D as follows:

$$K_{gl}^{turb} = -\frac{3}{8}\frac{s_d}{r_d} C_D \rho_c \tag{2.30}$$

For the transition flow where two regimes co-exist, the friction factor for the transition region is averaged from the friction factor of bubbly and droplet regions based on two methods: As proposed by Meignen et al. [48] and as proposed by Vujic [61].

Although two-phase pool flow is modelled in COCOMO3D, it applies only to water-steam two-phase flow, but not to the physical properties of molten corium and high velocity high temperature steam flow through molten corium. Moreover, existing friction laws assume gas continuous regime for higher void values and highly simplified versions of the drag coefficient, C_D from Ishii's approach. In COMET research on the other hand, high porous solidified post-test blocks indicate to a high void liquid continuous flow regime for melt-coolant flow. And although Ishii's drag force approach and drag coefficients are known to be valid for large ranges of flow properties and materials, great care must be taken with the application to two-phase flow of two different liquids. Chapter 5 of this work will discuss further the friction laws for two-phase pool flow for molten corium and steam and the existing shortcomings.

2.3.3 Short Description of the Numerical Solution Method

In COCOMO3D the mass, momentum and energy conservation equations are given in the form of partial differential equations. Spatial discretization based on a finite volume method is applied to estimate the spatial derivatives. Cylindrical coordinates and an orthogonal, staggered grid are applied in spatial discretization. Scalar quantities like pressure, temperature and volume fractions are defined at cell centers, while the components of vector quantities like velocity and mass flux are defined on the cell faces. For approximation of the time derivatives in COCOMO3D the first order backward differences quotients (implicit Euler method) are used. Due to this implicit time discretization, the mass and momentum conservation equations (as well as the energy conservation equations) have to be solved iteratively. This iterative process is done by COCOMO3D as follows: First, the momentum equations for gas and liquid are solved for the gas and liquid velocities, using actual values of saturation and pressure. Then, the velocities are inserted in the mass conservation equations of gas and liquid. By applying a Newton type method, the mass conservation equations are used to calculate corrections to the pressure and saturation, such that the mass flow rates calculated with the corrected pressures and saturations satisfy the discrete mass conservation equations. This involves the linearization of the terms in the mass conservation equations with respect to saturation and pressure, including the dependence of the velocities on these. After the update of pressure and void fractions, the energy equations of liquid and vapor are solved separately. Linearization with respect to the respective temperatures yields linear systems, from which temperature corrections are calculated. Due to the non-linearity and coupling between equations, an iterative procedure is required. The above steps of the iterative solution procedure are therefore repeated within the actual time step until sufficient convergence is reached.

3 Optimization of Hydraulic Parameters of a Porous Concrete Core Catcher

In order to enable the cooling and solidification of the ex-vessel molten corium, the cooling water must be provided to the melt with sufficient flow rates for the heat removal. Previous experimental investigations have demonstrated the successful application of a porous concrete core catcher device in small or medium size systems up to a diameter of 1 meter. Such a geometry is still small compared to large containment cavities of an actual PWR. The key feature of the porous concrete core catcher device is that it should passively transport cooling water to the large surface area of a reactor cavity with the required flow rates. Considering this, it is essential to investigate the hydraulic properties of such a device in a larger geometry in terms of the capacity of providing sufficient cooling water to the corium in a uniform way. This investigation has a higher importance especially in the case of back fitting to existing reactors, where the available space and water connection possibilities to the device are more limited.

In this chapter, a methodology is developed in order to optimize the hydraulic parameters of a porous concrete core catcher device. Firstly, the outline of the core catcher device geometry and the target for the core catcher design is presented. Next, the effect of various parameters on core catcher performance in terms of coolant distribution and required pressure input is evaluated by single effect simulations. The relation between these various system parameters is investigated in order to provide uniform and sufficient flow rates to the corium. Based on the outcome of these single effect simulations, a methodology for optimizing the hydraulic properties is developed. Finally, the limitations due to existing knowledge of the porous concrete properties are discussed, in terms of the reactor application possibilities.

3.1 Definition of the Geometry of the Core Catcher

The core catcher device has a cylindrical structure, placed in the reactor cavity on top of the basemat and underneath the RPV. The diameter of the device should be large enough to collect the corium in case of a large RPV opening but should also be designed to fit to

an average available space in a Generation II PWR cavity. This available space is reduced with the back-fitting constrictions. As for the height of the concrete layers, the total height should bring a certain mechanical stability but, in the meantime, should be able to fit to the available space between the basemat and RPV, which is again further restricted for the back fitting with the instrumentation below RPV.

The sketch in Figure 3.1 is the representation of the geometry of a porous concrete core catcher device and its placement in a PWR cavity. Considering the dimensioning of a generic Generation II PWR [3], the outline of the porous concrete core catcher device dimensions for reactor application can be chosen as given in Table 3.1. These dimensions are applied to all reactor case simulations in this work. The diameter of the core catcher device, d_c, is assumed as 6 meter and the total height of the device is assumed as less than 0.5 meter [62]. The sacrificial layer on top of the porous concrete layers is assumed to have height, h_s, of 0.1 meter based on previous CometPC experiments. This leaves the total height of the porous concrete layers as less than 0.4 meter. Conservatively, the sum of the upper concrete layer height, h_u, and lower concrete layer height h_l is assumed as 0.32 meter.

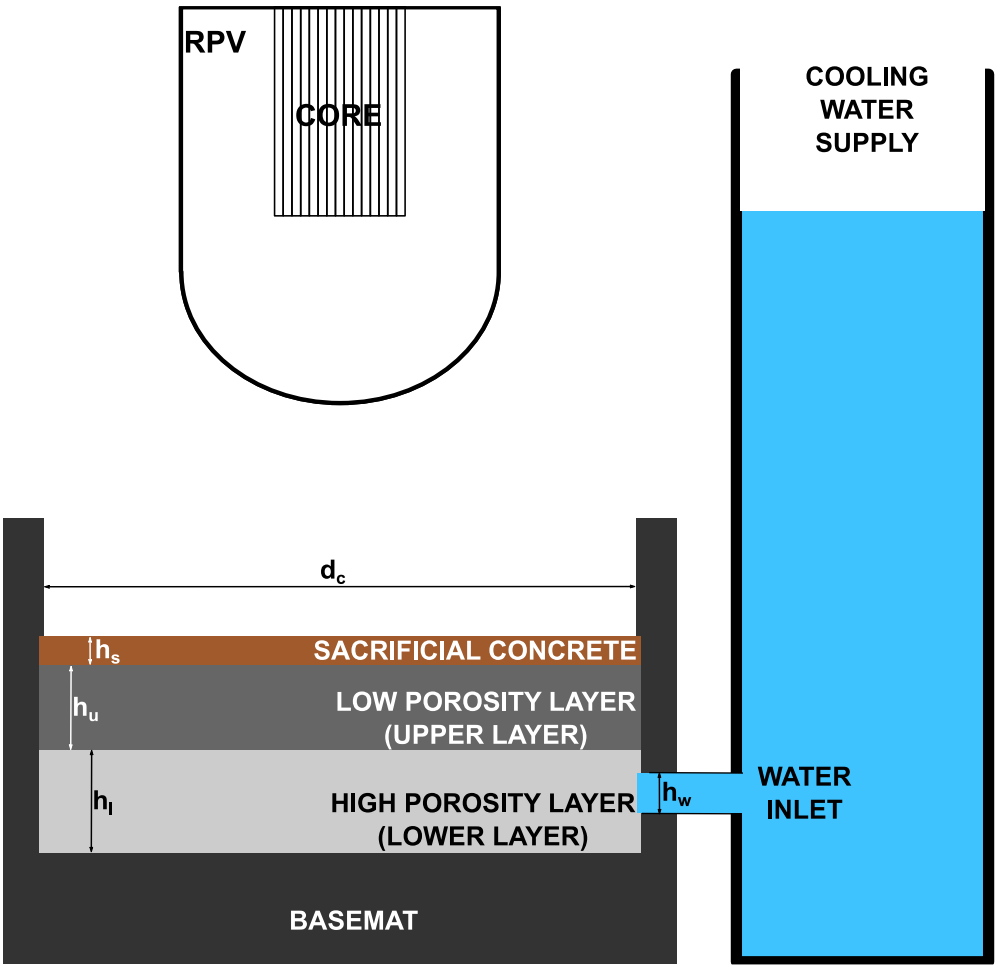

Figure 3.1 Sketch of the porous concrete core catcher device in a PWR cavity with dimensioning of the system. (Illustration of how it would be implemented in a reactor)

Table 3.1 Outline of the porous concrete core catcher device dimensions for reactor application.

Diameter of the device, d_c	6.00 m
Surface area of the device, A_c	28.27 m^2
Total height of the concrete layers, $h_u + h_l$	0.32 m
Height of sacrificial concrete layer, h_s	0.10 m
Height of cooling water inlet connection, h_w	0.03 m

3.1.1 Configuration of Cooling Water Inlet

Another aspect of the porous concrete core catcher design is the consideration of the cooling water tank connection. The cooling water should be passively provided from the circumference of the high porous layer of the device. Figure 3.2 demonstrates two different configurations for the cooling water inlet to the device. A single-point-inlet as seen in Figure 3.2 a is considered to be suitable for back-fitting application as it requires minimum interference. This is crucial for implementing a device into a reactor in operation. However, this type of singular inlet might bring higher loads to the system as the water inlet area is restricted. For a non-restricted design, for instance implementing the core catcher during the construction, a multi-inlet solution that distributes the coolant inlet around the circumference as seen in Figure 3.2 b would be more ideal design as it also divides the pressure load caused by the cooling water. In order to see the differences of their effect on optimization, both the restricted single inlet point connection and ideal circumferential inlet connection to the water supply for the core catcher device will be evaluated in this chapter. For these possible inlet configurations, the height of the water feed opening, h_w, is taken as 0.03 meter. For the single inlet point a 6° opening around the perimeter is assumed. Whereas for multi-inlet circumferential continuous 360° connection to water around the perimeter is assumed.

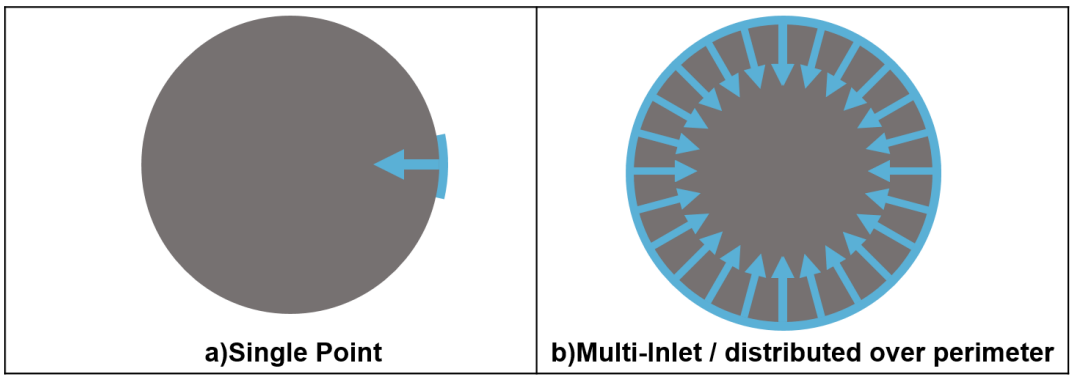

Figure 3.2 Two cooling water inlet configurations for porous concrete core catcher device. a) A single point water inlet with 6° wide opening at the side of the high porosity concrete layer. b) Circumferential inlet configuration with water inlet at entire perimeter of the high porosity concrete.

3.2 The Design Target for the Porous Concrete Core Catcher Device

The flooding water flow rate through the device shall ensure that the corium is quenched and solidified within a reasonable time. This reasonable time should be on one side fast enough to prevent basemat penetration by corium melt and on the other side not too quick to trigger containment failure due to over-pressurization caused by too fast water evaporation.

As discussed in Chapter 1.2.2, COMET-H and CometPC experiments simulated the maximum decay heat that could be reached by a PWR. In these experiments, the heat transfer from the corium, melt solidification and long-term heat removal process was represented one to one. The volume flow rates per contact surface area are around 1.5×10^{-3} - 2×10^{-3} m/s, one order of magnitude higher than required for the complete decay heat removal. The results show that this provides rapid cooling and successful solidification of the melt.

The corium coolability issue is dominated by the fission product decay heat rather than the sensible and latent heat of the corium, see Chapter 1.1.1. The fission product decay heat is a long-lasting source of internal heat generation and the cooling means should be capable of removing this heat from the corium. A typical Generation II PWR, which has a thermal operation power approximately between 2700 MWth and 4500 MWth depending on the type [3], would generate a decay heat as given on Table 1.1 after following a reactor shutdown [11]. The amount of corium on the reactor cavity and the decay heat which needs to be removed is accident scenario dependent. For the current work, as it was done in COMET research, the entire core inventory was assumed to be in reactor cavity 3 h after shutdown. This yields decay power value between 23 MW and 40 MW depending on the minimum and maximum operating power respectively.

Considering the latent evaporation heat of the water, 2256 kJ/kg, cooling water with a volume flow rate between 30-50 l/s would remove heat sufficiently above the decay heat just by evaporation. Assuming the corium spreads through the core catcher surface area with 6-meter diameter, this volume flow rate corresponds to volume flow rate per area (superficial velocity) of $1.1x10^{-3}$ – $1.8x10^{-3}$ m/s. These superficial velocities overlap with the superficial velocities that resulted in successful cooling and solidification in COMET research. For the current work cases with a few different volume flow rates in this range are investigated.

3.3 Porous Concrete Characteristics for the Core Catcher Device

In the very first CometPC experiments, mechanically not stable sand and gravel beds were used to make the porous bed, however it was clear that these layers needed stabilization [33]. It has been concluded that with an actual concrete that is permeable to water (pervious concrete or porous concrete) this stabilization can be achieved. Although during the later CometPC experiments actual pervious concretes were used, no information regarding the permeability of these concretes have been provided [23] [24]. The porosities of the concretes for these experiments are described as 30% for lower layer and 15% for upper layer, however, the porosity value alone does not determine the permeability of a porous concrete. Permeability of a porous concrete is the parameter that determines the hydraulic property of a porous concrete.

As a reference for the calculations in this work, various pervious concrete types from the literature have been surveyed. Table 3.2 presents the sample of pervious concrete types from the literature. As mentioned earlier the porosity values alone do not describe the permeability of a porous medium, however they are included in this table for insight. The porosity values marked with an asterisk * are open (effective) porosities. For initial calculations the concrete sample from D. H. Nguyen et al. [63] is used as upper layer and PC1 sample from A. Ibrahim et al. [64] is used as lower layer. The hydraulic conductivity values that are provided by the respective authors were used in Equation (2.2) with water properties at atmospheric conditions [65] to calculate the permeability values.

Table 3.2 Pervious concrete types from the literature. (The porosity values marked with an asterisk * are open (effective) porosities.)

Author	Concrete Sample Name	Hydraulic Conductivity [mm/s]	Porosity [%] (*effective)
B. Huang et al. [66]	LSAM 6	0.58	10.7 *
	LSAM 10	12.65	22.6 *
	D_508 16	24.7	30.5 *
A. Ibrahim et al. [64]	PC1	17.9	35
	PC8	21.4	35
	PC20	27.5	38
	PC22	15.0	30
M. U. Maguesvari et al. [67]	M1F0	12.58	40.91
	M2F20	10.29	35.67
	M4F40	4.80	30.01
D. H. Nguyen et al. [63]	———	1.8	26.5 / 17.2 *
R. Zhong et al. [68]	UHSM-2.5-1.19	0.25	19.84 / 9.5*
	UHSM-3.0-1.19	1.21	24.65 / 15.7*
	NSM-3.0-4.75	5.40	28.59 / 25.09*

3.4 Single Effect Simulations for Hydraulic Properties of a Porous Concrete Core Catcher

In this section, the separate effects of the porous concrete permeability, porous concrete thickness and total volume flow rate of the cooling water on the water distribution and pressure values are investigated in single-phase flow simulations.

The simulations were carried out in COCOMO3D. Figure 3.3 shows the sketch of the simulation domain. As it can be seen in this sketch, the sacrificial layer on top of the porous concrete layer is assumed as completely ablated leaving a free path towards the corium layer. The core catcher geometry is built in COCOMO3D in a cylindrical coordinate system that has the origin at the center of the base surface of the lower concrete layer. The radius of the core catcher is defined in radial direction and the height of the core catcher layers are defined in axial direction of the coordinates. The angular direction defines the place and the opening of the water inlet.

As a cooling water inlet configuration for initial simulations, cooling water is distributed over the entire perimeter of the device, see Chapter 3.1.1. The water inlet configuration top view is seen in the top right corner of Figure 3.3 as a guidance, the red line is the top of the section that is seen in detail. The circumferential inlet configuration brings a cylindrical symmetry to the system, which allows for carrying out the water flow simulations with decreased computational load.

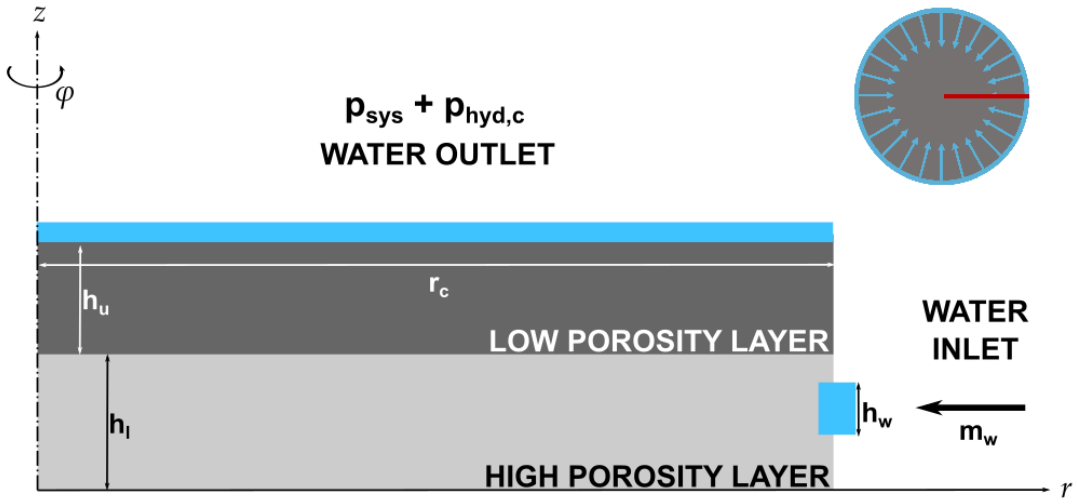

Figure 3.3 Sketch of COCOMO3D simulation domain for the porous concrete core catcher device.

At the flow inlet, the mass flow rate of cooling water, m_w, and corresponding mass flux for the inlet area is imposed as boundary condition. The mass flux of the cooling water is calculated for the desired volume flow rate of the cooling water with water inlet area, which is 0.56 m² for a 0.03 m high continuous circumferential water inlet. At the flow outlet, the total of system pressure, p_{sys}, and hydrostatic pressure of melt layer, $p_{hyd,c}$, with 0.5 m height and 6000 kg/m³ density [69] [70] were imposed as boundary condition. The system pressure, p_{sys}, is kept at 101.35 kPa which gives a total pressure of 130.78 kPa at the water outlet. The boundary condition at the flow outlet is accident dependent and given here for better comprehension of the values seen in simulation results. The important value to determine here is the total pressure loss in the porous core catcher device and its relation to other device parameters, and to the coolant flow, which is independent from boundary condition $p_{hyd,c}$ and p_{sys}.

In COCOMO3D code the porous medium properties permeability and passability are calculated with Darcy or Ergun laws based on effective porosity and aggregate diameter. Arbitrary values were assigned to these parameters in order to reach designated permeability values for the hydraulic calculations. Since the pervious concrete literature only provides permeability values for the concretes, for initial simulations, the passability

value in the flow model in COCOMO3D is assigned to an extremely high value. A sufficiently high passability value gives a linear relation between pressure difference (pressure loss due to friction) in the concrete and the superficial velocity, which should be applicable for the superficial velocity values reached in the system for circumferential water inlet configuration (0.05-0.1 m/s).

3.4.1 Initial Simulation Case

For the first simulation case, the design target is 1.5 x10^{-3} m/s volume flow rate per unit surface area of corium and porous concrete core catcher contact. This value is in agreement with previous CometPC experiments, and also within the range of required flow rates that was discussed in Chapter 3.2. For a core catcher device with 6 m diameter and 28.27 m^2 surface area for corium contact, this means 42.41 l/s total volume flow rate or 42.23 kg/s total mass flow rate should be provided in coolant inlet. Considering the water inlet area, this means 74.67 kg/m^2s mass flux applied at the cooling water inlet boundary of the simulation. As mentioned in Chapter 3.3, a higher permeable concrete for lower layer [64], and a lower permeable concrete for the upper layer [63] of the device has been selected for this first calculations. The heights of these different concrete layers are taken as equal.

For the first simulation case, the targeted superficial velocity of cooling water, j_w, and input parameters are summarized in Table 3.3.

Table 3.3 Input parameters for the first simulation case of water flow through porous concrete layers.

	Initial Simulation Case
Design target, j_w	1.5 x10^{-3} m/s
Permeability of upper layer, k_u	1.63x10^{-10} m^2
Permeability of lower layer, k_l	1.46x10^{-9} m^2
Height of upper layer, h_u	0.16 m
Height of lower layer, h_l	0.16 m
Radius of the device, r_c	3 m
Height of water inlet, h_w	0.03 m
Mass flow rate of cooling water at the system inlet, $\dot{m}_w$	42.23 kg/s

With given geometry and other input parameters the code calculates the superficial velocity in the porous concrete layers and on the top surface of the upper concrete layer, as well as the total pressure difference in the porous concrete layer. Figure 3.4 shows the simulation results on the porous concrete layers for the initial simulation case.

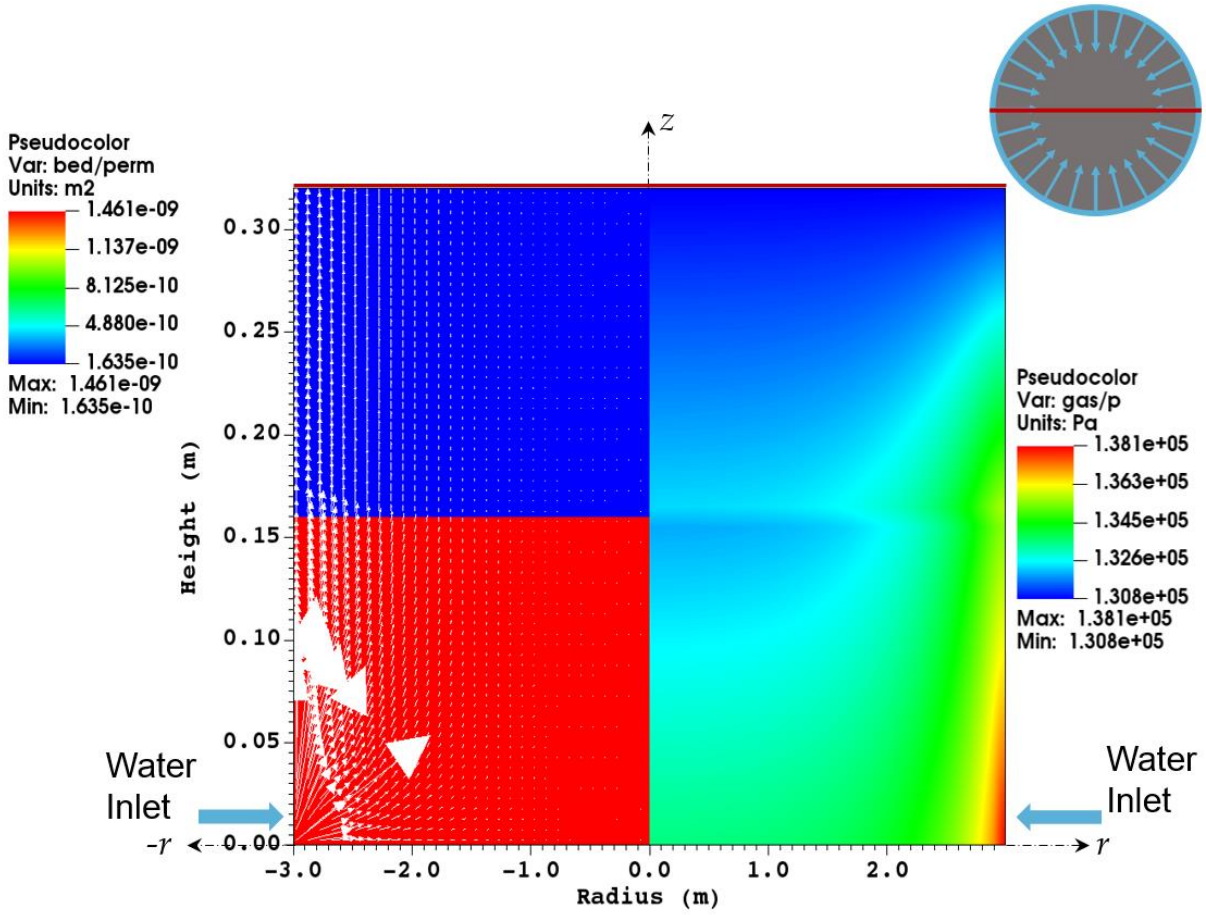

Figure 3.4 Simulation results for the water flow through porous concrete layers for the first case. Left: permeability and vectoral representation of the cooling water flow. Right: Pressure distribution. The top view of core catcher on the upper right corner as a guide for the cross-section location.

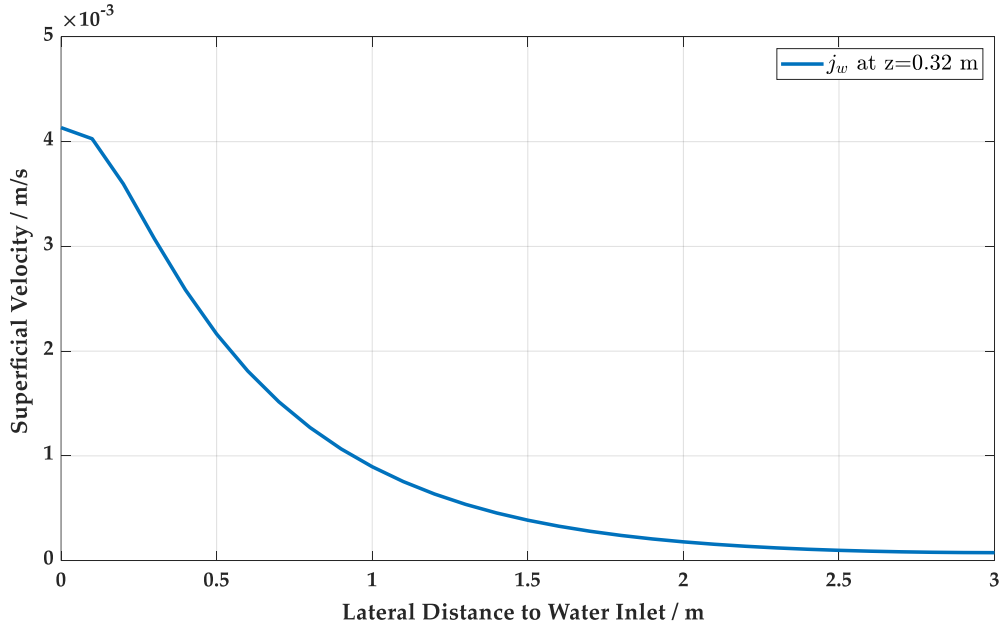

Figure 3.5 Superficial velocity of the cooling water at z=0.32 (the contact surface of corium and upper concrete layer) in axial direction for the initial simulation case.

A vertical cross section of the porous concrete core catcher device is shown in Figure 3.4 that represents the simulation results. The location of the cross-section is marked on the top view of the core catcher as a guidance in the upper right corner of the figure. The radial coordinate, *r*, indicates the radius of core catcher, and the axial coordinate, *z*, indicates the height of the core catcher. The water inlet locations on the sides are indicated for guidance on the figure as well. On the right-hand side of the figure the pressure distribution in the porous concrete layer can be seen. In order to have a better understanding of the pressure values shown in the legend of the figure: In this case the total pressure difference in the porous concrete core catcher yields 7.32 kPa, which requires an inlet water pressure of 138.1 kPa for the described system pressure and corium load. It should be mentioned here that the pressure values are obtained in the mesh center. Therefore, the minimum pressure value observed in simulation result figures could be higher that the outflow pressure value given as boundary condition, which is the real minimum pressure value that was taken to calculate the pressure difference in the porous concrete layers. On the left-hand side of the figure the two porous concrete layers can be identified with their different permeability values, red color represents the permeability value 1.46×10^{-9} m² of the lower layer and blue color represent the permeability value 1.63×10^{-10} m² of the upper layer. On this side of the figure, white arrows represent the volume flow rate of the cooling water. As it can be seen by the size and the direction of the arrows, the cooling water rises mostly upwards immediately after entering the bottom concrete layer. The volume flow rate is not limited enough by the upper concrete layer, so instead continuing to flow in radial direction in the bottom concrete layer the water prefers the upward path. The cooling water eventually reaches to the surface of the upper concrete layer (the contact surface of corium and porous concrete core catcher device, indicated with a red straight line at $z = 0.32$ m) mostly near the perimeter of the core catcher, and very little amount of water rises in the middle section. The actual distribution of the superficial velocity of cooling water on this surface in axial direction is shown in detail on the diagram on Figure 3.5.

Figure 3.5 shows the distribution of flooding volume flow rate per unit area (superficial velocity) of the cooling water on the contact surface of corium and upper concrete layer ($z = 0.32$ m). The superficial velocity reaches in the vicinity of water inlet as high as 0.005 m/s and after 1 meter drops down to 0.001 m/s which is already below the aimed volume flow rate per surface area for this simulation case. Moreover, a large area with 1 meter radius in the middle of the cavity is reached by almost no cooling water. Clearly, this case is much below optimal. Most of the cooling water accumulates on the sides while the middle section of the corium is not injected by water from below. The reason behind this is the fact that the water resistance of the upper concrete layer is not high enough for this system. Instead of limiting the upwards water flow, it allows water to rise rapidly in the vicinity of water inlet. This lateral water distribution problem could be solved by decreasing the permeability of the top concrete layer.

3.4.2 Influence of Porous Concrete Permeability

In order to observe the influence of concrete permeability on water flow rates and distribution, the permeability of the top concrete layer is reduced systematically while the other parameters were kept the same as the initial simulation case (see Table 3.4). The boundary conditions were also kept the same as for the initial case, which means the total volume flow rate for the system is 42.41 l/s with the target volume flow rate per unit surface area of 1.5 x10^{-3} m/s. After a number of permeability values that were simulated for the top concrete layer, it was found that with the permeability value of 1.96x10^{-12} m² the flooding cooling water flow rate towards corium layer is uniform along the contact surface. The results of this simulation case are shown in Figure 3.6.

Table 3.4 Input parameters for the simulation with altered upper layer permeability.

	Initial Simulation Case	Uniform Superficial Velocity (Reference Case hence forth)
Design target, j_w	1.5 x10^{-3} m/s	
Permeability of upper layer, k_u	1.63x10^{-10} m²	1.96x10^{-12} m²
Permeability of lower layer, k_l	1.46x10^{-9} m²	
Height of upper layer, h_u	0.16 m	
Height of lower layer, h_l	0.16 m	
Radius of the device, r_c	3 m	
Height of water inlet, h_w	0.03 m	
Mass flow rate of cooling water at the system inlet, $\dot{m}_w$	42.23 kg/s	

Similar to the Figure 3.5 a vertical cross section of the porous concrete core catcher device is shown on Figure 3.6 that represents the simulation results. The total pressure difference along the concrete layers is 104.22 kPa. Compared to the initial simulation case a drastically higher pressure losses in the core catcher is observed, mainly in the top concrete layer. The reason of this high pressure difference is the fact that in this simulation case the permeability of the top concrete layer is drastically lower, hence it has a high water resistance which increases the pressure loss. In this case, by the white arrows and their size it can be distinguished that cooling water could spread better in lateral direction along the bottom concrete layer. Although through this layer still considerable amount of water rises immediately after the inlet point, it can be clearly observed that the less permeable upper layer limits the water flow and a very even water flow reaches the surface. The diagram on Figure 3.7 shows the actual superficial velocity distribution on the surface of the porous concrete core catcher device.

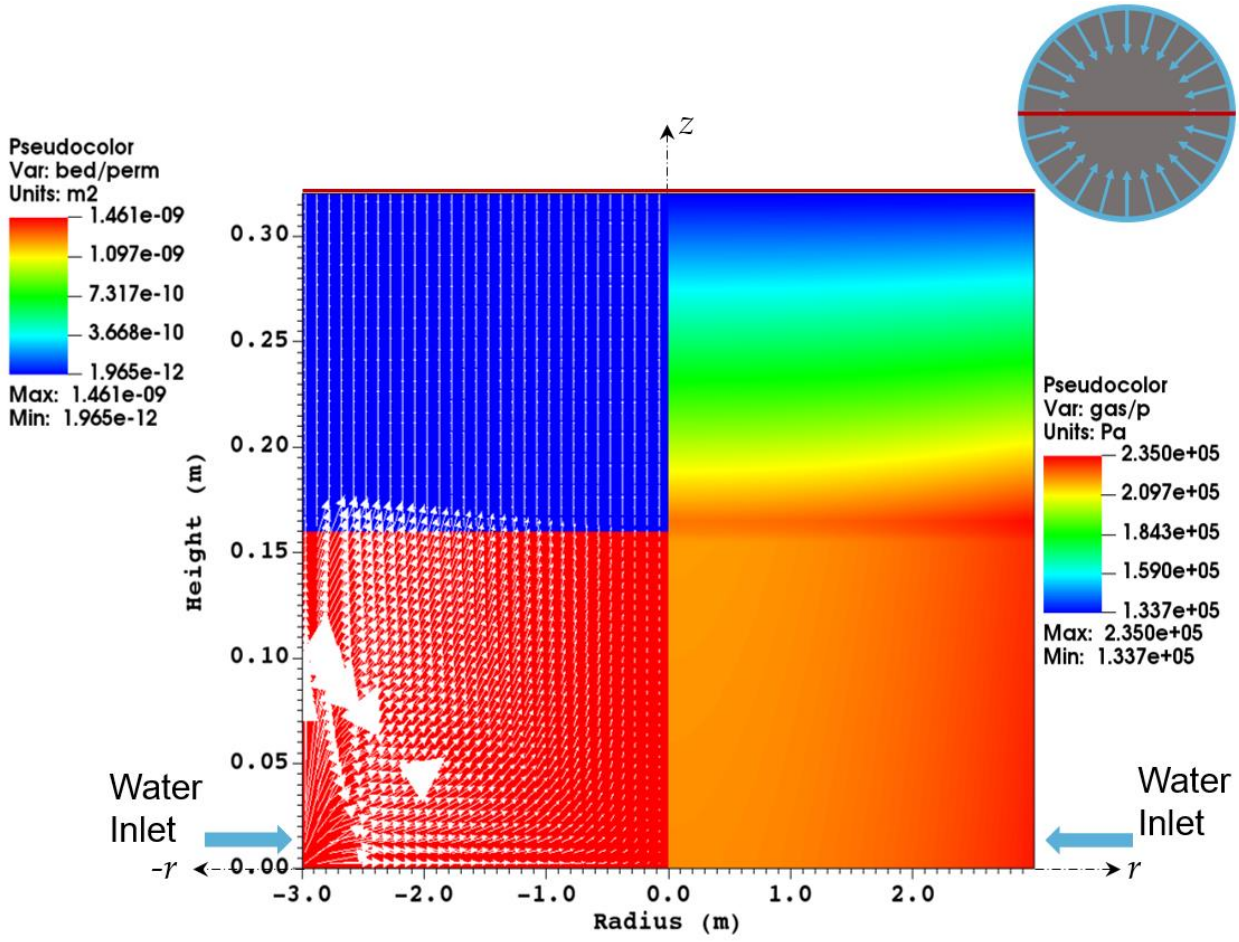

Figure 3.6 Simulation results for the water flow through porous concrete layers with new permeability for upper concrete layer. Left: permeability and vectoral representation of the cooling water flow. Right: Pressure distribution.

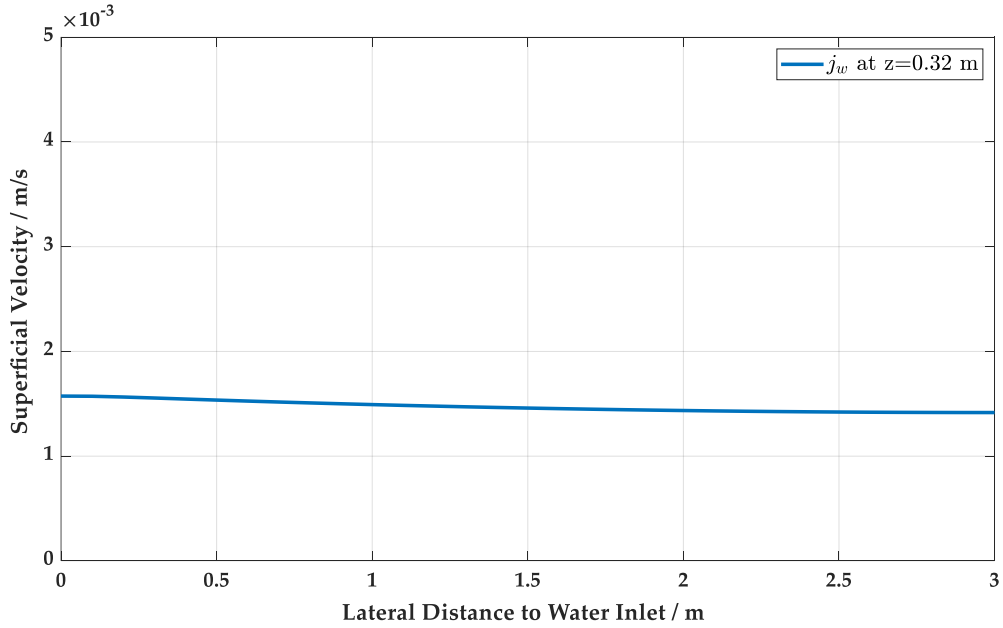

Figure 3.7 Superficial velocity of the cooling water at z=0.32 m (the contact surface of corium and upper concrete layer) in axial direction for new upper layer permeability.

This simulation case shows that the permeability values of upper and lower concrete layers have an influence on the distribution of the coolant flow on the concrete corium contact surface. One of the aims with the core catcher device to ensure the coolant water is distributed uniformly along the contact surface. Therefore, the simulation case where the uniform superficial velocity is reached is used as the reference case during the further investigations on the hydraulic properties of the core catcher device in this work henceforth.

3.4.3 Further Single Effect Simulations and Outcome

Further single effect simulations are performed for different core catcher height and different total mass flow rate of the coolant. The figures with the results of these simulations can be seen in Appendix A.

The simulations so far assumed the heights of the different porosity layers equal. Assuming that the heights of the upper and lower concrete layers of the system are required to be taken with different heights due to mechanical stability reasons, the influence of the concrete layer thickness to the cooling water flow would be another consideration for the design of the core catcher. In order to explore this effect, simulations were performed with different height ratios of the concrete layers to each other while keeping the total height of the device the same. The set of input parameters used in the simulation is shown in Table 3.5. The simulations case from the Chapter 3.4.2 is taken as a reference case so the permeabilities of the layers were taken from this simulation case.

Table 3.5 Parameters for the simulation with altered concrete layer thicknesses.

	Reference Case	Thicker Upper Layer	Thinner Upper Layer
Design target, j_w		1.5 x10^{-3} m/s	
Permeability of upper layer, k_u		1.96x10^{-12} m^2	
Permeability of lower layer, k_l		1.46x10^{-9} m^2	
Height of upper layer, h_u	0.16 m	0.24 m	0.08m
Height of lower layer, h_l	0.16 m	0.08 m	0.24 m
Radius of the device, r_c		3 m	
Height of water inlet, h_w		0.03 m	
Mass flow rate of cooling water at the system inlet, $\dot{m}_w$		42.23 kg/s	

In comparison to the reference case, changing the ratio of concrete layer thickness does not show considerable effect on the coolant distribution, see Figure A.1 - Figure A.3 in Appendix A. However, it has an effect on the total pressure difference in the core catcher, see Figure A.1 and Figure A.2 in Appendix A.

Another aspect of the design that is analyzed is the effect of change in targeted water flow rate to the simulation outcome. In order to investigate this effect another set of simulations was performed. The simulations case from the Chapter 3.4.2 is taken again as a reference so the permeabilities and geometry of the layers are same with this simulation case. For the new simulations the aimed superficial velocity is 1.2 x10^{-3} m/s and 1.7 x10^{-3} m/s. In order to reach this velocity on the entire contact surface of core catcher device and the corium, 33.78 kg/s and 47.86 kg/s mass flow rate of cooling water is imposed to simulations as boundary condition at the inlet respectively. The outlet boundary condition is imposed the same as the reference case simulation. Table 3.6 summarizes the input parameters of the simulations.

Table 3.6 Parameters for the simulations with altered cooling water mass flow rate.

	Reference Case	Lower Mass Flow Rate	Higher Mass Flow Rate
Design target, j_w	1.5 x10^{-3} m/s	1.2 x10^{-3} m/s	1.7 x10^{-3} m/s
Permeability of upper layer, k_u		1.96x10^{-12} m²	
Permeability of lower layer, k_l		1.46x10^{-9} m²	
Height of upper layer, h_u		0.16 m	
Height of lower layer, h_l		0.16 m	
Radius of the device, r_c		3 m	
Height of water inlet, h_w		0.03 m	
Mass flow rate of cooling water at the system inlet, $\dot{m}_w$	42.23 kg/s	33.78 kg/s	47.86 kg/s

With altered mass flow rate through the porous concrete system, the total pressure difference in the system increases or decreases proportionally to the total mass flow rate, see Figure A.4 and Figure A.5 in Appendix A. However, the uniformity of the superficial velocity is not affected by that, see Figure A.6 in Appendix A.

Table 3.7 summarizes the total pressure difference in the core catcher observed as a result of each single effect simulations in this Chapter.

Table 3.7 Total pressure difference in the porous concrete core catcher as a result of single effect simulations.

Simulation Cases	Total Pressure Difference in Core Catcher, Δp
Initial Simulation Case (Non-Uniform Superficial Velocity)	7.32 kPa
Reference Case (Uniform Superficial Velocity)	104.22 kPa
Thicker Upper Layer	159.32 kPa
Thinner Upper Layer	52.72 kPa
Lower Mass Flow Rate	80.00 kPa
Higher Mass Flow Rate	115.40 kPa

The initial simulation case yields a non-uniform distribution of the superficial velocity on the contact surface of corium and core catcher. This means that in the center of the core catcher there is very little to zero water injection to the corium. By decreasing the upper layer permeability, a uniform distribution of the superficial velocity is achieved. However, as seen in Table 3.7, the pressure loss in the core catcher ends up being drastically higher. This means, for the same design target and boundary conditions, higher input pressure for the coolant water is required which can cause higher pressure load on the core catcher and design challenges for the passive water pressure head. Accepting a relatively non-uniform water distribution helps reducing this pressure requirement. However, having a concrete pair that brings a non-uniform water distribution means the total amount of water provided in the system should be higher than the in the case of a uniform distribution, so the center of the cavity can also receive the required amount of water in order to remove the heat from the molten corium. As seen in Table 3.7 increasing the total mass flow of the coolant results in increased pressure for coolant input as well. It is challenging to keep the pressure loads to the system reasonably low while providing sufficient cooling water to the corium throughout the contact surface. Therefore, an optimization methodology is developed in this work which can be applied to different boundary conditions or design target.

3.5 Optimization Methodology for Coolant Flow through Porous Concrete Core Catcher

It is essential that the porous core catcher is able to provide sufficient cooling water into the corium throughout the cavity while keeping the required pressure head for the passive inflow at a reasonable value. The single effect simulations showed that having the cooling water distribution very strictly uniform or less uniform can both have their advantages and disadvantages in terms of required total coolant flow rate and required input pressure for the flow. On the other hand, the porous concrete itself could have limitations in terms of manufacturing with required mechanical stability and permeability. Therefore, it is challenging to determine the optimal hydraulic properties for the porous core catcher for providing sufficient cooling water into the melt successfully.

In order to overcome this challenge, a methodology is developed in this chapter for optimizing the hydraulic parameters of the porous concrete layers in order to achieve the desired water superficial velocity and pressure. It is acknowledged that the actual conditions in the reactor cavity are highly accident dependent. The methodology in this chapter is developed independently of the loads and can be applied for any given boundary conditions. This optimization can show optimum possible combinations for hydraulic parameters which can be beneficial for design decisions.

The final aim of the core catcher design is to provide cooling water along the whole contact surface with sufficient superficial velocity. Two different optimization criteria are defined in this methodology:

Optimization criterion 1: This is the more straining criterion in terms of uniform distribution of water. The axial component of the superficial velocity of the cooling water at the core catcher and corium contact surface can vary by only 10%, which can be assumed as a sufficient reasonable uniformity. Meaning, the difference between maximum superficial velocity and minimum superficial velocity on the surface is 10% of the maximum superficial velocity.

Optimization criterion 2: This criterion allows the axial component of the superficial velocity of the cooling water at the core catcher and corium contact surface to vary by 30%. Therefore, it is less straining than the optimization criterion 1.

Figure 3.8 shows the outline of the optimization method. The single-phase flow of cooling water through the porous concrete layers is simulated by COCOMO3D as shown in single effect simulations in Chapter 3.4. Optimization is done by a standalone simulation program that is coupled to COCOMO3D. For a given set of constant parameters and the solution parameter that are defined to COCOMO3D as input, the optimization program acquires the COCOMO3D output file and iterates the solution variable (the permeability of upper concrete layer) until the given optimization criterion is matched. The optimization criterion 1 and the optimization criterion 2 are applied separately.

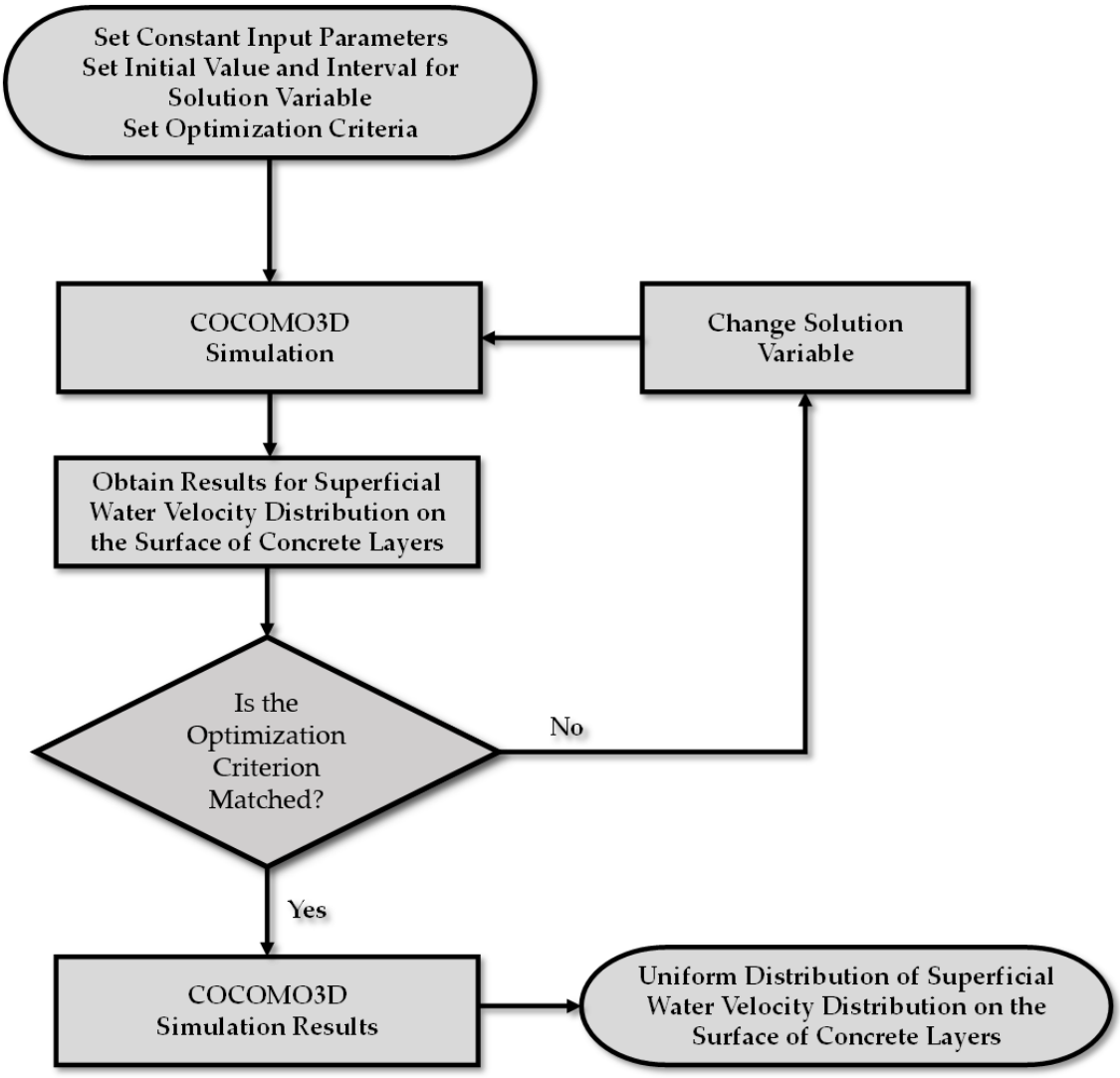

Figure 3.8 Outline of optimization method.

The total geometry of the core catcher, water inlet configuration and the boundary condition at the water outlet are applied similar to the single effect simulation in Chapter 3.4. Initially, the height of each concrete layer, mass flow rate at the inlet for the aimed average superficial velocity and permeability of the lower concrete layer are defined for the COCOMO3D simulations as in the reference case from Chapter 3.4.2. While other parameters were kept constant, the optimization program iterates the upper layer permeability, which is the solution parameter, until the optimization criterion is matched. This optimization process was then repeated for a great number of lower layer permeability values between 8.15×10^{-11} m^2 and 2.6×10^{-8}.m^2.

Figure 3.9 shows the relation between the permeability of lower concrete layer and the permeability of upper concrete layer to realize the defined optimization criteria. Figure 3.10 shows the resulting pressure difference in core catcher in relation to lower layer permeability (the upper layer permeability is paired as seen in Figure 3.9). Note that the x-axis in Figure 3.10 is shown in logarithmic scale in order to better depict the shape of the curve for lower values of the permeability. In both Figure 3.9 and Figure 3.10 , solid

line is the relation between the two parameters where the average superficial velocity, $\bar{j}_w$, of 0.0015 m/s is reached while realizing the optimization criterion 1 (Crit. 1) and dashed line represents the relation between the two parameters where the average superficial velocity of 0.0015 m/s is reached while realizing the optimization criterion 2 (Crit. 2).

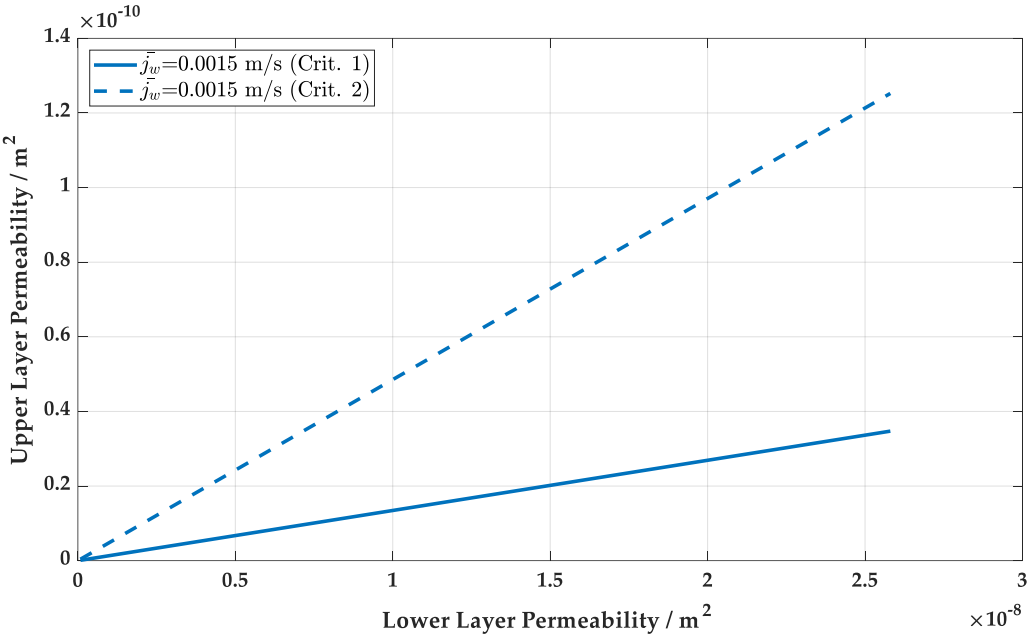

Figure 3.9 Relation between permeability values of two porous concrete layers that fulfills each optimization criterion for average superficial velocity of 0.0015 m/s. Solid line: Crit. 1 is fulfilled, dashed line: Crit. 2 is fulfilled.

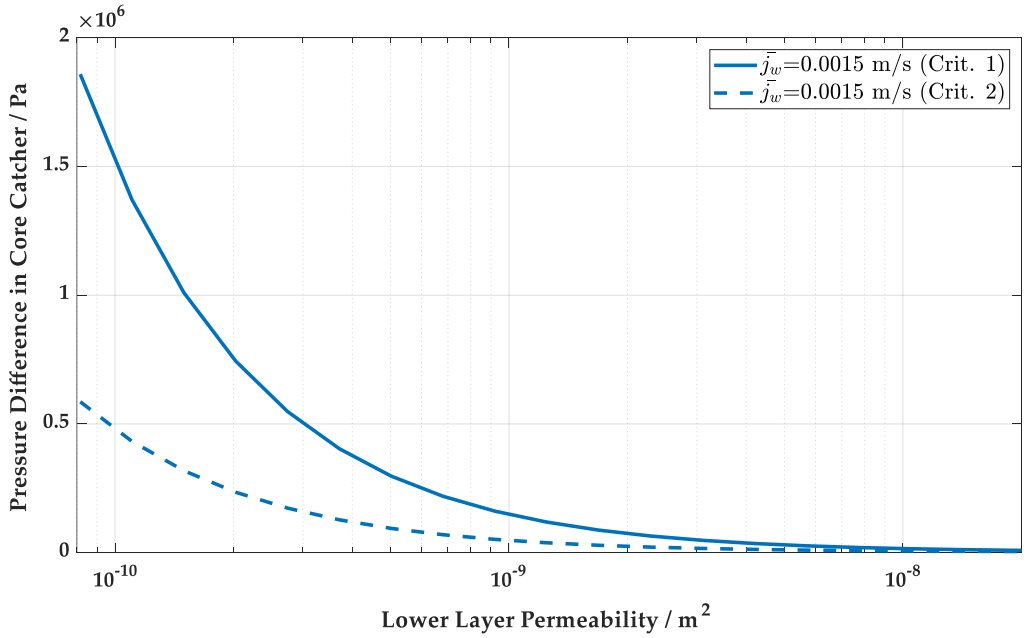

Figure 3.10 Change in pressure difference in the core catcher in relation to lower layer permeability when the upper layer permeability fulfills each optimization criterion for average superficial velocity of 0.0015 m/s. Solid line: Crit. 1 is fulfilled, dashed line: Crit. 2 is fulfilled.

As it can be seen in the Figure 3.9, for constant mass flow rate and core catcher geometry, the upper layer permeability linearly increases with increasing lower layer permeability. Fulfilling the optimization criteria 1, which is a very uniform distribution of the cooling water, requires lower permeability values for upper concrete layer as expected from the single effect simulations.

The total pressure difference in the core catcher decreases with increasing permeability of lower and upper layer for the constant mass flow rate and geometry as seen in Figure 3.10. As expected, more uniform distribution of the cooling water (optimization criterion 1) results in higher pressure difference in the core catcher as the upper layer for this case is less permeable.

As discussed earlier, while compromising between uniform water distribution and amount of total water flow rate, the maximum inlet pressure and realistic porous concrete structure can play a role for actual design decisions. In order to gain a better understanding of the parameter dependencies and to demonstrate possible parameter combinations, the optimization method was applied to 5 different design targets (with 5 different mass flow rates at the inlet), and 3 different concrete layer height ratios. These values can be seen on the Table 3.8. In the next sections, the relation between these parameters that realizes the optimization criteria is presented.

Table 3.8 Input parameters that optimization simulation is applied.

Parameter	Variations				
Design target, j_w	1.0 x10^{-3} m/s	1.2 x10^{-3} m/s	1.5 x10^{-3} m/s	1.7x10^{-3} m/s	2.0x10^{-3} m/s
Height of upper layer, h_u	0.16 m		0.24 m		0.08m
Height of lower layer, h_l	0.16 m		0.08 m		0.24 m
Mass flow rate of cooling water at the system inlet,$\dot{m}_w$	28.15 kg/s	33.78 kg/s	42.23 kg/s	47.86 kg/s	56.30 kg/s

3.5.1 Optimization of Systems with Different Mass Flow Rates

For the same concrete layer heights ($h_u = h_l = 0.16\,m$), the optimization simulations are performed for different design targets for superficial velocity, hence different coolant mass flow rates through the system, see Table 3.8.

Figure 3.11 shows the relation between the permeability of lower concrete layer and the permeability of upper concrete layer for 5 different cases of aimed average superficial velocity. Figure 3.12 shows the resulting pressure difference in core catcher in relation to lower layer permeability for these cases (the upper layer permeability is paired as seen in Figure 3.11). In both Figure 3.11 and Figure 3.12, solid line is the relation between the

two parameters where each average superficial velocity is reached while realizing the optimization criterion 1 (Crit. 1) and the dashed line represents the relation between the two parameters where each average superficial velocity is reached while realizing the optimization criterion 2 (Crit. 2).

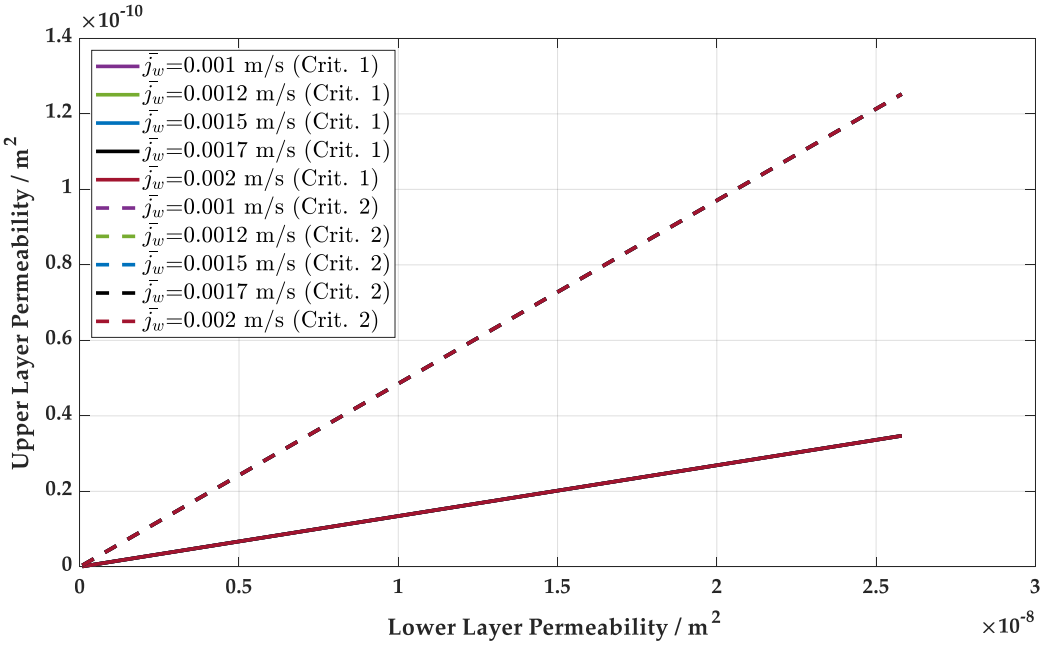

Figure 3.11 Relation between permeability values of two porous concrete layers that fulfills each optimization criterion for different average superficial velocities. Solid line: Crit. 1 is fulfilled, dashed line: Crit. 2 is fulfilled.

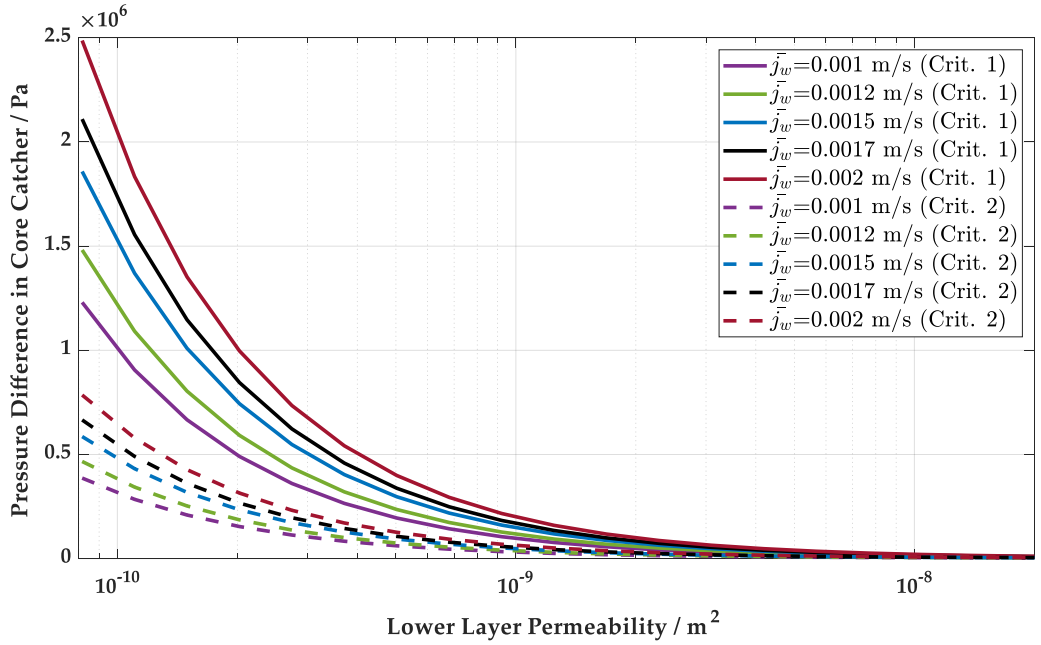

Figure 3.12 Change in pressure difference in the core catcher in relation to lower layer permeability when the upper layer permeability fulfills each optimization criterion

for different average superficial velocities. Solid line: Crit. 1 is fulfilled, dashed line: Crit. 2 is fulfilled.

Figure 3.11 shows that the permeability values of upper and lower layer have the same ratio to fulfill each optimization criterion with different uniformity independent of the total mass flow rate of the cooling water and aimed average superficial velocity. Based on this, it can be concluded that for the same concrete pairing the distribution ratio of the cooling water along the concrete corium contact surface stays the same for different cooling water flow rates. In other words, the decided uniformity is not be affected by the total flow rate.

On the other hand, as expected, Figure 3.12 shows that the increased total coolant flow rate, hence the average superficial velocity, increases the total pressure difference in core catcher for the same core catcher. Which results in increased input pressure values.

3.5.2 Optimization of Systems with Different Height Ratio of Concrete Layers

The optimization simulations are performed for 3 different height ratios of the concrete layers, see Table 3.8, for the same mass flow rate of cooling water ($\dot{m}_w = 42.23\ kg/s$, $j_w = 0.0015\ m/s$).

Figure 3.13 shows the relation between the permeability of lower concrete layer and the permeability of upper concrete layer for 3 different cases of concrete layer heights. Figure 3.14 shows the resulting pressure difference in core catcher in relation to lower layer permeability for these cases (the upper layer permeability is paired as seen in Figure 3.13). In both Figure 3.13 and Figure 3.14, the solid line is the relation between the two parameters where each average superficial velocity is reached while realizing the optimization criterion 1 (Crit. 1) and the dashed line represents the relation between the two parameters where each average superficial velocity is reached while realizing the optimization criterion 2 (Crit. 2).

As seen in Figure 3.13, for this constant total height of the core catcher, the permeability of the upper layer is the highest for the same water distribution when the layer thicknesses are equal. On the other hand, in Figure 3.14, the pressure difference in the core catcher increases with increasing ratio of the upper concrete layer thickness. This is expected since the upper concrete layer always has lower permeability than the lower concrete layer, hence the pressure loss in upper layer is higher. Although, for the same uniformity of superficial velocity, the upper layer permeability values for 8 cm high upper layer and 24 cm high upper layer are the same and both lower than the 16 cm upper layer case, the pressure difference in the total system are increasing based on their ratio. This is based on the fact that both the permeability and the height of a porous concrete has an influence on the pressure drop along the total height of it. As Figure 3.14 shows, the pressure values are increasing for higher ratios of upper layer but not proportionally to the height, because it is compensated by the permeability values for upper layer shown

in Figure 3.13. Another detail from the figure is that the values for total pressure difference in core catcher observed for two different thickness ratios almost overlap. Each case has also different upper layer permeability values and they deliver the cooling water with different uniformity. This overlap demonstrates how different parameter combination would realize the same boundary condition depending on the desired outcome.

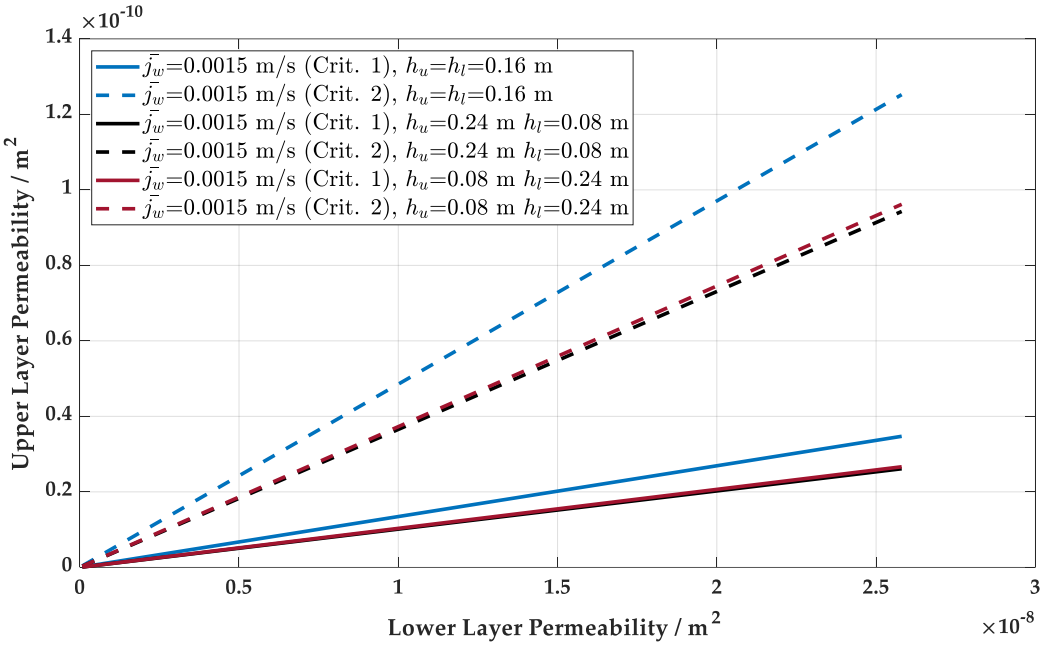

Figure 3.13 Relation between permeability values of two porous concrete layers that fulfills each optimization criterion for different layer height ratios. Solid line: Crit. 1 is fulfilled, dashed line: Crit. 2 is fulfilled.

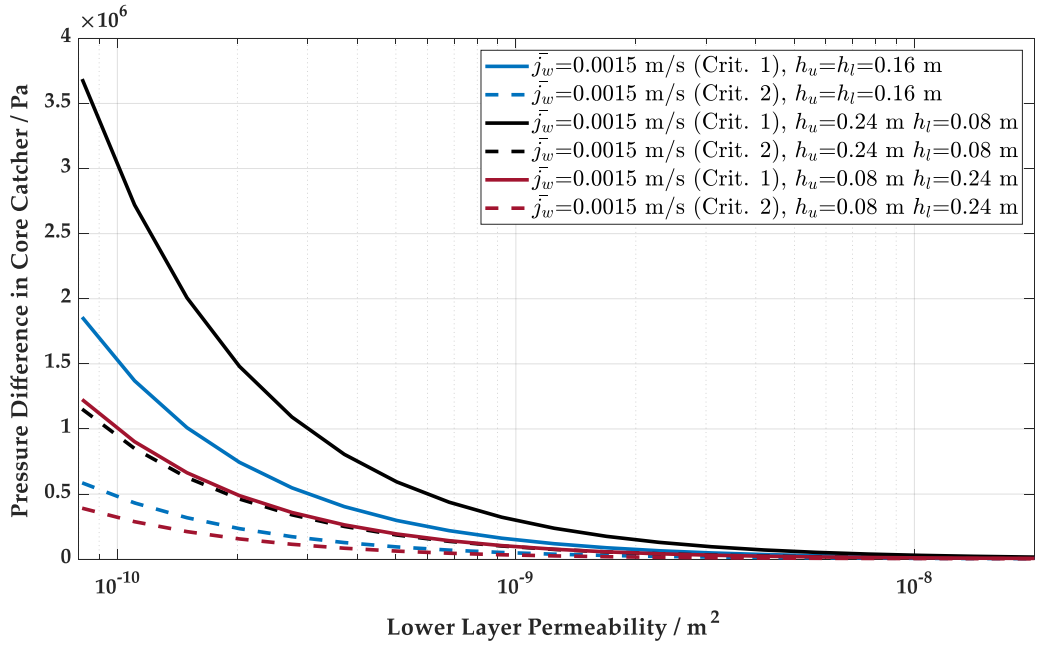

Figure 3.14 Change in pressure difference in the core catcher in relation to lower layer permeability when the upper layer permeability fulfills each optimization criterion for different average superficial velocities. Solid line: Crit. 1 is fulfilled, dashed line: Crit. 2 is fulfilled.

A comprehensive comparison of the change in total pressure difference in the core catcher system in relation to lower layer permeability for the various mass flow rate and concrete thickness values from this section is presented in Appendix A Figure A.7.

The optimization methodology presented in this section can be applied independently of the boundary conditions. Through this optimization possible combinations for hydraulic parameters can be determined for a desired outcome or allowed boundary conditions, and the design decisions can be made with the help of the outcome of the optimization.

3.6 Cooling Water Inlet Configuration for Back Fitting

The simulations in this chapter so far are performed for the ideal case of cooling water being provided around the core catcher circumference. For a possible back fitting application of the porous concrete core catcher device, the connection with the cooling water supply is expected to be restricted. A single point opening, as can be seen in Figure 3.2, is a more suitable option under the restrictions of back fitting.

In order to investigate this restricted case, the cooling water flow distribution in core catcher device is simulated for the case where the water is supplied to device through single opening point. This opening is assumed to be at the base of the side with 0.03 m height and 6° opening on the circumference, yielding to 0.0094 m^2 surface area. Compared to the circumferential water inlet cases, this inlet area yields higher mass flux and higher superficial velocities at the inlet of porous concrete and nearby. For instance, 42.23 kg/s mass flow rate supplied to the system for the design aim of 0.0015 m/s rising superficial velocity means mass flux as high as 4480.05 kg/m^2s and superficial velocities as high as 3.08 m/s at the water feed region of the porous concrete device. The same mass flow rate of cooling water yields to 74.67 kg/m^2s mass flux and 0.075 m/s superficial velocity at the inlet region for the case of circumferential inlet. This difference in flow velocity is expected to have an effect on the friction forces within the porous concrete layers.

For the velocities reached in the single inlet case, it is expected that the friction law for flow would not be linear anymore. The quadratic dependency of the pressure difference via passability as seen in Equation (2.7) would be a more suitable model. In the literature, the porous concrete research is limited to lower or creeping water flow velocities that bring a linear correlation between pressure losses and velocities. With the lack of information in existing literature for high velocity flow through porous concrete, the initial simulation for the single inlet case is performed with linear dependency between pressure losses and superficial velocity. Passability is assumed sufficiently high in the applied momentum models in COCOMO3D and the permeability values of the upper and lower layer were taken as 1.96×10^{-12} m^2 and 1.46×10^{-9} m^2 respectively as the reference case in Chapter 3.4.2.

The other input parameters of the simulation were taken the same as the reference case as well (see Table 3.4) and COCOMO3D simulation was applied with the boundary conditions as previously. Figure 3.15 shows the pressure values in the porous concrete device as a result of this simulation. The top view of water inlet configuration is given on the left top corner as a guidance and the actual water inlet is indicated on the figure as well. The entire device with a realistic scale with the mesh lines of each direction can be seen on the figure. In order to reduce the computation time, the meshes on cylindrical coordinates were taken finer on the water inlet region and coarser in the regions sufficiently away from the water inlet.

The simulation result yields to a total pressure difference of 280 kPa. For the given boundary conditions at the outlet, this would require a cooling water inlet with pressure value of 403 kPa, which is rather high. For the same input parameters and boundary conditions, the circumferential water inlet case yields to 104.22 kPa of total pressure difference in the core catcher and 235 kPa inlet pressure. The inlet pressure has almost doubled. Moreover, it is still underestimated due to use of linear correlation for friction law.

Figure 3.16 shows the resulting visible superficial velocities to have a better understanding and comparison of superficial velocities reached at inlet and outlet. The visible superficial velocity is calculated as follows:

$$j_{vi} = \sqrt{{j_x}^2 + {j_z}^2} \tag{3.1}$$

where j_x is the superficial velocity in radial direction and j_z is the superficial velocity in axial direction.

The legend of the Figure 3.16 was adjusted to show the velocity distribution on the surface in a better way, the maximum superficial velocity that was reached at the inlet can be still seen on the legend. On the surface of the porous concrete system, the superficial water velocities reach up to 0.0035 m/s near perimeter where the water inlet connection is and decreases to 0.001 m/s at the farthest regions. However, as the total pressure drop along the porous concrete layers are underestimated due to the applied linear friction law, these superficial velocities are expected to be lower in reality.

The hydraulic properties of porous concrete layers become more important in back fitting case for existing reactor due to higher velocities in the inlet and limited inlet connections. Appropriate friction laws should be applied to simulate the distribution of the cooling water along the cavity. Underestimating the friction losses along the porous concrete could lead to insufficient cooling water supply in the application.

In order to model the flow through porous concrete core catcher system more realistically, the relation between the pressure loss and cooling water velocity for the flow through a prototypical porous concrete should be measured. For better understanding of the cooling mechanism of a porous concrete core catcher, the next chapter of this work investigates the actual friction laws for porous concrete types that have been used in CometPC research.

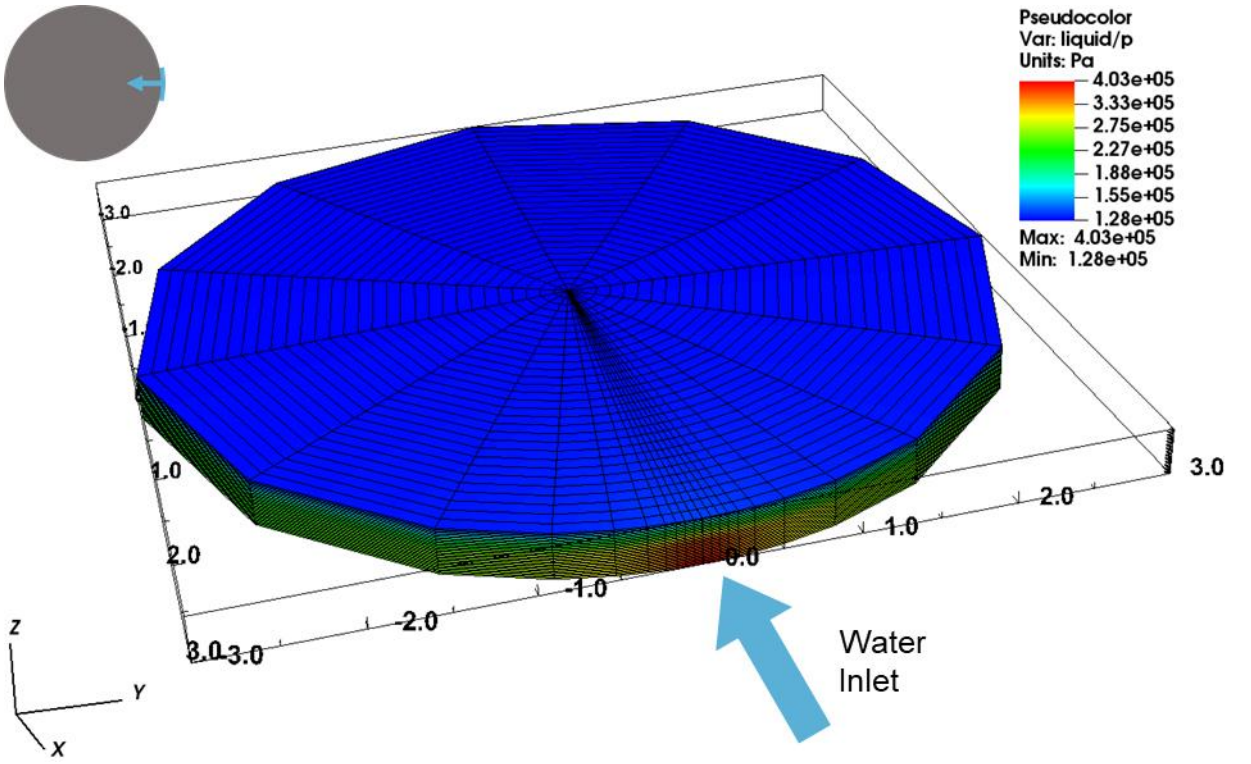

Figure 3.15 Pressure values as a result of the simulation of cooling water flow with single point inlet. Water inlet point and top view of inlet configuration are given on the figure.

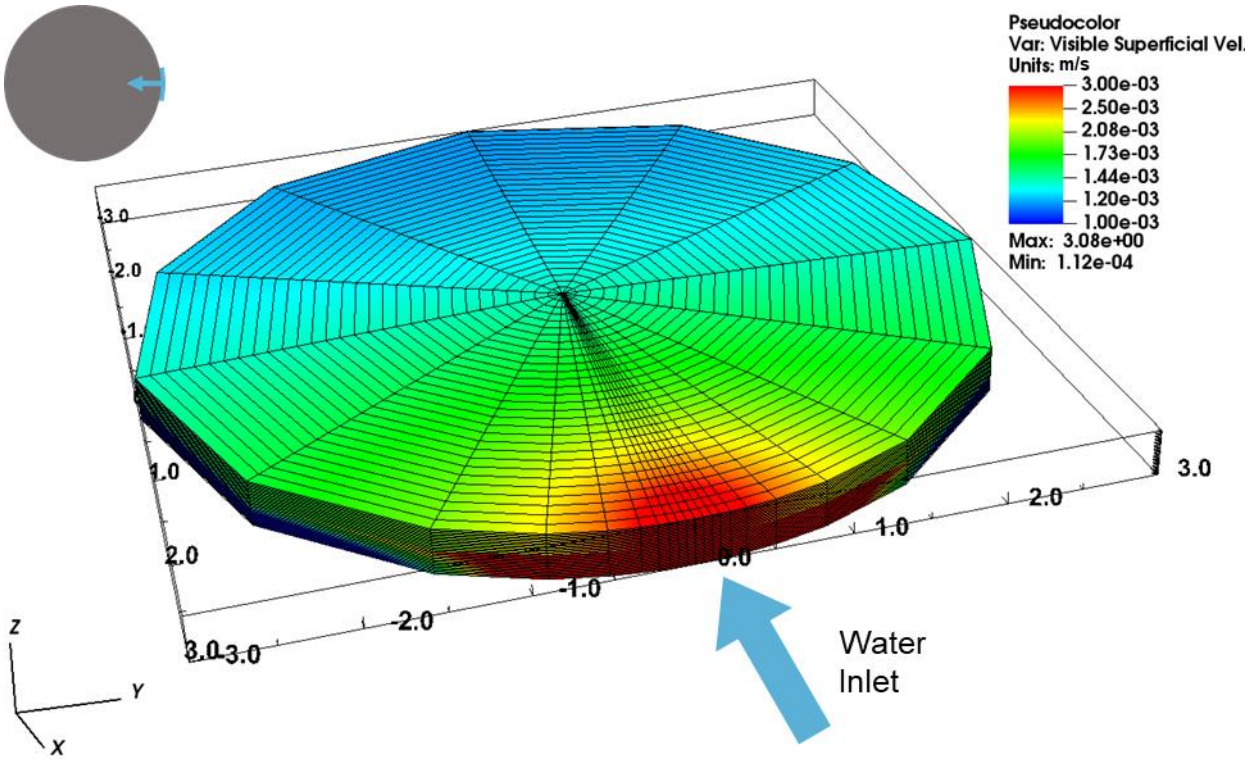

Figure 3.16 Visible Superficial Velocity in the Core Catcher as a result of the simulation of cooling water flow with single point inlet. Water inlet point and top view of inlet configuration are given on the figure.

4 Experimental and Numerical Investigation of Hydraulics of Prototypical Porous Concrete

For the reactor application of a porous concrete core catcher, depending on the water inlet configuration, high velocities of the cooling water are to be expected due to high volume flow rates through small areas at cooling water inlet points. This high volume flow rate evolves into slow creep flow close to the porous concrete-melt layer contact surface. The investigations presented in Chapter 3 indicate that the results are sensitive to the friction laws applied in the simulations, i.e. the relation between velocity and pressure drop in a porous concrete. The Darcy and Ergun laws that are presently applied in the COCOMO3D code are determining the permeability and passability of simulated porous media based on their porosity and aggregate size. These empirical models are adequate for the simulation of particulate debris, but their application to porous concrete is questionable. Moreover, due to their structure, which is mix of cement and various aggregate sizes and shapes, it is difficult to define the effective porosity size in a porous concrete that is required for the application of these models. Porous concrete types from the existing literature on the other hand, are presented with only linear friction law, which is not suitable for the rapid flow regions that can occur in the core catcher application case. In order to model the flow through this type of core catcher system more realistically, the relation between the pressure loss and cooling water velocity for the flow through a prototypical porous concrete should be measured.

This chapter presents the experiments performed on the porous concretes that have been used in the previous CometPC experiments at KIT in order to determine their permeability and passability. An experiment set-up is built at IKE for this work to measure the pressure loss along the porous concrete samples for various water velocities. Following the experimental investigation, the obtained friction laws are implemented in COCOMO3D and water flow simulations through porous core catcher with obtained friction laws are performed. Finally, a CometPC experiment, which uses the same concretes as the core catcher is partially simulated to have an insight into the pressure losses in the system.

4.1 Measurement of the Hydraulic Properties of Prototypical Porous Concretes

4.1.1 Samples

Porous concrete samples that are similar to the ones that have been used for previous CometPC experiments were prepared and provided by KIT. The 4 samples in cylindrical geometry are seen in Figure 4.1. Two of them have the same properties to the concrete type that was used as bottom layer during CometPC experiments (coarse concretes C1 and C2) while the other two have the properties of the concrete type that was used as top layer (fine concretes F1 and F2).

Figure 4.1 Porous concrete samples from KIT. Samples left to right: C1, C2, F1, and F2.

A few of the properties such as size and the porosity of these concretes can be seen in Table 4.1. Information on the porosity of the samples and aggregate diameters for each type of concrete were provided by KIT.

Table 4.1 Properties of concrete samples that were used in measurements.

	Sample C1	Sample C2	Sample F1	Sample F2
Aggregate diameter, D_p [mm]	8-16	8-16	2-8	2-8
Porosity, ε [-]	0.30	0.30	0.15	0.15
Sample length, h [m]	0.16	0.15	0.15	0.15
Sample diameter, d [m]	0.152	0.152	0.152	0.152

For permeability or pressure loss measurement for an unfixed packed bed of aggregates, the edge effect, where the fluid bypasses the bed is an issue that needs to be taken into consideration. However, as consolidated porous media, the porous concrete samples are prepared with aggregate and cement mixture that provides a fixed continuum structure to the inner wall of the cylinder that the sample is prepared in. Although this prevents a complete by-pass of the flow, the openings at the wall and sample interface might show

structural differences from the sample itself, which might influence the pressure drop measured. Therefore, the diameter of these samples is chosen large enough to be able to neglect the edge effects [71] [72].

4.1.2 Measurement Method

In order to determine permeability and passability of a porous medium the pressure loss accompanying the flow of water through a porous medium should be measured. One possible method is to provide water flow vertically through porous medium under various imposed hydrostatic pressures. Usually, the height of the water column above the sample is kept constant and the flow is determined by measuring the mass of water that has drained and accumulated within a certain time interval [37] [63] [64] [73]. For this so-called constant head method, a certain constant water head above the sample must be maintained during the continuous flow through the sample. Therefore, this method is more favorable for small samples or for the low permeable samples.

An alternative to this method, which can also carry more challenges to the measurement, is the so-called falling head method. This method relies on continuously descending water head as an energy input [37] [64] [66] [73] [74] [75] [76] [77]. Since two of the samples to be measured in this work have relatively high porosities and turbulent flow is expected, it was concluded that to achieve constant hydrostatic head of water would require water volume flow rates that are too high to achieve under our laboratory conditions. In its primitive form, the falling head test consists of reading the change in water column height above the porous sample by time. This simple application would be highly limited to the low drainage samples. However, there are successful applications of this method for expected turbulent flow cases by using suitable measurement and data acquisition [66] [76] [77]. Based on this, a modified falling head method is applied for the measurements in this work. Although the method is more challenging for data acquisition, it is better suitable for high porous concrete samples to perform measurements in wide parameter range.

Figure 4.2 schematically shows the measurement principle of the falling head method used in this work. In a vertical setting, the concrete sample is placed in the column in a way to prevent leakage through the perimeter. The water column is filled up to a desired height above the porous concrete, z_w, while a gate valve is kept closed below the concrete sample to prevent water flowing through, as shown in the left side of the figure. When the porous concrete sample is saturated with water, water flow through the porous concrete is set free by opening the gate valve below the concrete and the water level above the concrete decreases by the time. The right side of the figure demonstrates the flow position at a time t after opening the gate with remaining water column height of $z_w(t)$. In Figure 4.2, point 0 marks the water column surface, point 1 marks right above the concrete sample placed in column, and point 2 marks right below the surface. For a sample height of h, the distance between point 1 and 2 is also h.

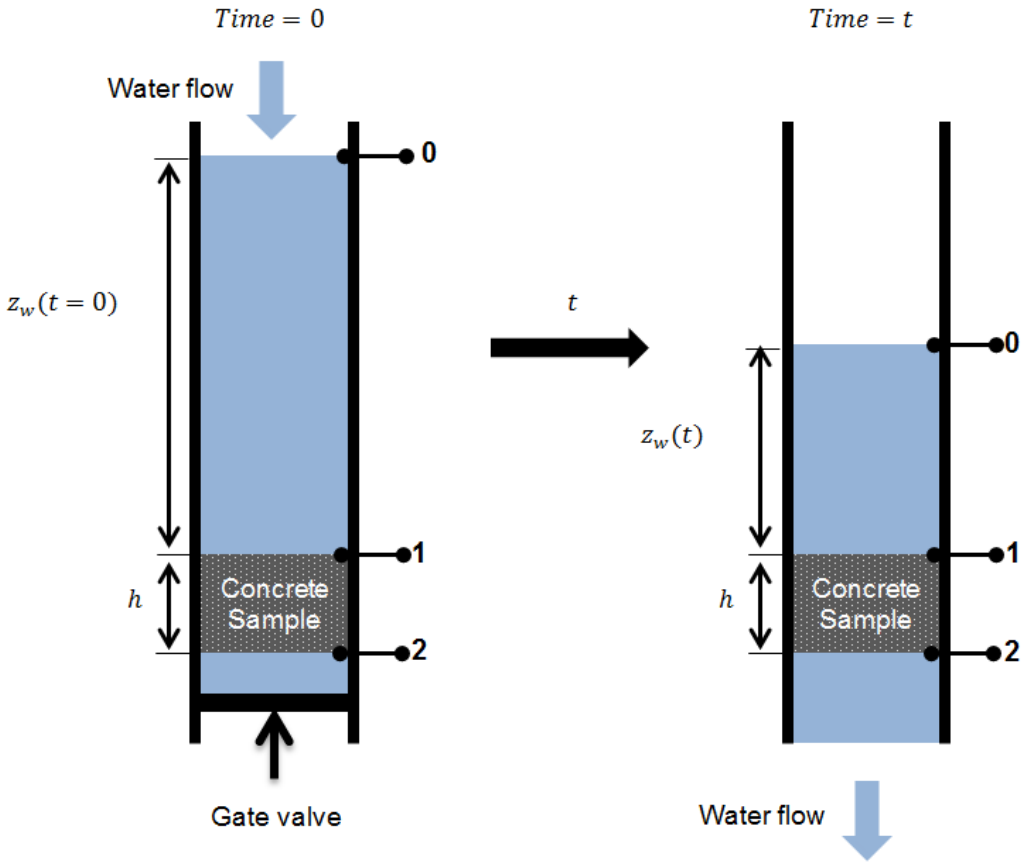

Figure 4.2 Measurement principle of the falling head method shown schematically. Left side: Filling up the water column that the porous sample is positioned in, until the sample is saturated. Right side: Flow of the water through porous sample at a certain time t after opening the gate.

For evaluating the flow behavior, the energy balance of the system can be solved by applying the Bernoulli Equation for a flow on a streamline. For unsteady frictionless flow along a vertical streamline in z direction Bernoulli Equation is defined as follows [78]:

$$\rho \frac{\partial v}{\partial t} dz + dp + \rho v \, dv + \rho g \, dz = 0 \tag{4.1}$$

where ρ is the liquid density, v is the discharge velocity, z is the elevation, p is the static pressure, g is the gravity acceleration. When there are friction losses in the system, this equation can be used to balance the forces due to friction losses in the streamline. The differential form from the Equation (4.1) can be integrated between any two points a and b along the streamline for incompressible flow with friction losses as follows:

$$\int_a^b \rho \frac{\partial v}{\partial t} dz + (p_b - p_a) + \frac{1}{2}\rho({v_b}^2 - {v_a}^2) + \rho g(z_b - z_a) = \int_a^b f_f dz \tag{4.2}$$

where f_f is the pressure loss per unit length due to friction. Therefore, the right hand side of the equation stands for energy loss of the system due to friction. Equation (4.2) can be applied to flow through the porous concrete and flow through the section above the porous concrete separately.

For the flow between points 0 and 1 in the Figure 4.2, the friction losses can be neglected for straight and wide pipe geometry compared to the porous concrete. For a wide enough vertically straight, column-like flow path, after a short initial acceleration phase a quasi-steady flow should be established. Hence, the first term of Equation (4.2), which is the transient term for temporal change of momentum between points a and b, can be neglected for such a system. Since the straight pipe has a constant cross section, the velocity is the same at points 0 and 1 and the terms representing the kinetic energy are cancelled out. As a result, the Equation (4.2) can be rewritten for a quasi-steady frictionless flow between points 0 and 1 as follows:

$$(p_1 - p_0) + \rho g(z_1 - z_0) = 0 \tag{4.3}$$

The pressure value at point 0 that is on the water surface can be assumed to be equal to the atmospheric pressure in laboratory conditions. By measuring the pressure value at point 1, the height of the water column above the concrete sample, z_w, at any given time t can be determined as follows:

$$z_w(t) = \frac{p_1(t) - p_0}{\rho g} \tag{4.4}$$

Following this, the water discharge velocity (superficial velocity) of the water can be calculated from the time derivative of $z_w(t)$ as follows:

$$\frac{dz_w(t)}{dt} = v(t) \tag{4.5}$$

Between points 1 and 2 in Figure 4.2, the flow path leads through the porous concrete. Hence, the pressure losses due to friction through porous concrete are important for the energy balance between these two points of flow. It can be assumed that the superficial velocity and the surface areas (flow path cross-section) above and below the porous concrete sample are equal therefore a quasi-steady state would be again established. As a result, the Equation (4.2) can be rewritten for flow between points 1 and 2 as follows:

$$(p_2 - p_1) + \rho g(z_2 - z_1) = -\int_1^2 f_f dz \tag{4.6}$$

The average friction properties of the concrete sample are of interest for this work and this value can be interpreted as constant. As the difference in elevation between points 1 and 2 is denoted by the sample height, the Equation (4.6) becomes as follows:

$$(p_2 - p_1) - \rho g h = -f_f h = -\Delta p_f \tag{4.7}$$

Which essentially shows that the friction losses in the porous concrete are balanced by the pressure difference along the porous concrete.

As the pressure value at point 0 is assumed to be atmospheric pressure, by determining the pressure values at points 1 and 2 the instantaneous superficial velocity and corresponding pressure losses due to friction in the sample based on the flow equations above. This allows to gain the information on the functional dependency of pressure loss on velocity for a high range of velocity values. The upper limit of the velocity range will be determined by the initial water column height and the lower limit would approach to zero.

A modified falling head measurement set-up was built at IKE laboratory within this work that satisfies the established methodology [79].

4.1.3 Measurement Set-Up

The measurement set-up should be able to provide the required data and satisfy the assumptions for the balance equations that are presented in Chapter 4.1.2. KIT manufactured the porous concrete samples inside a standard 160 mm PVC pipe, according to desired dimensions, see Figure 4.1. In order to keep this wide diameter constant in the whole system, the measurement set-up is also constructed from standard 160 mm PVC pipes and fittings [79].

Figure 4.3 shows the measurement set-up. The total height of the system adds up to approximately 6.5 meters, which yields the maximum height of 5.10 meter of water column above the concrete samples. The bottom section of the test set-up is composed of the same type of PVC pipes including a gate valve which closes the system during the water fill-up and test preparation. The gate also allows very sudden and complete opening of the pipe to minimize the initiation effect on the measurements. Concrete samples are stabilized in the pipe leak tight with a collar piece from the same PVC material.

Figure 4.3 Measurement set-up in IKE laboratory for the modified falling head method. Left: The lower part of the set-up with instrumentation, sample placement area and opening valve. Right: View from below to the entire height of the set-up.

Figure 4.4 provides a more detailed look into the placement of pressure transducers and sample placement. The figure shows the CAD drawing of the lower part of the measurement setting. Pressure measurement is provided by two pressure transducers connected to a data acquisition system, see Figure 4.4. The first pressure transducer, the PR-23 type relative pressure transducer from Keller Company, is positioned right above the porous concrete sample in order to follow the hydrostatic pressure of the water column above. The zero point of the pressure transducer is set to the room pressure by manufacturer, so it can read directly the relative pressure of the water column during measurements. The second pressure transducer, PD-33X type differential pressure transducer from Keller Company, is connected to right above and below of the concrete sample. With this pressure transducer, the static pressure difference between these two points is acquired. In order to read positive data during the test, the positive side of the transducer is connected above the sample and the negative side of the transducer is connected below the sample. These connection points are kept close to the sample for more accurate measurements of the pressure losses due to friction forces inside the porous concrete. The precision and the offset of these pressure transducers are discussed in the Appendix B within the measurement error discussion.

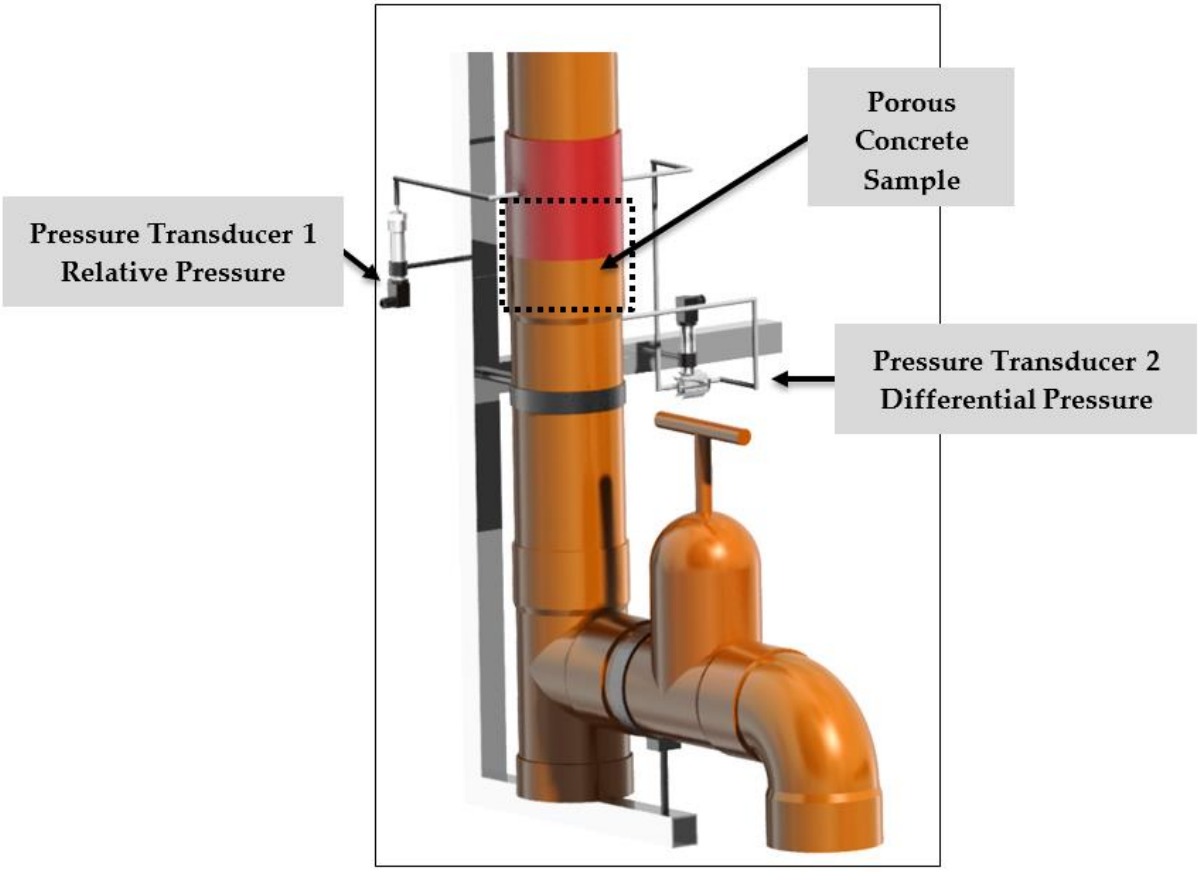

Figure 4.4 CAD drawing of the measurement set up with detailed view of instrumentation and sample placement [79].

Before the measurements, the entire system is filled with water while the gate valve below is in closed position. At the filled state, a sufficient time is given for porosities to saturate with water. The measurement is initiated before the opening of the gate and continues until the system is empty. During the measurements, both pressure transducers acquire data with 2 Hz frequency. Although the measurement times are relatively short, especially for the concretes C1 and C2, sufficient data points for the data evaluation are obtained with this measurement frequency.

4.2 Measurement Results and Discussion

The measurements are repeated 11 times for samples F1 and F2, and 10 times for samples C1 and C2 in order to assure the reproducibility of the method. The data from both pressure transducers are acquired simultaneously. Figure 4.5 shows the measured pressure values during the test by two pressure transducers, for each sample. The first diagram, Figure 4.5.a, shows the measured relative pressure right above the porous concrete sample by the relative pressure transducer. The second diagram, Figure 4.5.b, shows the measured pressure difference between top and bottom of the porous concrete sample by the differential pressure transducer.

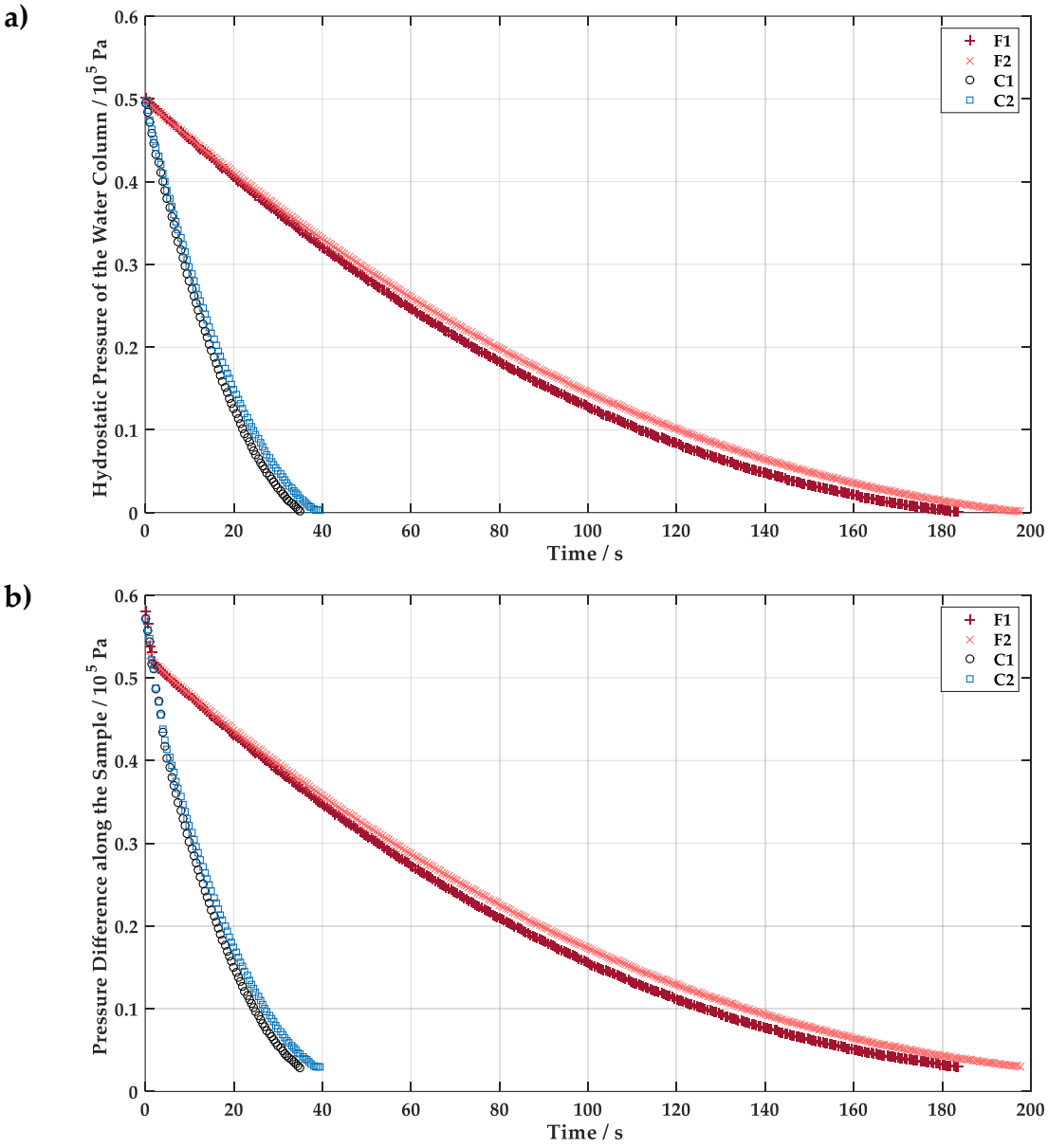

Figure 4.5 Measured pressure values during the test. a) Pressure values from the relative pressure transducer that represents the change in hydrostatic pressure difference of the water column above the sample. b) Pressure values from differential pressure transducer that represents the pressure difference along the porous concrete sample.

The measurement values shown in the Figure 4.5 belong to the measurement that has approximately the mean value of the repeated measurements for each sample. The measurement uncertainties are presented in Appendix B. Although the falling head measurement method is the most suitable for these samples, the data analysis with such transient measurements is challenging and the acquired data should be handled with great care. Pinpointing the begin and end time is the first important step. Since the nature of the experiment requires a sudden opening of the water filled system and a continuous measurement. Hence, the data acquisition is initiated already in the filled state of the system,

before the opening of the gate. During the data processing, the time point where the differential pressure transducer measures the highest pressure is assumed as the time where the gate valve is opened completely. This time point is assumed as the beginning time of the measurements which is shown as the initial time (t=0 s) on both diagrams in Figure 4.5. This continuous measurement continues until after the system is completely empty. After the water level decreases below the connection points of the pressure transducers there is a certain fluctuation above absolute zero measured by relative pressure transducer, that has no effect on the measurements when the water level is still above this connection. A few seconds before this point is reached, is assumed as the end time of the test. The initial time and end time of the test is taken in the same way for all samples. As it can be seen on the Figure 4.5, for the same amount of water that flows through the concrete sample, it takes longer for the finer samples F1 and F2.

Having established the beginning and end time of the measurement, a reproducibility analysis was performed based on pressure difference acquired by each pressure transmitter between certain time frame of the measurement. This reproducibility analysis is presented in detail in Appendix B as a part of measurement uncertainties. As it is discussed in Appendix B, it is analyzed thoroughly that these measurement results are systematically reproduced for each sample among the repeated measurements with a small uncertainty margin. Thus, the observed differences in Figure 4.5 in the measurements between nominally identical samples come from variations in their hydraulic properties. These differences are not completely unexpected, since the fabrication process of a porous concrete inherently involves a certain degree of randomness. In this sense, the differences between the samples give some indication of the variations to be expected for the local hydraulic properties within the concrete layers.

For the evaluation of the measured data in use of friction model, the first few seconds of the actual experiment are excluded in order to avoid the fluctuations due to sudden gate opening at the beginning of the water flow and be more consistent with the quasi steady-state assumption. The pressure values measured by relative pressure measurement are used in Equation (4.4) to convert them into water column height above the porous concrete sample as seen in Figure 4.6.

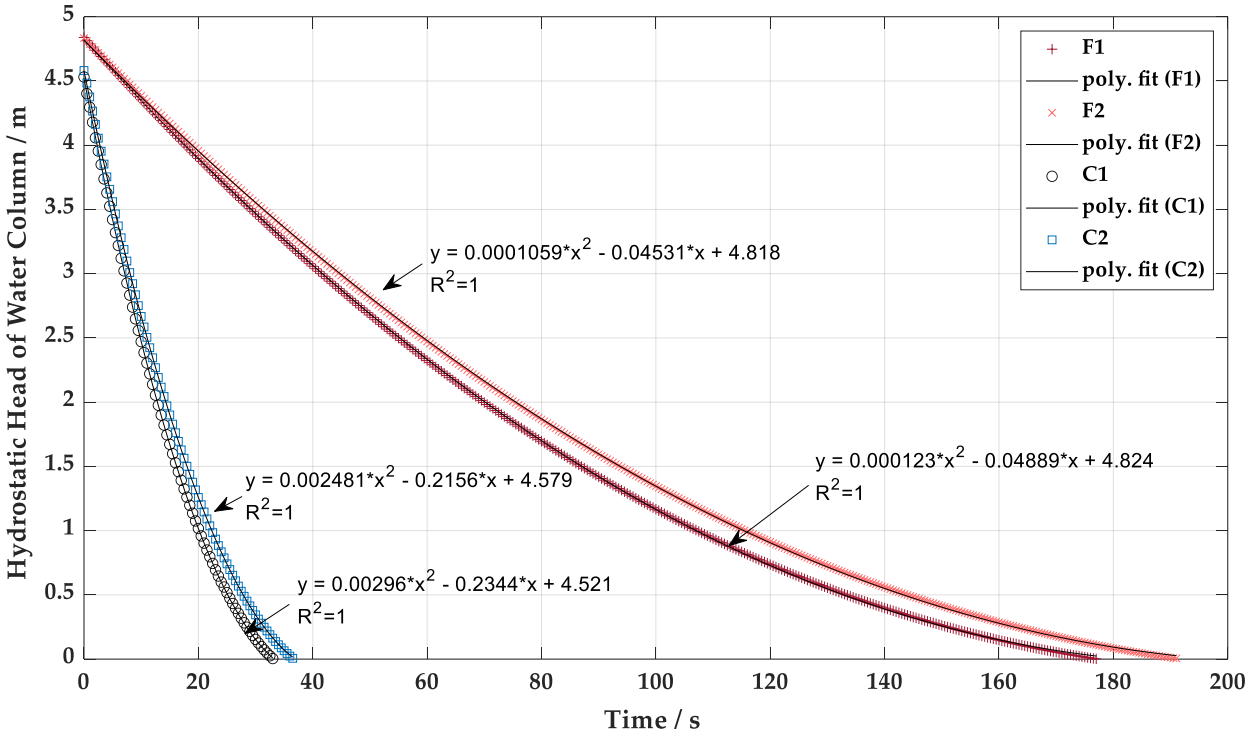

Figure 4.6 Change in the height of the water column above each sample by time. The equation for the polynomial fit for each data curve are shown.

Figure 4.6 shows the hydrostatic head of water column $z_w(t)$ at measurement times for each sample. The data set for each sample is fit with second-degree polynomial curve with the format seen in Equation (4.8).

$$z_w(t) = c_1 t^2 + c_2 t + c_3 \tag{4.8}$$

The coefficients c_1, c_2 and c_3 for polynomic fit to measurements for each sample can be seen in Table 4.2.

Table 4.2 Coefficients for polynomic fit to change in the height of the water column above each sample by time.

	c_1	c_2	c_3
poly. fit(F1)	0.000123	-0.04889	4.824
poly. fit(F2)	0.0001059	-0.04531	4.818
poly. fit(C1)	0.00296	-0.2344	4.521
poly. fit(C2)	0.002481	-0.2156	4.579

The second-degree polynomial equation for each data set is differentiated in Equation (4.5) in order to determine the discharge velocity (superficial velocity) by the change in the water column height. In principle, an alternative to this approach would have been computing divided differences for each data point. Instead, an approach based on fitting the data to an analytic function is pursued as mentioned with second order polynomial providing a highly satisfactory fit for each sample. Differentiating the polynomial equations with respect to time yields the superficial velocity of the water as functions of time for each sample.

The static pressure difference values measured by differential pressure transducer are used in Equation (4.7) in order to calculate the pressure difference along the porous concrete sample due to only friction losses. The pressure difference due to friction losses for each sample is divided by their respective height in order to obtain the pressure gradient for each sample. Figure 4.7 shows the pressure gradient due to friction for each sample plotted with corresponding superficial velocity values determined earlier.

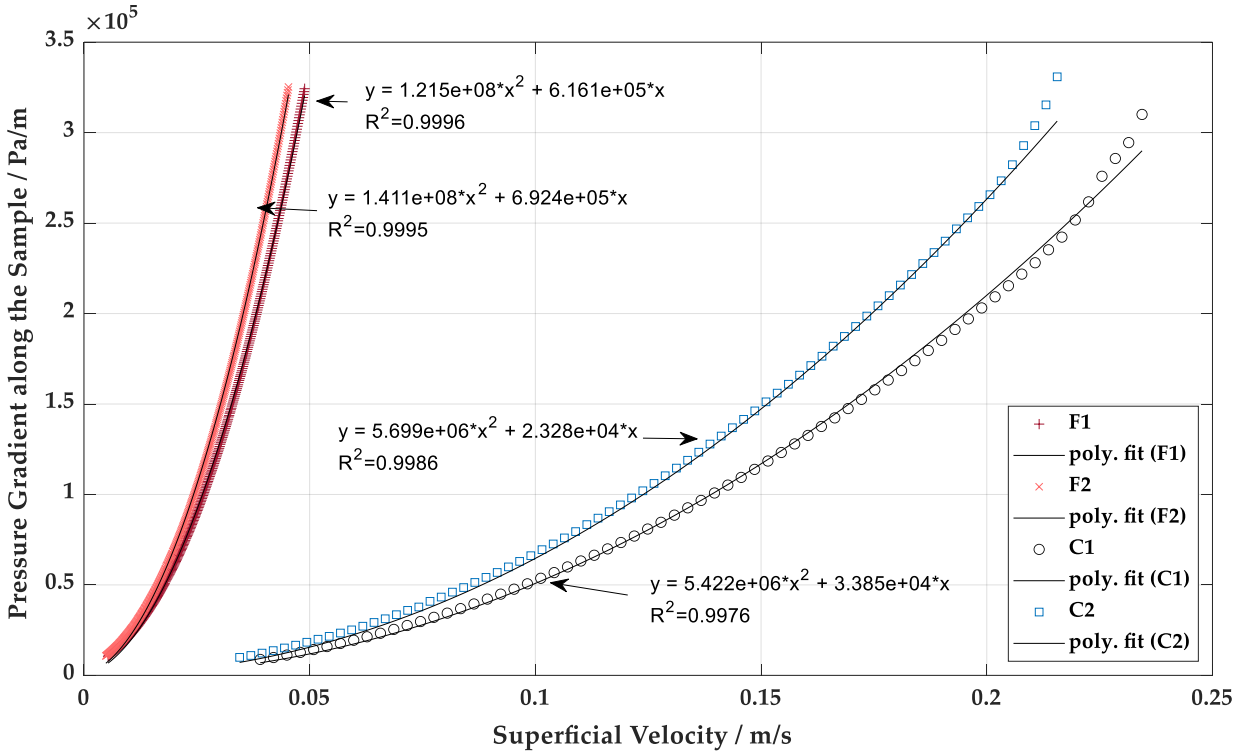

Figure 4.7 Pressure gradient along the sample due to friction by change in superficial velocity for each porous concrete sample.

The relation between the superficial velocity and pressure gradient due to fiction provides the information about the friction law of the porous concrete sample. After trying few other fit to the seen trends, a second-degree polynomial fit provided the best fit into the data. As a physical definition, pressure gradient due to friction in the sample should be zero when there is no flow. In order to follow this physical limit, the polynomial fit line is forced to go through the origin point, where the condition is realized. This second-degree polynomial relation fits to the form of friction law described in Equation (2.7). The coefficients from fit equations in Figure 4.7 are used to calculate the permeability

and passability of each sample. For these calculations, the water properties in the IKE laboratory are considered, that is at atmospheric pressure and approximately 10°C during the measurements with fine concretes F1 and F2, and approximately 8°C during the measurements with coarse concretes C1 and C2. Table 4.3 shows the measured permeability and passability values of the sample concretes.

Table 4.3 Permeability and passability values of the samples F1, F2, C1 and C2 based on the measurement results.

	Permeability [m^2]	Passability [m^{-1}]
Sample F1	$2.12x10^{-9}$ ($\pm 1.31x10^{-11}$)	$8.23x10^{-6}$ ($\pm 6.35x10^{-8}$)
Sample F2	$1.89x10^{-9}$ ($\pm 1.72x10^{-11}$)	$7.09x10^{-6}$ ($\pm 7.89x10^{-8}$)
Sample C1	$4.09x10^{-8}$ ($\pm 5.15x10^{-10}$)	$1.84x10^{-4}$ ($\pm 3.02x10^{-6}$)
Sample C2	$5.95x10^{-8}$ ($\pm 1.25x10^{-9}$)	$1.75x10^{-4}$ ($\pm 4.52x10^{-6}$)

As it is discussed previously in this work, for such permeable concrete samples it is best to perform measurements for determining the most reliable information on their hydraulic properties. For the sole purpose of comparing with the measured values, permeability and passability of these concrete samples were also predicted by Ergun's law which is a quadratic friction law for flow through porous media. Ergun's law predicts permeability and passability of porous media based on their porosity and effective particle diameter (Equations (2.8) (2.9)). These parameters are taken as provided by KIT, see Table 4.1. Due to lack of information about effective particle size, the average of the given particle diameter range is taken as effective particle diameter for each sample. Table 4.4 shows the permeability and passability of the concrete samples in comparison with the measured ones.

Table 4.4 Measured permeability and passability values of the samples F1, F2, C1 and C2 in comparison with estimated permeability and passability values by Ergun's Law.

	Measured Permeability [m^2]	Estimated Permeability [m^2]	Measured Passability [m^{-1}]	Estimated Passability [m^{-1}]
Sample F1	$2.12x10^{-9}$	$1.45x10^{-9}$	$8.23x10^{-6}$	$2.03x10^{-5}$
Sample F2	$1.89x10^{-9}$		$7.09x10^{-6}$	
Sample C1	$4.09x10^{-8}$	$5.29x10^{-8}$	$1.84x10^{-4}$	$2.64x10^{-4}$
Sample C2	$5.95x10^{-8}$		$1.75x10^{-4}$	

Compared to measurements, it can be seen on the table that Ergun's Law estimates the permeability and passability values of these concrete samples very close to the measurement results. However, there is a caveat to these results, which is that the effective particle size is merely an estimation based on the range of particle sizes that were provided. In conclusion, the estimation of permeability and passability based on the Ergun's Law delivered close results, however, might not be reliable for porous concrete material such as the ones used in this work due to the effective particle size determination.

Having measured the permeability and passability values of the porous concrete samples used in the previous CometPC research, it is possible to now investigate the applicability of these concretes (or any porous concrete) to reactor scale more realistically. Moreover, it will provide an insight for understanding the molten corium solidification behavior with such porous concrete systems based on the Comet PC experiment results. Both of these aspects will be investigated in the following sections of this chapter.

4.3 Application of the Measurement Results to Reactor Scale Simulations

CometPC experiments have demonstrated that the concretes analyzed in this chapter are performing well with respect to providing a sufficiently uniform and sufficient enough water flow to arrest and stabilize the corium on the (relatively small) experimental geometry scale with relatively low overpressure values. With respect to larger prototypical reactor scale, previous chapter of this work demonstrated that a certain relation between the permeabilities of the two concrete layers and over pressure of the system is necessary to achieve sufficient and uniform distribution of the water towards the melt layer. It was also demonstrated in previous chapter of this work that by the restricted cooling water injection, such as only one inlet point, the proper friction law for high velocity flow through porous concrete is also of a high importance in order to predict the required pressure values for the cooling water inlet. It is therefore highly interesting to predict the water flow distribution at the concrete-melt layer interface by means of simulations when concretes with properties like the F1, F2, C1 and C2 samples are employed.

In this section, the simulations of the cooling water flow through porous concrete core catcher for reactor geometry with the measured permeability and passability values and obtained friction law are presented. By the simulation of 5 different cases, the effect of quadratic law and realistic porous concrete properties in terms of its effect on cooling water distribution and total pressure drop in core catcher are discussed.

For these simulations, the new quadratic friction law was implemented to COCOMO3D code by defining permeability and passability values for concrete layers. The boundary conditions and the geometry of the simulation are taken the same as the reference case presented in Chapter 3.4. For all these simulations, the target superficial velocity for the cooling water for sufficient cooling is 1.5 $x10^{-3}$ m/s throughout the core catcher surface,

therefore the cooling water is provided with 42.23 kg/s mass flow rate at the inlet. For each simulation case the concrete pairing and the inlet configuration of the water are the aspects that are investigated.

4.3.1 Case 1

For the simulation Case 1 permeability and passability values that are determined by the measurement of the KIT concrete samples are applied to the core catcher. For upper layer the permeability and passability value of F1 concrete, and for lower layer the permeability value of the C1 concrete is taken, as the measurements for these samples have lower uncertainties, see Table 4.3. Water inlet configuration for this case is a single inlet with conditions described in Chapter 3.6.

Figure 4.8 shows the resulting superficial water velocity values on the core catcher surface in axial direction for this simulation case. The water inlet configuration is given on the upper left corner of the figure as a guidance and the position of water inlet is shown as well. The legend on the upper right corner shows the said superficial velocities. As it can be seen on the Figure 4.8, at a small region (red) right by the water inlet the cooling water reaches to surface with high superficial velocities up to $10x10^{-2}$ m/s. And approximately 2/3 of the surface receives less than $0.3\ x10^{-3}$ m/s which is much less than required cooling water velocity of $1.5\ x10^{-3}$ m/s.

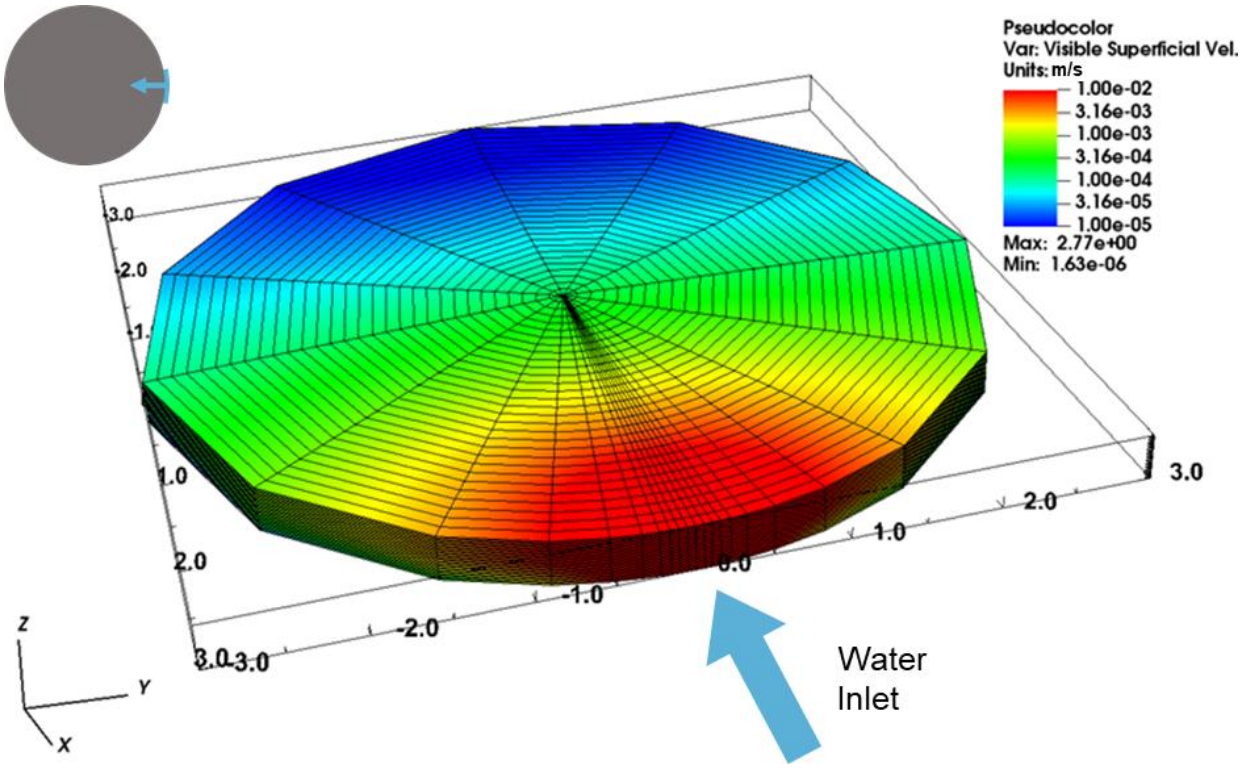

Figure 4.8 Superficial velocity values of cooling water in axial direction for simulation Case 1 (single inlet configuration with KIT concretes applied) Legend of the simulation result is adapted to the values on the surface. Water inlet configuration shown in upper left corner and water inlet point is indicated.

In addition, this simulation case yields to total pressure difference of 415 kPa which is relatively high for reactor application. Depending on the desired pressure value of water while exiting the core catcher, in order to overcome this pressure loss a water column height of over 40 m will be necessary. The structural stability of the core catcher is also another point which needs to be taken into consideration. And even with this high pressure, sufficient cooling water will not be distributed to the melt layer. Increasing the water flow rate would require even higher pressure values.

Based on the simulation Case 1 it can be stated that the concretes as they are used in CometPC experiments are not suitable for the single water inlet reactor application.

4.3.2 Case 2

For the simulation Case 2, the permeability and passability values are same as in Case 1 but the water inlet configuration is circumferential where the cooling water is provided to the core catcher from the sides all around, see Chapter 3.6.

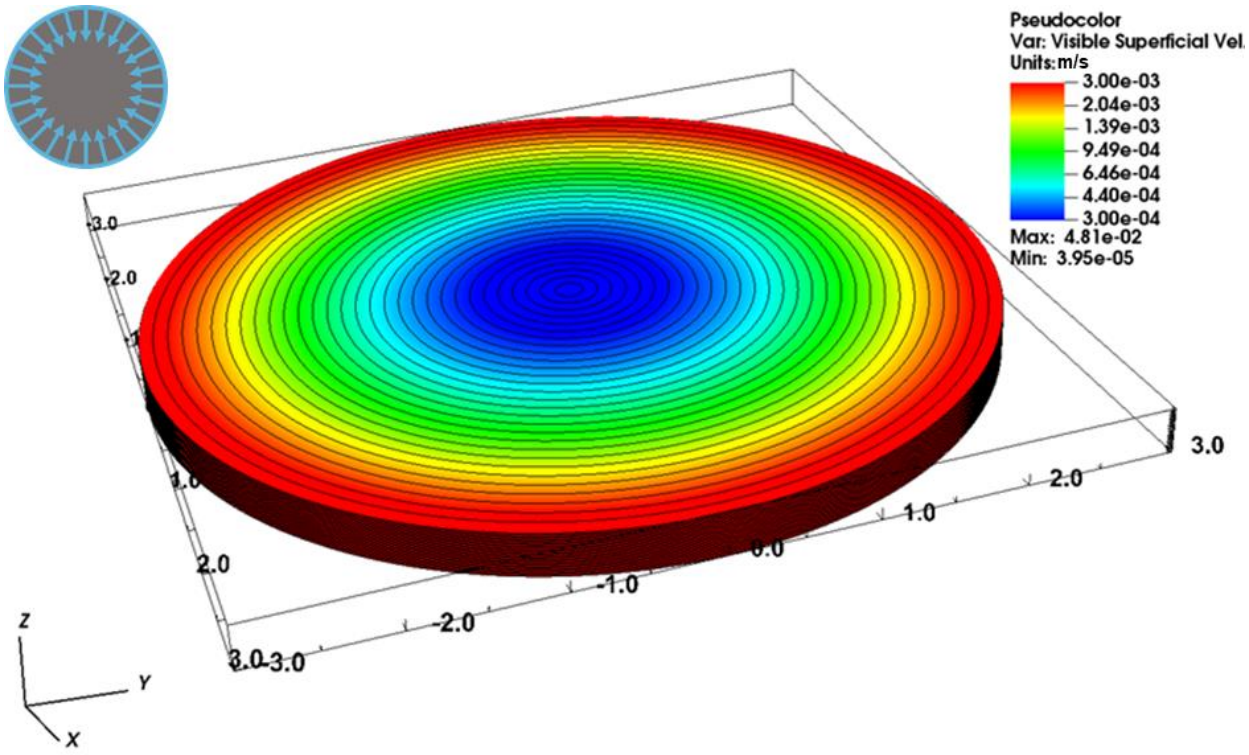

Figure 4.9 Superficial velocity values of cooling water in axial direction for simulation Case 2 (circumferential inlet configuration with KIT concretes applied). Legend of the simulation result is adapted to the values on the surface. Water inlet configuration shown in upper left corner.

In terms of providing water uniformly along the cavity, the circumferential water inlet configuration can be defined as more ideal compared to single water inlet. However, as Figure 4.9 shows, while a limited side region receives water with 3 mm/ superficial velocity, a large region in the middle of the core catcher (green, light blue, blue) receives

superficial velocity values less than required 1.5 $x10^{-3}$ m/s. Although the water distribution is improved compared to Case 1 it is still not sufficient.

The total pressure difference in the core catcher for this case is 3 kPa. Although this pressure value allows for total coolant mass flow rate to be increased, in order for middle section to receive sufficient cooling water, this increase will end up requiring very high inlet pressure and the side region will receive much more cooling water than required.

Based on the Simulation Case 2 it can be stated that the porous concrete core catcher used in CometPC experiments has its limitation for the reactor application. Even with the water inlet all around the core catcher the cooling water will be provided to corium in a very non-uniform way which is not optimal considering the pressure loads.

4.3.3 Case 3

For the simulation Case 3 the permeability values of the concretes from the reference case in Chapter 3 are taken, and passability values for these concretes are estimated based on the relation between permeability and passability in measured concrete samples. It must be stated here that, as mentioned earlier in this chapter, permeability and passability values of individual porous concretes should be determined by measurements. For the purpose of comparing the effects of linear friction law and quadratic friction law for the coolant flow in this work, it was assumed that the ratio of the permeability of a concrete to its passability is constant. The concrete samples F1 and C1 have these ratios between their permeability and passability, respectively: F1: $2.58x10^{-4}$, C1: $2.22x10^{-4}$. These ratios are close enough to continue with the constant ratio assumption for the fictitious concretes. For this work, a ratio of $2.58x10^{-4}$ permeability to passability was assumed for the fictitious concretes applied in simulations. According to this assumption the concrete pairing from the reference simulation case has the permeability and passability values as seen in Table 4.5. Water inlet configuration is taken as circumferential.

Table 4.5 Permeability and passability of the concrete layers from the optimized reference case when the quadratic friction law from the measurements applied.

	Permeability [m^2]	Passability [m^{-1}]
Upper layer	$1.96x10^{-12}$	$7.63x10^{-9}$
Lower layer	$1.46x10^{-9}$	$5.67x10^{-6}$

Figure 4.10 shows the superficial velocity of cooling water in axial direction on the core catcher surface. As it can be seen on the figure and the legend the superficial velocity of the cooling water towards melt layer in this case varies between 0.00135 m/s and 0.00165 m/s. This is the exact same variation of velocity in the reference case from Chapter 3.4.2.

The passability has no influence on the water velocity variation for the same simulation conditions.

On the other hand, the pressure difference along the porous concrete layers as a result of this simulation case is 180 kPa. Compared to the reference case with the same water inlet configuration and same concretes with the linear friction law, this pressure difference is around 75 kPa higher. Under these boundary conditions, although the volume flow rate values of cooling water do not go very high at the inlet, there is still a small non-linearity in the flow, which brings the increase in the total pressure difference when the quadratic flow law is applied.

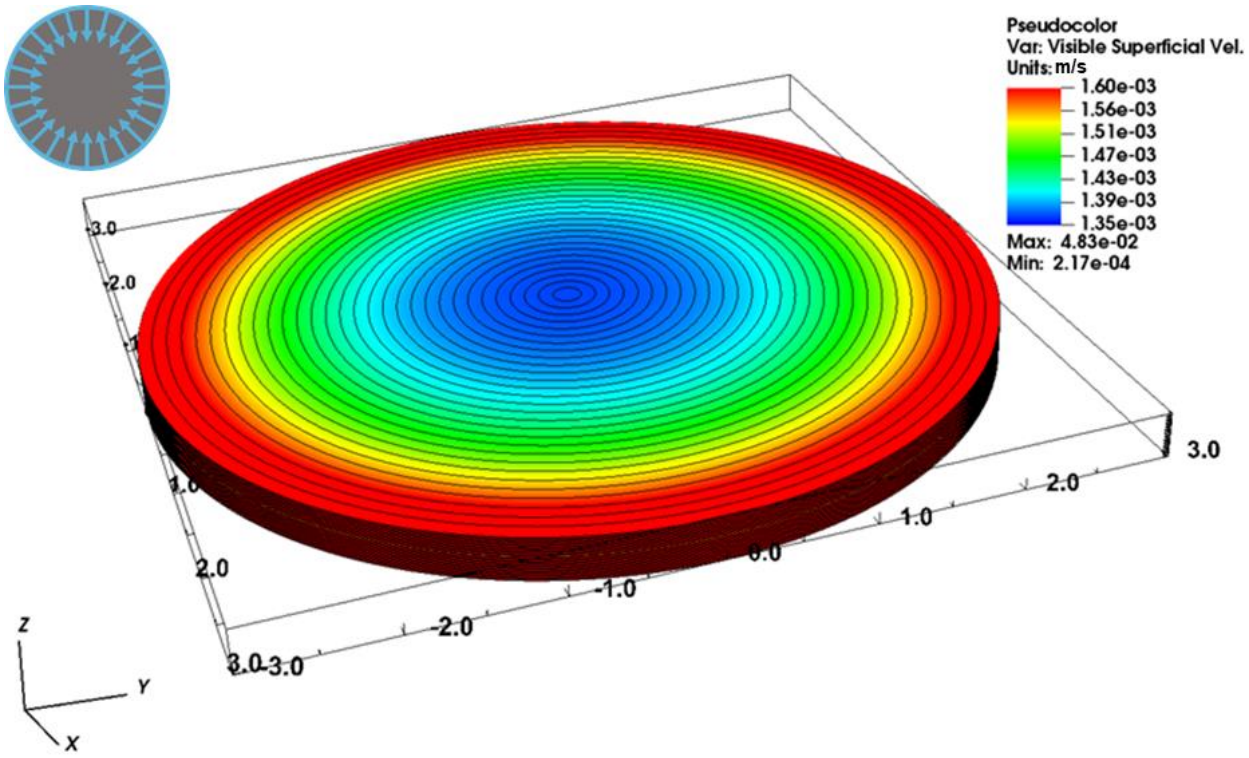

Figure 4.10 Superficial velocity of cooling water in axial direction for simulation Case 3 (circumferential inlet configuration with concrete pairing from reference case with quadratic friction law applied). Water inlet configuration shown in upper left corner.

This simulation case shows that it is important to determine the real friction relation for water coolant flow through porous core catcher in order to avoid underestimating the inlet pressure for the passive flow.

4.3.4 Case 4

For the simulation Case 4 the concrete pairing from Case 3 is used as core catcher and the cooling water is provided only from a single inlet connection. The simulation Case 4 can be considered as the simulation case from Chapter 3.6 with more realistic friction law for water flow through porous concrete.

As can be seen in Figure 4.11, the superficial velocity in axial direction on the core catcher surface varies between 0.0008 m/ and 0.008 m/s. With the effect of permeability the water is distributed as expected in less uniform way compared to simulation from Chapter 3.6 and 1/3 of the surface is provided with cooling water of 0.0008 m/s velocity, which is lower that the aimed superficial water velocity of 0.0015 m/s.

Moreover, with the effect of high water velocities at the water inlet the total pressure difference in the core catcher reaches to 16 MPa which is extremely high for a reactor application.

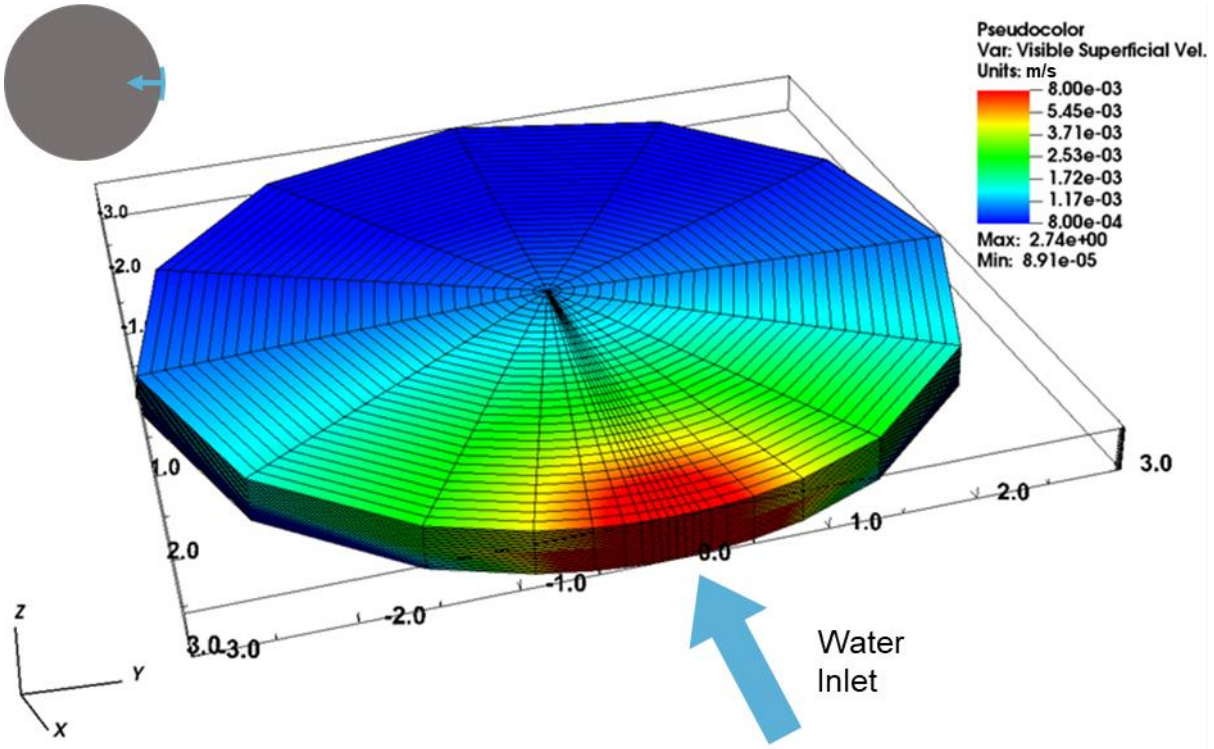

Figure 4.11 Superficial velocity of cooling water in axial direction for simulation Case 4 (single inlet configuration with concrete pairing from reference case with quadratic friction law applied). Water inlet configuration shown in upper left corner and water inlet point is indicated.

4.3.5 Case 5

For the simulation Case 5, the optimization method developed in Chapter 3.5 is applied to determine a concrete pairing with their permeability and passability values that deliver cooling water uniformly on the melt contact surface for single inlet point.

It is clear from the previous investigations in this work that by decreasing the permeability and passability of the upper concrete layer for the same lower layer, the cooling water can be distributed more evenly along the cavity. However, it is equally clear that such a concrete pairing will require even higher pressure values at the cooling water inlet. Increasing the permeability and passability of both layers once the even distribution is reached might decrease the pressure to certain extend.

Table 4.6 shows the permeability and passability values of a concrete pair obtained with optimization, which delivers the coolant sufficiently uniform to the melt layer.

Table 4.6 Permeability and passability of the concrete layers that provides cooling water uniformly to the melt layer from single inlet point when the quadratic friction law from the measurements applied.

	Permeability [m^2]	Passability [m^{-1}]
Upper layer	7.68×10^{-13}	2.98×10^{-9}
Lower layer	7.31×10^{-8}	2.83×10^{-4}

As the Figure 4.12 shows, the aimed superficial velocity in axial direction is reached uniformly on the entire surface of the core catcher device except for the very small region right by the inlet that has a slightly higher velocity.

However, the corresponding pressure difference along the core catcher is still around 700 kPa, which is considerably high for reactor application. Another limitation to consider for this configuration is that the permeability of the lower concrete layer is already quite high for a standard porous concrete, which can cause structural problems, and the permeability of upper concrete layer is quite low for a standard porous concrete, which will be challenging to manufacture.

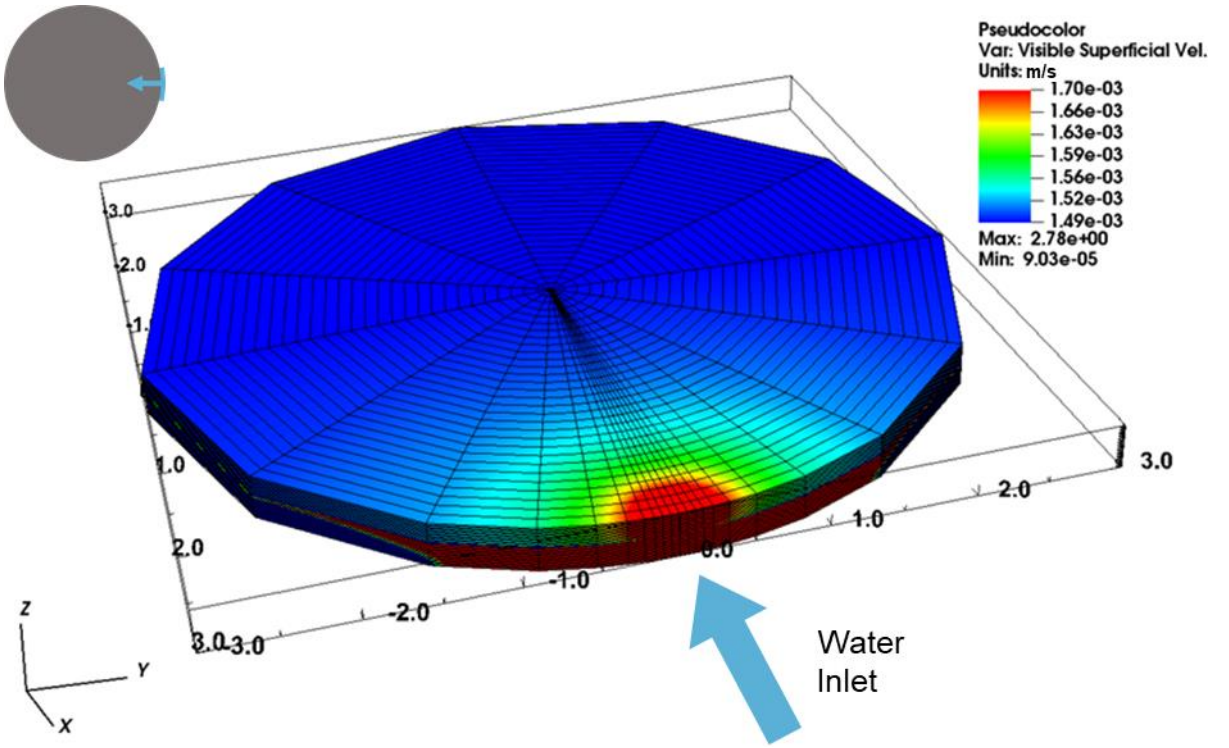

Figure 4.12 Superficial velocity of cooling water in axial direction for simulation Case 5 (single inlet configuration with concrete pairing that provides uniform flow with quadratic friction law applied). Water inlet configuration shown in upper left corner and water inlet point is indicated.

Table 4.7 summarizes the simulation cases from this section. Permeability and passability values of the concrete pair used as core catcher, water inlet configuration, the resulting total pressure loss in the core catcher, and weather or not the cooling water was provided with sufficient cooling water superficial velocity along the entire surface of core catcher.

Case 3 and Case 5 are the cases that provided the cooling water with superficial velocity sufficiently close to required 1.5 $x10^{-3}$ m/s along the entire surface. Case 3, which was simulated with circumferential water inlet can be still improved by applying lower permeable concrete pair which can result in more applicable pressure input requirement for the reactor. Case 5 on the other hand, already has a very high permeable lower layer and very low permeable upper layer. It can be concluded based on this section that the back fitting of the porous concrete core catcher device with limited water inlet configuration can raise many challenges. Increasing the area of the water inlet and providing it uniformly from the perimeter of the porous core catcher device is more feasible approach for the reactor application.

Table 4.7 Pressure difference in the core catcher for each simulation case.

	Core Catcher Concrete			Total Pressure Difference in Core Catcher, Δp [kPa]	Sufficient Cooling Water on the entire Surface	Inlet Config-uration
	Layer	Permeability [m^2]	Passability [m^{-1}]			
Case 1	Upper	$2.12x10^{-9}$	$8.23x10^{-6}$	415	NO	Single Inlet
	Lower	$4.09x10^{-8}$	$1.84x10^{-4}$			
Case 2	Upper	$2.12x10^{-9}$	$8.23x10^{-6}$	3	NO	Circum-ferential Inlet
	Lower	$4.09x10^{-8}$	$1.84x10^{-4}$			
Case 3	Upper	$1.96x10^{-12}$	$7.63x10^{-9}$	180	YES	Circum-ferential Inlet
	Lower	$1.46x10^{-9}$	$5.67x10^{-6}$			
Case 4	Upper	$1.96x10^{-12}$	$7.63x10^{-9}$	16000	NO	Single Inlet
	Lower	$1.46x10^{-9}$	$5.67x10^{-6}$			
Case 5	Upper	$7.68x10^{-13}$	$2.98x10^{-9}$	700	YES	Single Inlet
	Lower	$7.31x10^{-08}$	$2.83x10^{-4}$			

4.4 Application of the Measurement Results to CometPC experiments

Knowing the flow behavior through porous concretes used in CometPC experiments has a significant importance in terms of exploring the melt cooling and solidification via bottom flooding. The concrete samples provided by KIT for the permeability measurements in this work were prepared the same way with the concrete pair used in CometPC Plus experiment. Applying the now known permeability and passability values to the experiment geometry and boundary conditions from CometPC Plus experiment can provide an insight in to the cooling water progress in the melt layer.

4.4.1 CometPC Plus Experiment

CometPC Plus is the most recent CometPC experiment that was performed in KIT. In Chapter 1.2 general information on CometPC experiments including CometPC Plus is provided. Some important data from the CometPC Plus experiment can be seen in Table 1.2. Figure 1.6 shows a picture that was taken during CometPC Plus experiment catching the violent interaction between hot melt and cooling water, and a picture of a post-test solidified melt cross-section. CometPC Plus experiment has resulted with melt being successfully arrested and cooled.

The cooling water was provided on the side of lower concrete layer from four points and these four feed lines were connected to main water feed line which was connected to the water tank. The water tank was positioned with an elevation so that the cooling water could be supplied with an effective over pressure of 0.2 bars (20 kPa). As mentioned in Chapter 1.2, effective overpressure is a term used in COMET and CometPC experiments to describe the pressure value which is the difference between the hydrostatic pressure of cooling water and the hydrostatic pressure of melt on the core catcher surface level. Meaning, after the expected hydrostatic pressure of melt is compensated by cooling water, this effective overpressure is what remains from the input.

Figure 4.13 shows the measured cooling water inflow rates and taken directly from the experiment report [27]. The blue line is the total water inflow rate. The ignition of the thermite material is at time=0, and at around 180 second mark the water is in the water feed line. According to the experiment, 207 seconds after the ignition, cooling water begins to flow into the melt.

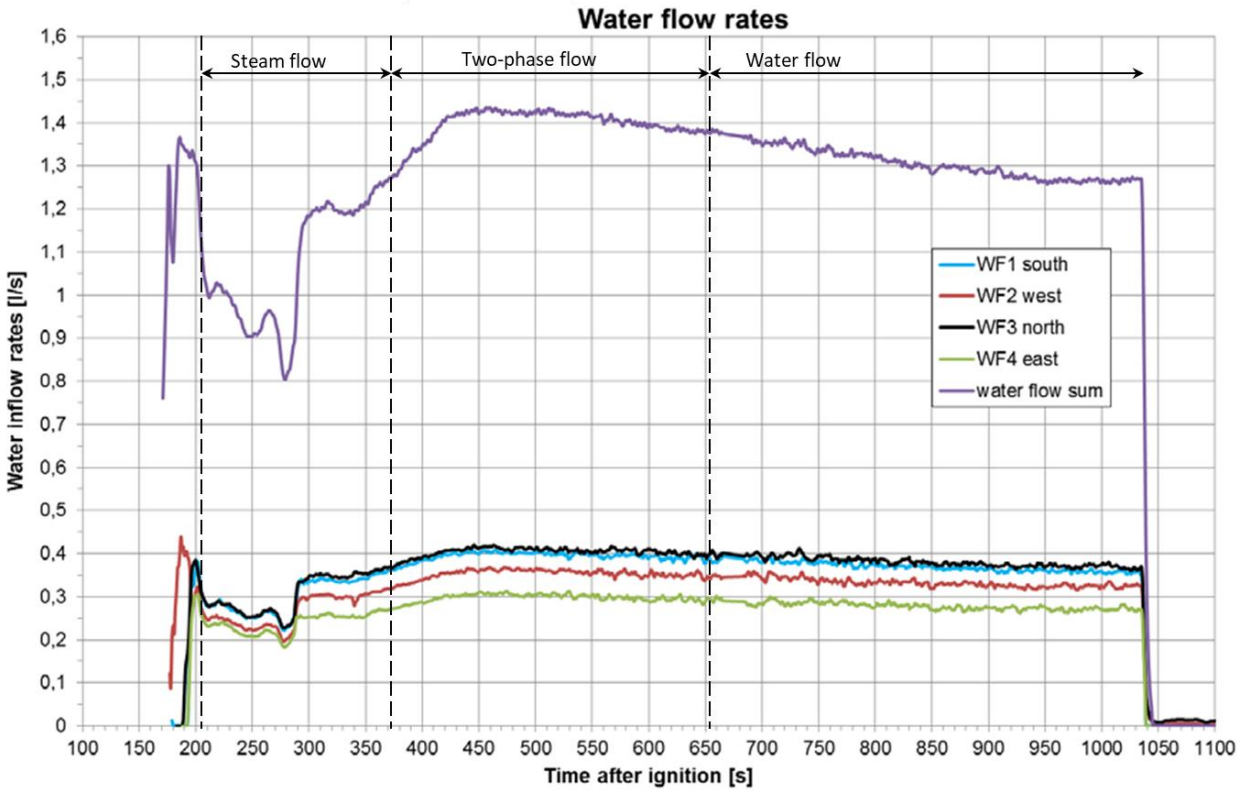

Figure 4.13 Change in water flow rate at the feed line during CometPC Plus experiment according to the experiment report [27]. The flow phase of the coolant after it meets the melt is indicated on the diagram for the purpose of the analysis in this work based on the observations from the experiment.

Although the nature of the experiment brings some uncertainties, it is still possible to have an information on the event progress based on the data collected from instrumentation and the camera positioned right above the open-air experiment set-up, which provides the bird eye view to the interaction between coolant and melt. Based on this collected information and observations the flow phase of the coolant through the melt for

each experiment is predicted and indicated on the Figure 4.13 for the purpose of the analysis performed in this work. The flow phases could be assumed as follows: Between the 207 second mark after ignition up to 370 second steam flows through the molten corium. Between the seconds 370 and 654 the coolant flow upwards as two-phase and after 654 second mark the corium is completely solidified and coolant flows upwards as single-phase liquid and starts accumulation on the surface.

By this indication, total inflow rates measured during each phase can be seen on Figure 4.13 (purple line). It can be seen that although the flow rate fluctuates initially, almost the same flow rate is observed at the very beginning and at the very end of the cooling. Thus we know the flow rates reached during the flow phase.

The coolant flow for CometPC Plus experiment can be simulated for the core catcher geometry and concrete properties in order to see the pressure loss in the concrete layers under the experiment parameters and its relation to the progress of the cooling.

4.4.2 Simulation of CometPC Plus Coolant Flow Rates

The aim of these simulations is to determine the pressure loss in the concrete layer during CometPC experiments, its relation to the progress of the cooling and to compare this pressure loss with the effective overpressure of the cooling water. It should be stated that the transients of cooling water while flowing through compact melt layer are still unclear and the simulations in this section are not transient simulations. The simulations in this section are single-phase water flow through porous core catcher for CometPC experiment data. The coolant inflow rates measured in the experiment are imposed as constant flow rates.

The simulations are performed with COCOMO3D code with the domain built as seen in Figure 4.14. In CometPC experiments the cooling water was provided by four channels around the bottom concrete layer positioned across from each other symmetrically. Since in the relatively small diameters of the experiments this positioning of the water inlet provides a high homogeneity, for the simulations, the total area of the water inlet is taken as circumferential around the perimeter of bottom layer. This configuration does not have an effect on the outcome of the simulations and decreases the computational load since it brings cylindrical symmetry to the calculation domain. The porous solid structure consists of CometPC core catcher and the geometry of the core catcher is given in Table 1.2

The ambient pressure is imposed as boundary condition at the cooling water outlet. For the inlet, the water flow rates measured in experiment are defined as a constant boundary condition and varied for each simulation. The temperature that was measured in the crucible during the test was also assumed as the temperature of the water flowing in the system and the cooling water properties for the simulations were taken according to this temperature values.

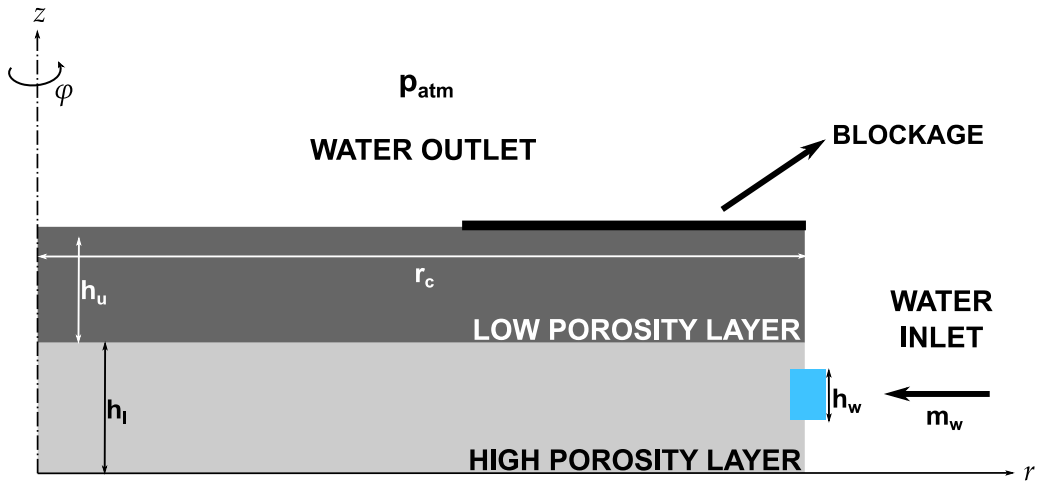

Figure 4.14 Sketch of COCOMO3D simulation domain for CometPC simulations.

The blockage that is seen on the Figure 4.14 represents part of the sacrificial layer that has not been ablated during experiments. During most of the CometPC experiments the sacrificial layer has been only partially ablated, which can also clearly be seen in post-test pictures. Since the exact amount of opening was not clear for the Comet PC Plus experiment, the simulations are performed under four assumptions for the sacrificial concrete; 100% ablated (completely open flow into the melt layer), 80% ablated, 50% ablated and 20% ablated.

Figure 4.15 shows the simulation results. The x-axis is the flow rate of the coolant imposed in simulations and y-axis is the resulting pressure loss in the porous concrete layers of the core catcher due to friction (Δp_f *Porous Concrete*) in relation to effective overpressure of the experiment, of 0.2 bar (20 kPa). The relation of these parameters is shown for each assumption of the sacrificial concrete (SC) ablation rate. The phases of the coolant flow are indicated on the Figure 4.15 for the flow rate range they were observed as given on Figure 4.13.

As it can be seen on the figure, for the observed water inlet flowrate during experiment, part of the effective overpressure is compensated in the porous concrete due to friction losses and a significant portion of the overpressure is not. According the Figure 4.15, for the assumption of where sacrificial concrete is ablated 50% or more, the pressure loss in the porous concrete layers is around 20% of the effective overpressure. For cases where sacrificial concrete is ablated less, the ratio of the pressure loss in the porous concrete layers increases significantly, however, there is still another part of the system that causes pressure losses. A certain pressure loss occurring at the inlet lines of the cooling water, before reaching to the porous concrete, could be a contribution to this pressure loss outside of the porous concrete layers. However, based on the significance of this pressure loss ratio, it can be interpreted that the melt layer itself is actually imposing pressure losses.

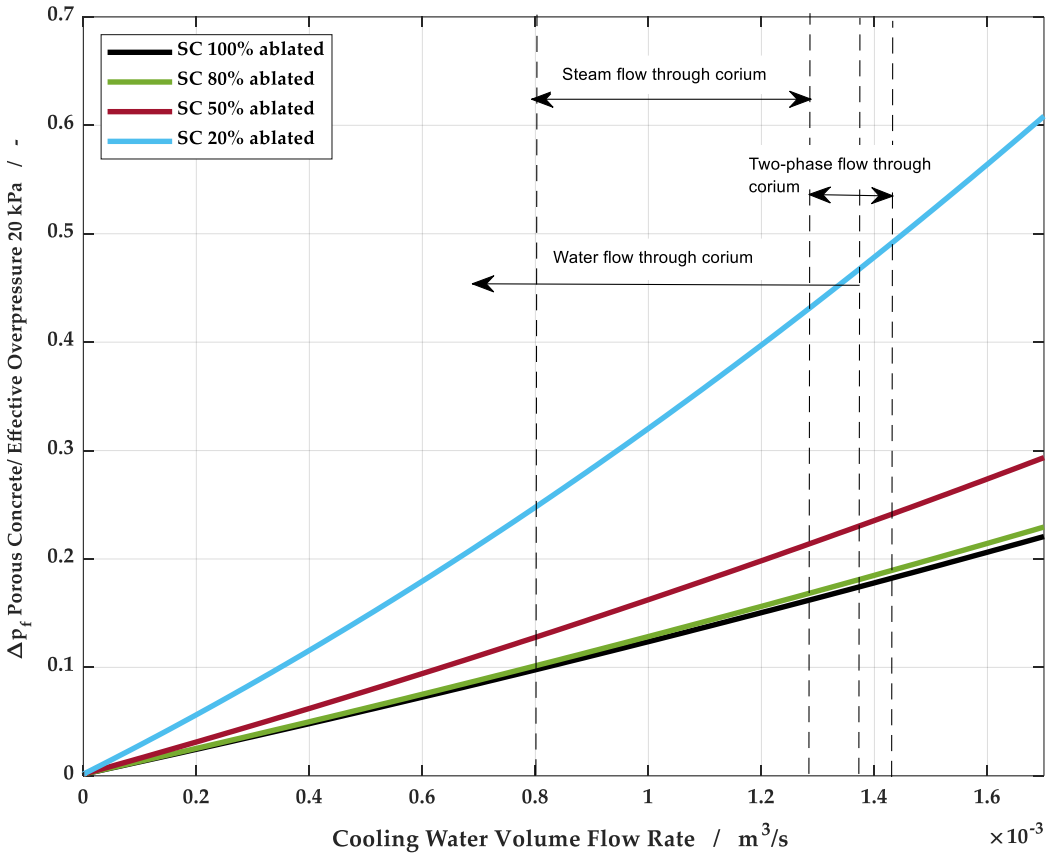

Figure 4.15 COCOMO3D Simulation results for the pressure loss due to friction in porous concrete layers in relation to effective overpressure for the CometPC Plus experiment.

Even with the consideration of other effects on the pressure losses in the system, based on this analysis, a significant pressure loss is imposed by the melt layer. It should be stated that the investigations performed in Chapter 3 are, as explained, independent from the pressure loads at coolant inlet and outflow. With the assumption that these pressure losses imposed by melt are uniform along the radial direction, this pressure value can be taken as an outflow boundary condition in addition to hydrostatic pressure of melt. Which then means that, this additional load should be considered for the required inflow pressure of the coolant.

This evaluation once again shows the importance of the modelling of porosity formation in the compact melt layer during bottom cooling, as the resulting pressure loss values would have an implication on the device and cooling set-up in a reactor application. The next chapter of this work presents a new approach and model for modelling of porosity formation in melt layer.

5 Modelling of Melt Fragmentation and Porosity Formation in Melt Layer

Fragmentation of molten corium due to bottom cooling is a topic that still requires further investigation in severe accident research. Since the experimental investigations show successful fragmentation and porosity formation for solidified corium, it is essential to model this phenomenon suitably. An accurate modelling of melt fragmentation and final void fraction in the solidified corium layer improves the ability of simulation codes to predict corium coolability via bottom flooding in reactors.

This chapter presents a new interfacial friction model for molten corium-steam two-phase flow that represents the physics of melt fragmentation via bottom flooding and can simulate the porosity values of the solidified corium layer. The chapter starts with discussing the modelling approach that is taken in this work in order to model porosity build up. Following this, with a specifically written stand-alone simulation code, the existing two-phase flow friction laws from literature are evaluated for their applicability to physical properties of steam and molten corium with the boundary conditions during bottom flooding in ex-vessel. This evaluation is followed up by introducing the new friction model for molten corium-steam two-phase flow and the stand-alone simulations with the new friction model.

Finally, the new friction model and the molten corium liquid properties are implemented in COCOMO3D. The first set of COCOMO3D simulations takes the CometPC geometry and experiment parameters in order to validate the void of the model against porosity of the experiments. In addition, the last set of simulations takes a generic reactor cavity diameter and expected corium levels in order to predict the corium fragmentation in reactor application of bottom cooling.

5.1 Considerations and Assumptions for the Modelling Approach

The observations and measurements from COMET and CometPC experiments provide the information for the estimation and assumptions for the molten corium cooling via bottom-flooding. These information and assumptions are also discussed in Chapter 1.2.3 and Chapter 4.4. During cooling of the molten corium via bottom-flooding, water flows through the porous concrete layer towards the melt layer upon the ablation of the sacrificial concrete. Initially water is evaporated in a relatively small region around the melt-concrete interface and steam flowing upward through the melt layer creates a two-phase flow. Void in two-phase region is governed by the balance between evaporation of injected water at the bottom and hold-up of the steam due to friction between steam and melt in the melt layer. Void leads to swelling of the melt layer into melt continuous but high void, foam-like structure. Consequently, gradual cool down of the melt due do its large solidus-liquidus range leads to a strong increase in melt viscosity and finally freezing, conserving the void as pores. This fragmentation or porosity formation phenomenon during bottom flooding is a highly complex 3-phase flow phenomenon where steam, water and liquid corium co-exist.

The crucial process for a successful cooling is sufficient break-up of the compact corium layer and the formation of a coolable porous structure. Therefore, the essential process to model is the initial two-phase flow of liquid corium and steam with the actual movement of the fluids. This way, the melt break-up can be described more realistically with steam penetrating into compact corium and creating flow patterns due to movement of liquid corium and steam. This modelling enables simulations to predict the coolant ingression into melt for a reactor case more realistically. Due to challenges of 3-phase flow modelling and time limitations, this work pursues a modelling approach that focuses on steam-melt two-phase flow with the assumption that the void that occurs during this steam-melt two-phase flow stays almost the same for the solidified melt as pores. This assumption is supported by the presented CometPC Plus experiment. The water head stays constant throughout the experiment and except a small fluctuation region the coolant flow rates stay almost constant and the same as the initial flow rate, see Figure 4.13.

The evaporation front of the cooling water around the melt-concrete interface is assumed to be very narrow, and the initial shape of the corium upon two-phase flow with steam is preserved almost the same in the solidified corium. Another supporting argument for the applicability of this approach is that, due to the violent and ever-changing interaction of the corium and coolant the initial effect of the evaporation and resulting volume change will not last. Whereas, the flow of the high velocity steam through liquid corium will be the decisive phenomenon and will have the lasting effect on the fragmentation. Moreover, the strong evaporation might not always lead to pressure build up. If the steam finds preferred paths, it might escape the melt rapidly, without interacting, hence causing low porosity. Figure 5.1 illustrates the main approach of the current work for modelling of the fragmentation/porosity formation in corium layer by bottom flooding.

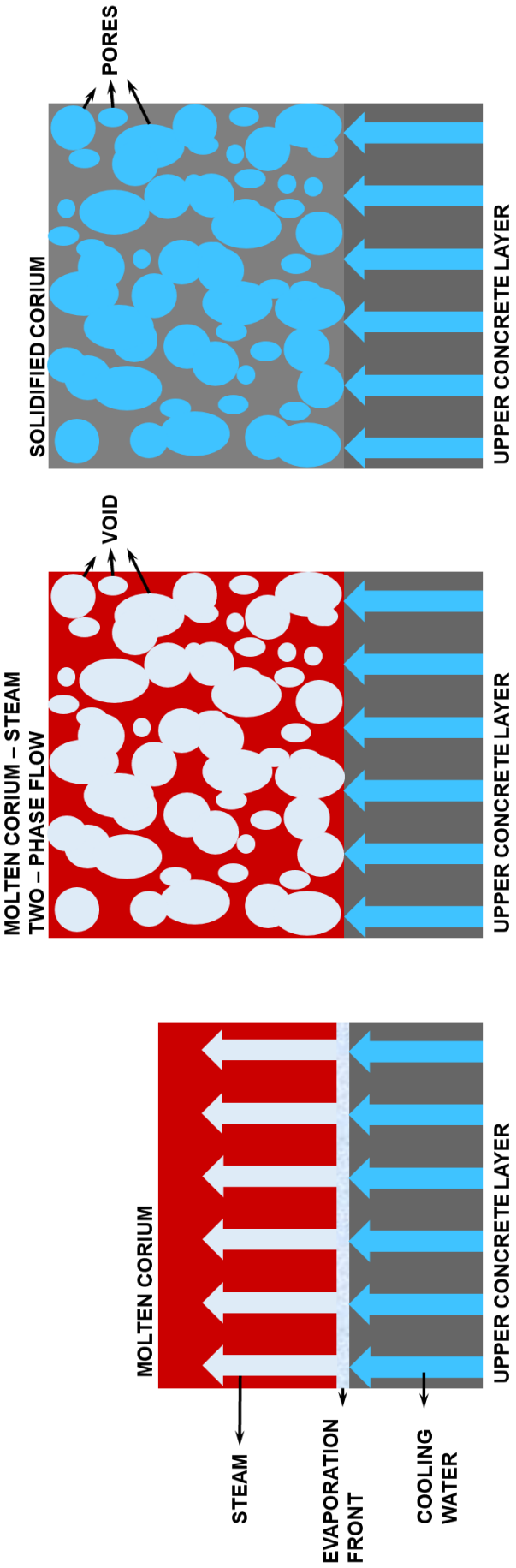

Figure 5.1 Illustration of the porosity formation modelling approach.

The two-phase flow of steam and melt is assumed as a pool flow where the wall friction is neglected. As the high melt temperature is dominant, the temperature difference between steam and melt is expected to be small enough that for the two-phase flow modelling approach in this chapter the heat exchange between steam and melt is neglected. The momentum exchange between steam and melt is assumed to be mainly influenced by drag forces, therefore the diffusion fluxes and the shear stress are neglected at this stage. The inertial terms for the momentum equation are neglected as well, and for the one-dimensional steady-state two-fluid two-phase flow of melt and steam, the simplified momentum conservations equations are defined as follows:

$$-F_{mst} = \alpha \frac{dp}{dz} + \alpha \rho_{st} g \tag{5.1}$$

$$F_{mst} = (1-\alpha) \frac{dp}{dz} + (1-\alpha) \rho_m g \tag{5.2}$$

Equation (5.1) and Equation (5.2) are the simplified momentum conservation equations for steam and melt respectively. F_{mst} is the momentum exchange between melt and steam due to friction forces, α is the void fraction (volume fraction of steam), $\frac{dp}{dz}$ is the pressure gradient in the axial direction of the pool, ρ_m is the density of the molten corium (or melt), ρ_{st} is the density of the steam, and g is the gravitational acceleration. The void fraction, α can be estimated from the momentum balance based on the interfacial friction force F_{mst}.

The momentum conservation equation for liquid and gas phases exist in COCOMO3D code in complete form as described in Chapter 2.3. The simplified momentum equations (5.1) and (5.2) are used in the stand-alone simulation code written for the analysis in this chapter in order the evaluate the real effect of the models before implementing it into the complex COCOMO3D code.

5.1.1 Material Properties and Boundary Conditions

For the investigations, the boundary conditions are based on COMET research and CometPC experiments, as these experiments provide the reference point for void fraction. As it can also be seen on Table 1.2, the highest temperatures seen during CometPC experiments are around 2200 K and pressure values are around 1.2 bar [23] [24] [27]. It should be mentioned here that for the reactor case higher temperatures for typical corium (up to 2800 K) and higher pressure values are expected depending on the porous concrete and storage set up. As for the physical properties of melt, based on the CometPC reports, the melt used in the experiments had a density between 3000 kg/m^3 and 5000 kg/m^3 whereas the density of a typical corium could be higher depending on the amount of concrete that is mixed in the ex-vessel conditions. Table 5.1 shows some of the physical properties of ex-vessel corium when it is mixed in varying degrees with siliceous sacrificial concrete [80] [81] [82].

As bottom cooling inherently requires sacrificial concrete to ablate (at least to some extent), it can be assumed that the density of the corium that needs to be cooled will be below 7000 kg/m^3.

Based on this information, for the investigations during model development in this chapter the material properties as given on Table 5.2 are applied. For steam data, the properties at 2200 K and 1.2 bar are used. The investigations are carried out for the high velocity values reached by steam in bottom cooling conditions. In order to do so, the mass flux of the coolant is varied up to 5.60 kg/m^{2}s which corresponds to superficial velocity of approximately 6x10^{-3} m/s for water supply and a superficial velocity of 45 m/s for steam for complete evaporation. As these velocity values could be reached by water or steam in case of partial opening of the sacrificial concrete surface of the core catcher, it is important for the developed model to cover this range of velocity.

Table 5.1 Physical properties of ex-vessel corium.

	Initial Corium	~20% Concrete	~30% Concrete	~40% Concrete	~50% Concrete
Density [kg/m^3]	7000	5500	5000	4600	4500
Viscosity [Pa.s]	0.01	0.015	0.02	0.024	0.025
Surface Tension [N/m]	0.47	0.455	0.448	0.445	0.44

Table 5.2 Physical properties of steam and melt used in two-phase flow friction force modelling

	Melt	Steam
Density [kg/m^3]	4000	0.12
Viscosity [Pa.s]	0.02	7.69x10^{-5}
Surface Tension [N/m]	0.4	

5.2 Applicability of Interfacial Frictions Models from Literature

This section investigates the applicability of various friction or void fraction models from literature to the material properties and boundary conditions during bottom cooling as mentioned in previous section. As some of these models claim to be applicable to a wide range of parameters, the compatibility or possible limitations of these models provide valuable information on the specific modelling requirements for the steam-melt two-phase flow under bottom cooling conditions.

5.2.1 Drift Velocity Approach

Drift velocity modelling is part of drift flux modelling of two-phase flow where the fluids of the flow are modelled as a mixture. It is one of the two most common approaches for predicting the void fraction in two-phase flow and in reactor simulation codes, with other being the drag coefficient approach. The drift velocity approach is found to be suitable for pool flow type of water-gas interactions where the gas flow rate is very small [53] [70].

Void fraction calculation by drift velocity approach is more straight forward and relatively simple compared to determining void fraction for the separated flow models, however due to the less flexible simplified modelling, the application of drift velocity models might be limited. In this section the drift velocity model for pool flow by Ishii [50] [51], which is one of the most widely used model, is applied to material properties of molten corium and steam for higher steam flow rates. By rewriting the Equation (2.16) from Chapter 2.2, the void fraction with drift flux modelling is calculated as follows [51]:

$$\alpha = \frac{j_{st}}{C_0 j + V_{gj}} \tag{5.3}$$

Where α is the void fraction (gas phase volume ration), j is the total volumetric flux (total superficial velocity), j_{st} is the superficial velocity of the steam and V_{gj} is the average local drift velocity. The distribution parameter C_0 is described by Ishii for a pool flow in a round geometry as follows [51]:

$$C_0 = 1.2 - 0.2\sqrt{\frac{\rho_{st}}{\rho_m}} \tag{5.4}$$

Where ρ_{st} is the steam density and ρ_m is the molten corium density.

The average local drift velocity for this flow is modelled as follows [51]:

$$V_{gj} = \sqrt{2}\left(\frac{\sigma_m(\rho_m - \rho_{st})}{{\rho_m}^2}\right)^{0.25} \tag{5.5}$$

Where σ_m is the surface tension between steam and melt.

Material properties from Table 5.2 are used in order to calculate the void fraction in corium melt for a large variety of cooling water mass fluxes by the stand-alone simulation program. For the assumption that the entire cooling water evaporates at the base of the melt pool, the mass flux of steam is equal to the mass flux of water. The superficial velocities of water and steam can be calculated for given densities and mass fluxes of the water as follows:

$$j_w = \frac{\varphi_w}{\rho_w} \tag{5.6}$$

$$j_{st} = \frac{\varphi_{st}}{\rho_{st}} \tag{5.7}$$

Where j_w is the superficial velocity of water, j_s is the superficial velocity of the steam, ρ_w is the density of water, ρ_{st} is the density of steam, φ_w is the mass flux of the water and φ_{st} is the mass flux of the steam. Water properties are taken for water at 303 K and 1.2 bar. To realize the pool flow conditions, the initial average mass flux and velocity of the melt pool are set to zero.

For the known void fraction, the real velocities of steam, v_{st}, and melt, v_m, during two phase flow are calculated respectively as follows:

$$v_{st} = \frac{j_{st}}{\alpha} \tag{5.8}$$

$$v_m = \frac{j_m}{1-\alpha} \tag{5.9}$$

The drift velocity model for pool flow by Ishii assumes a churn flow regime for the pool flow and it is claimed to show good results for moderate gas flow rates [53] [70].

The results for the steam flow rates from the CometPC experiments with the material properties from the experiments can be seen in Figure 5.2.: The graph shows the relation between void fraction in melt pool and superficial velocity of the cooling water that is provided to the hot melt, determined by application of the drift flux model by Ishii in the stand-alone simulation program as described. Although the water velocity is used for the relation in the diagram for better understanding of the coolability, the superficial velocity values of the steam are also indicated on the diagram as these values were directly used in the simulations. The rectangular region with the dashed lines on the diagram indicates the range of water flow rates that were measured in CometPC experiments and the porosity values observed as a result.

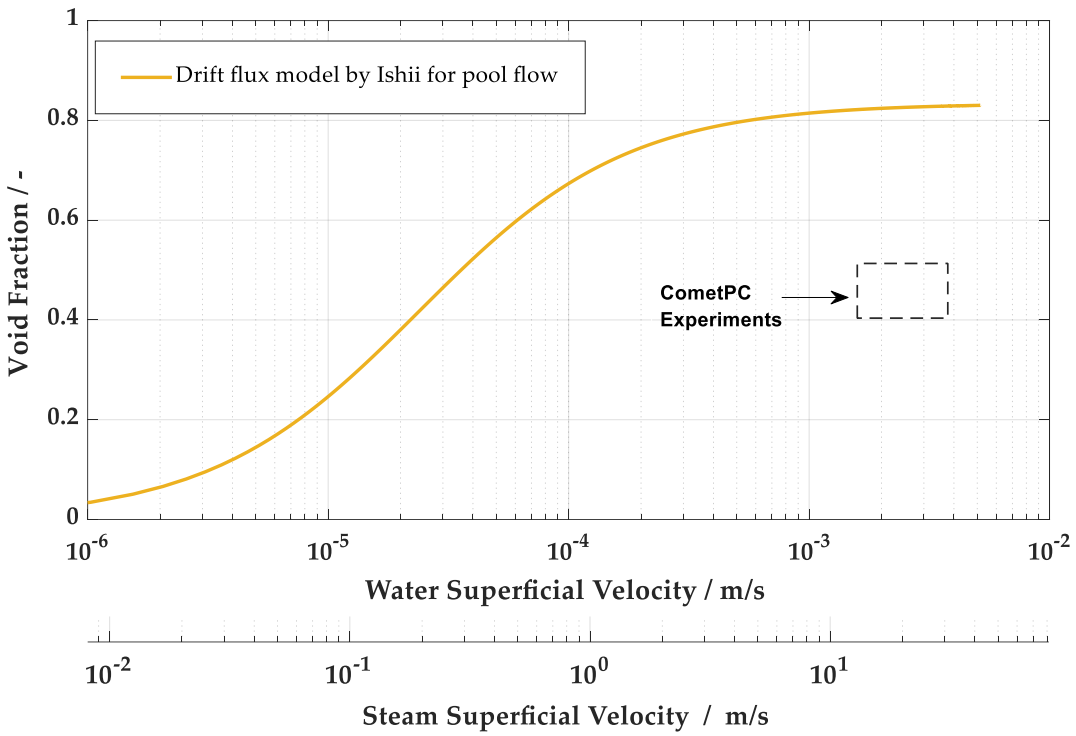

Figure 5.2 Relation between the void fraction in the melt pool and superficial velocity of cooling water (and steam) according to drift flux model by Ishii. The cooling water flow rate values and final porosities observed in CometPC experiments are indicated on the diagram with a rectangular region within dashed lines.

As it can be seen on the Figure 5.2, the resulting void fractions are much higher than the void values from CometPC experiments. The reason is that the friction between the phases is highly overestimated by this model for the bottom cooling conditions. The majority of two-phase flow modelling roots back to water-steam two phase flow and the assumptions for drift flux approach rooted in water and steam flow are not suitable for corium properties and steam velocities for bottom cooling conditions. In fact, it can be seen in the literature that for fluids other than water, adapted drift flux modelling with very specific drift velocity definitions with limited applicability is used. Appendix C shows two different drift velocity models that are used for heavy-liquid-gas two-phase flow as an example. These models are not suitable for melt-steam two-phase flow in this work, as they have a very limited application range therefore cannot estimate the void fraction for the bottom flooding conditions. Nevertheless, based on this observation it can be emphasized again that the special flow conditions and fluids require new models for better estimation of the flow.

5.2.2 Drag Coefficient Approach

The second most widely used approach for two-phase flow modelling is two-fluid modelling where the fluids of the flow are modelled separately. The interfacial friction force of the two-fluid two-phase flow is defined by the drag force and drag coefficient. Drag force modelling approach by Ishii for the two-fluid flow modeling is used very widely for predicting void fraction in two-phase flow in reactor simulation codes and has been applied in variety range of gas-water two-phase flow in the reactor [46] [47] [48].

Constitutive relations for drag force and drag coefficient closures for momentum exchange in two-phase modelling by Ishii has a wide range applicability. However, it requires more detailed modelling of the interaction between the two phases in order to obtain the void fraction. The momentum exchange between melt and steam can be expressed analog to Equation (2.14) from Chapter 2.2 as follows:

$$F_{mst} = -\frac{3}{8}\frac{s_d}{r_d} C_D \rho_c v_r |v_r| \tag{5.10}$$

Drag force modelling by Ishii defines three main flow regimes and pattern for pool flow as shown in Figure 5.3. Two-phase flow for void fraction value 0.3 and below is defined as bubbly flow where the gas phase is dispersed in continuous liquid phase. For void fraction values between 0.3 and 0.7, the flow regime is called churn turbulent flow, which is a liquid continuous flow with foam like structure. For void fraction values 0.7 and above, the flow regime is droplet flow where liquid droplets are dispersed in continuous gas phase. For the investigations in this section, the flow regions and the flow regime criteria are taken according to this definition.

Bubbly Flow $\alpha \leq 0.3$ | *Churn Turbulent Flow* $0.3 < \alpha < 0.7$ | *Droplet Flow* $0.7 \leq \alpha$

Figure 5.3 Different flow regimes of two-phase flow and flow regime criteria given by drag force modelling by Ishii for pool flow.

For each of these flow regimes the radius of the dispersed phase, r_d, and drag coefficient C_D is modelled differently by Ishii and these equations are described as follows as they are implemented in this work:

- **Drag force for bubbly flow , $\alpha \leq 0.3$:**

For bubbly flow, where the melt is the continuous phase and steam is the dispersed phase, the Equation (5.10) can be rewritten for bubbly flow drag force, $F_{mst,bb}$, as follows:

$$F_{mst,bb} = -\frac{3}{8}\frac{\alpha}{r_{bb}} C_{D,bb}\rho_m v_r|v_r| \tag{5.11}$$

Where ρ_m is the density of the melt, α is the volume fraction of the steam, r_{bb} is the radius of the steam bubbles v_r is the relative velocity and $C_{D,bb}$ is the drag coefficient for the bubbly flow. $C_{D,bb}$ is defined for viscous and distorted particle regime separately [42]:

$$C_{D,bb,vis} = \frac{24(1 + 0.1N_{Re}^{0.75})}{N_{Re}} \tag{5.12}$$

$$C_{D,bb,dist} = \frac{4}{3} r_{bb} \sqrt{\frac{g(\rho_m - \rho_{st})}{\sigma_m}} \left[\frac{1 + 17.67(1-\alpha)^{1.29}}{18.67(1-\alpha)^{1.5}}\right]^2 \tag{5.13}$$

Where $C_{D,bb,vis}$ is the drag coefficient for viscous bubbly flow regime and $C_{D,bb,dist}$ is the drag coefficient for distorted bubbly flow regime, ρ_{st} is the steam density and N_{Re} is the Reynolds Number for multi-particle system. The bubble radius seen in Equations (5.11)and (5.13) and is calculated based on Taylor instability for maximum bubble radius as follows [45]:

$$r_{bb} = 2\sqrt{\frac{\sigma_m}{g(\rho_m - \rho_{st})}} \tag{5.14}$$

Where ρ_{st} is the density of the steam and σ_m is the surface tension between steam and melt.

Reynolds number for the multi-particle system is modelled as follows [42]:

$$N_{Re} = \frac{2r_{bb}\rho_m v_r}{\mu_{mix}} \tag{5.15}$$

Where μ_{mix} is the mixture viscosity and modelled for bubbly flow as follows [42]:

$$\mu_{mix} = \frac{\mu_m}{1-\alpha} \tag{5.16}$$

Where μ_m is the dynamic viscosity of the melt.

- **Drag force for churn turbulent flow, $0.3 < \alpha < 0.7$:**

For churn turbulent flow, melt is modelled again as the continuous phase and distorted steam phase modelled as dispersed phase. The Equation (5.10) can be rewritten for churn turbulent flow drag force, $F_{mst,ct}$, as follows:

$$F_{mst,ct} = -\frac{3}{8}\frac{\alpha}{r_{ct}} C_{D,ct}\rho_m v_r|v_r| \tag{5.17}$$

The drag coefficient for churn turbulent flow $C_{D,ct}$ is modelled as follows [42]:

$$C_{D,ct} = \frac{8}{3}(1-\alpha)^2 \tag{5.18}$$

The bubble radius seen in Equation (5.17) is calculated based on Taylor instability for maximum distorted bubble radius as follows [45]:

$$r_{ct} = 4\sqrt{\frac{\sigma_m}{g(\rho_m - \rho_{st})}} \tag{5.19}$$

- **Drag force for droplet flow, $0.7 \leq \alpha$:**

For droplet flow, where the steam is continuous phase and melt droplets are dispersed in steam, the Equation (5.10) can be rewritten for droplet flow drag force, $F_{mst,dt}$ as follows:

$$F_{mst,dt} = -\frac{3}{8}\frac{(1-\alpha)}{r_{dt}} C_{D,dt}\rho_{st} v_r|v_r| \tag{5.20}$$

Where α is the volume fraction of the steam, r_{dt} is the radius of the melt droplets and $C_{D,dt}$ is the drag coefficient for the droplet flow. Similar to the bubbly flow, the drag coefficient for droplet flow is defined for viscous and distorted particle regime separately as well [42]:

$$C_{D,dt,vis} = \frac{24(1 + 0.1N_{Re}^{0.75})}{N_{Re}} \tag{5.21}$$

$$C_{D,dt,dist} = \frac{4}{3} r_{dt}\sqrt{\frac{g(\rho_m - \rho_{st})}{\sigma_m}}\left[\frac{1 + 17.67(\alpha)^{2.57}}{18.67(\alpha)^3}\right]^2 \tag{5.22}$$

Where $C_{D,dt,vis}$ is the drag coefficient for viscous droplet flow regime and $C_{D,dt,dist}$ is the drag coefficient for distorted droplet flow regime. The droplet radius seen in Equations

(5.20) and (5.22) was calculated based on Taylor stability for maximum droplet radius as follows [45]:

$$r_{dt} = 3\sqrt{\frac{\sigma_m}{g(\rho_m - \rho_{st})}} \tag{5.23}$$

For this regime the Reynolds number for the multi-particle system is modelled as follows [42]:

$$N_{Re} = \frac{2r_{dt}\rho_{st}v_r}{\mu_{mix}} \tag{5.24}$$

Where μ_{mix} is the mixture viscosity and modelled for droplet flow as follows [42]:

$$\mu_{mix} = \frac{\mu_{st}}{\alpha^{2.5}} \tag{5.25}$$

Where μ_{st} is the dynamic viscosity of the steam.

In order to solve the momentum Equations (5.1) and (5.2) for void, α, the equations are rearranged as described below.

Both sides of the Equation (5.1) are multiplied by $(1-\alpha)$ and both sides of the Equation (5.2) are multiplied by α:

$$-F_{mst}(1-\alpha) = \alpha(1-\alpha)\frac{dp}{dz} + \alpha(1-\alpha)\rho_{st}g \tag{5.26}$$

$$F_{mst}\alpha = \alpha(1-\alpha)\frac{dp}{dz} + \alpha(1-\alpha)\rho_m g \tag{5.27}$$

The Equation (5.26) is subtracted from Equation (5.27). As the pressure gradient $\frac{dp}{dz}$ is assumed to be equal for both melt and steam, the result is:

$$F_{mst} = \alpha(1-\alpha)(\rho_m - \rho_{st})g \tag{5.28}$$

Equation (5.28) is an explicit equation with void, α, value in both sides of the equation, therefore it should be solved iteratively. The standalone simulation program is written in order to solve α iteratively. The material properties of melt and steam, and a mass flux

value for cooling water are defined in the stand-alone program as input. A range between 0 and 1 is defined for void fraction and an initial value was set to start the iteration. The superficial velocities of water, j_w, and steam, j_{st}, are calculated by Equations (5.6) and (5.7) respectively as explained in Chapter 5.2.1. Water properties were taken for water at 303 K and 1.2 bar. To realize the pool flow conditions, the initial average mass flux and velocity of the melt pool was set to zero. For the known void fraction, the real velocities of steam, v_s, and melt, v_m, during two phase flow are calculated respectively by Equations (5.8) and (5.9).

During simulations, the initial α value is given, F_{mst} is calculated with this α (as $F_{mst,bb}$, $F_{mst,ct}$, or $F_{mst,dt}$ depending on the α), and the residue of Equation (5.28) is checked for the calculated F_{mst}. Void value, α is iterated until the residue approaches to zero. Depending on the void fraction value the drag force is calculated for one of the defined flow regions. For the dispersed flow regions, the drag coefficient C_D is calculated for both viscous and turbulent form and the larger one is taken. This is repeated for a large range of mass flux values of cooling water.

Figure 5.4 shows the relation between void fraction in melt pool and superficial velocity of the cooling water that is provided to the hot melt, determined by application of the drag force model by Ishii in the stand-alone simulation program as described. The superficial velocity values of the steam are also indicated on the diagram as these values were directly used in the simulations. The rectangular region with the dashed lines on the diagram indicates the range of water flow rates that were measured in CometPC experiments and the porosity values observed as a result.

As it can be seen on the Figure 5.4, the resulting void fractions are higher than the void values from CometPC experiments. Similar to the drift velocity approach from previous section, the friction between the phases are is highly overestimated by the drag force model by Ishii for bottom cooling conditions. However, the model has an advantage because of its detailed and flow region-based modelling. Therefore, the drag force approach by Ishii is used as a basis for the model development in this work.

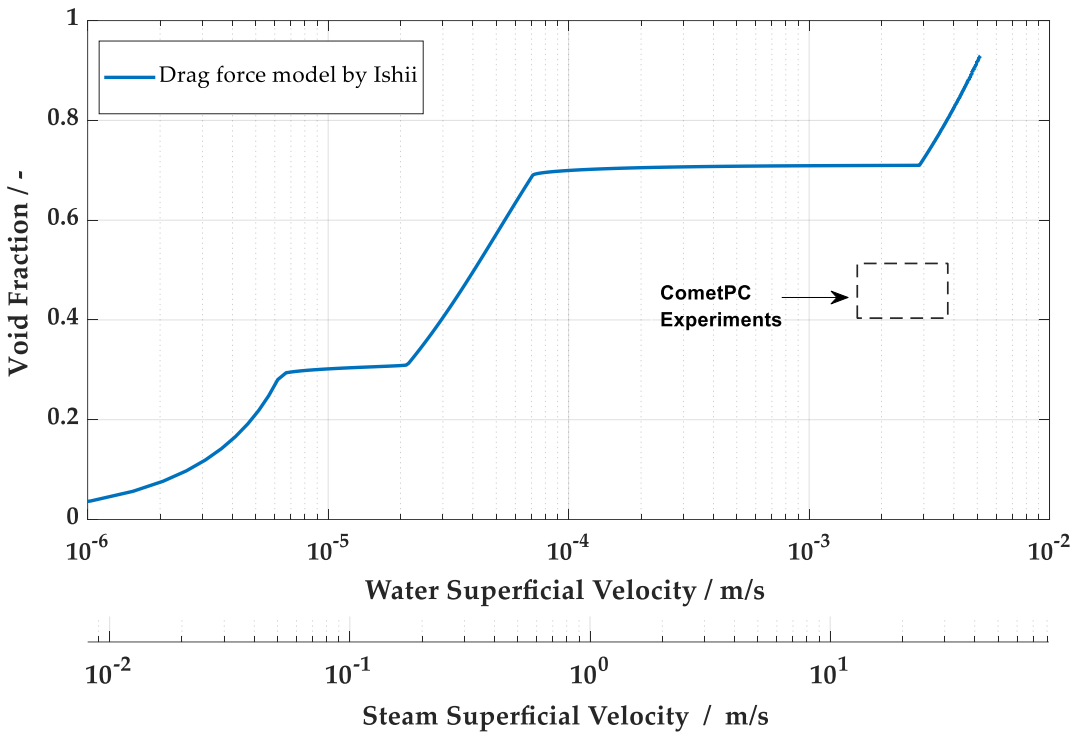

Figure 5.4 Relation between the void fraction in the melt pool and superficial velocity of cooling water (and steam) according to drag force model by Ishii. The cooling water flow rate values and final porosities observed in CometPC experiments are indicated on the diagram with a rectangular region within dashed lines.

The flow region definitions of drag force modelling by Ishii is mostly based on flow in a pipe. The flow patterns and characteristic lengths are based on the considerations coming from water-steam two phase flow in a pipe. This can cause the shortcomings of the model while predicting the void fraction of melt-steam two phase pool flow.

The next section evaluates two existing models that suggest alternative approaches for the flow regimes of drag force modelling for the pool flow.

5.2.3 Alternative Approaches to Drag Force Modelling

For the application of the drag force modelling to geometries that have much larger geometries than a pipe, alternative approaches to flow regime modelling were considered in the literature, based on the drag force modelling by Ishii. For the pool flow, the suitable pressure drop modelling for the middle void fraction ranges (between 0.3 and 0.7) becomes more important. The transition flow approaches for this middle void range by Meignen et al. [48] and by Vujic [61] introduce a transition flow region where bubbly and droplet flow co-exist. Although these models introduce simplifications while moving away from the pipe specific flow patterns and characteristic lengths, they represent the pool flow better.

Similar to the drag force modelling by Ishii, both of these models assume a bubbly flow regime for void fraction value of 0.3 and below, and a droplet flow regime for void fraction value of 0.7 and above. As mentioned, for the void fraction values in between, the models by Meignen et al. and by Vujic assume a transition region where bubbly flow and droplet flow regimes co-exist, see Figure 5.5.

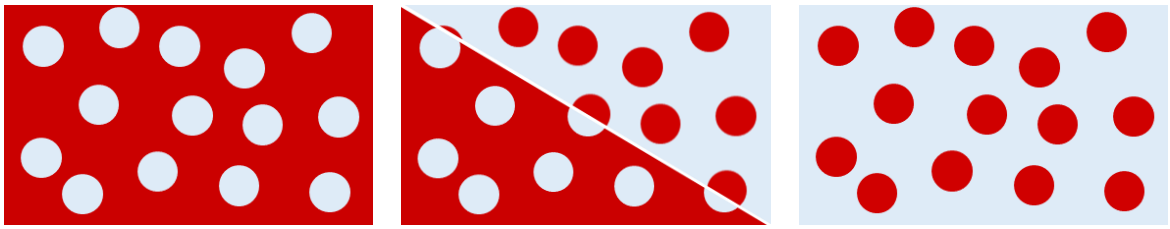

Bubbly Flow $\alpha \leq 0.3$ | *Transition Flow* $0.3 < \alpha < 0.7$ | *Droplet Flow* $0.7 \leq \alpha$

Figure 5.5 Different flow regimes of two-phase flow and flow regime criteria according to drag force modelling by Meignen et al. and by Vujic with transition flow.

In the model by Meignen et al., as in drag force modelling by Ishii, the velocity of the gas phase is assumed to be the same in every flow region independently if the gas phase is dispersed or continuous.

On the other hand, in the model by Vujic, the gas phase is assumed to have different velocities in dispersed and in continuous form. More precisely, the model by Vujic assumes that the continuous gas flow around the droplets has a higher flow rate than that of bubbles.

Both models calculate the drag force between the phases for bubbly and droplet flow regions the same way it is calculated by Ishii as described in Chapter 5.2.2. For the transition region where the void fraction is between 0.3 and 0.7, the drag force is calculated by weighing the drag forces for bubbly and droplet regimes.

- **Drag force for transition flow, $0.3 < \alpha < 0.7$ by Meignen et al. [48]:**

For the void fraction value α that is between 0.3 and 0.7, the drag force, $F_{mst,tr}$ is calculated by Meignen et al. as follows:

$$F_{mst,tr} = F_{mst,bb}(\alpha = 0.3) * Z_{bb} + F_{mg,dt}(\alpha = 0.7) * Z_{dt} \tag{5.29}$$

Where $F_{mst,bb}(\alpha = 0.3)$ is the drag force for the bubbly flow regime at void fraction value 0.3 and $F_{mst,dt}(\alpha = 0.7)$ is the drag force for the droplet flow regime at void fraction value 0.7. Both of these values are calculated according to the modelling by Ishii as described in Chapter 5.2.2. Z_{bb} and Z_{dt} are weighing coefficients that indicates the fraction

of bubbly flow and the fraction of droplet flow in the transition regime respectively. For the total void fraction of the flow, α, these coefficients are calculated as follows:

$$Z_{bb} = \frac{0.7 - \alpha}{0.7 - 0.3} \tag{5.30}$$

$$Z_{dt} = \frac{\alpha - 0.3}{0.7 - 0.3} \tag{5.31}$$

- **Drag force for transition flow, $0.3 < \alpha < 0.7$ by Vujic** [61]**:**

For the void fraction value α that is between 0.3 and 0.7, the drag force, $F_{mst,tr}$ is calculated by Vujic as follows:

$$\begin{aligned} &F_{mst,tr} \\ &= \Bigg(F_{mst,bb}(\alpha = 0.3) Z_{bb} \\ &+ F_{mst,dt}(\alpha = 0.7) Z_{dt} \frac{0.7 F_{mst,bb}(\alpha = 0.3)}{0.3 F_{mst,dt}(\alpha = 0.7)} \Bigg) \left(\frac{\alpha}{0.3 Z_{bb} + 0.7 Z_{dt} \sqrt{\frac{0.7 F_{mst,bb}(\alpha = 0.3)}{0.3 F_{mst,dt}(\alpha = 0.7)}}} \right)^2 \end{aligned} \tag{5.32}$$

As mentioned earlier, the modelling approach by Vujic considers two different velocity values for bubbles and gas in continuous form. For the pool flow where initial average velocity for the liquid phase is zero ($v_l = 0$), the relative velocity for bubbly flow region $v_{r,bb}$ and the relative velocity for droplet flow region, $v_{r,dt}$ are calculated based on the average relative velocity, v_r, as follows:

$$v_{r,bb} = \frac{\alpha}{0.3 Z_{bb} + 0.7 Z_{dt} \sqrt{\frac{0.7 F_{mst,bb}(\alpha = 0.3)}{0.3 F_{mst,dt}(\alpha = 0.7)}}} v_r \tag{5.33}$$

$$v_{r,dt} = \frac{\alpha}{0.3 Z_{bb} + 0.7 Z_{dt} \sqrt{\frac{0.7 F_{mst,bb}(\alpha = 0.3)}{0.3 F_{mst,dt}(\alpha = 0.7)}}} \sqrt{\frac{0.7 F_{mst,bb}(\alpha = 0.3)}{0.3 F_{mst,dt}(\alpha = 0.7)}} v_r \tag{5.34}$$

With the stand-alone simulation program, the two-phase interfacial drag force models discussed in this section were solved for melt and steam properties with similar method to solving Classic Ishii Drag model discussed in Chapter 5.2.2. The void fraction results according to modelling by Meignen et al. and modelling by Vujic can be seen Figure 5.6.

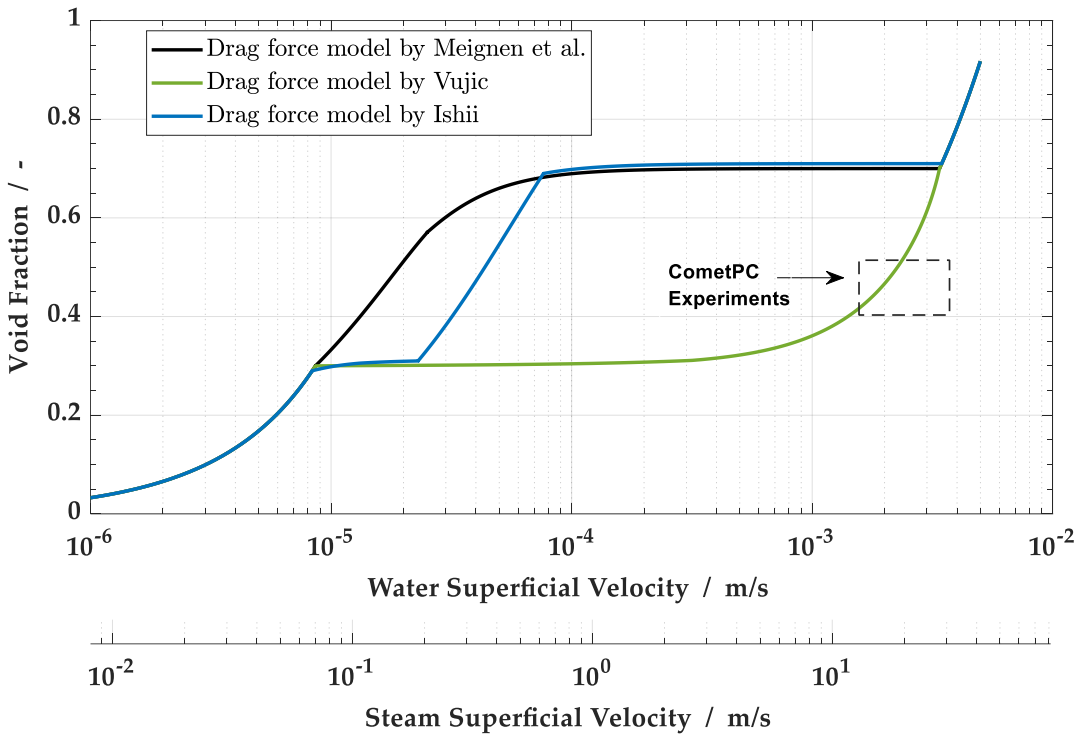

Figure 5.6 Relation between the void fraction in the melt pool and superficial velocity of cooling water (and steam) according to drag force models by Meignen et al., by Vujic and by Ishii. The cooling water flow rate values and final porosities observed in CometPC experiments are indicated on the diagram with a rectangular region within dashed lines.

As all these three models assume the same drag force relation for the bubbly flow region the void fraction curve of all these models overlap up to 0.3 void fraction which occurs for water superficial value of $8x10^{-6}$ m/s which corresponds to approximately 0.065 m/s steam superficial velocity. For the middle flow region between $8x10^{-6}$ m/s and $3.5x10^{-3}$ m/s water superficial velocity the difference in the resulting void fraction can be observed for each model.

For the model by Ishii, the three different flow patterns are clearly visible which have the transition at 0.3 void fraction and again at 0.7 void fraction. The void stays almost constant shortly while transitioning to the churn flow, however the void fraction increases relatively quickly up to 0.7 void fraction. During transition from churn to droplet flow the void fraction again proceeds almost constant for certain range of superficial steam or water velocity due to the fact that the increasing steam flux no longer forms bubbles to be dragged down but continues to flows around drops and the liquid droplets are forming that are dragged down by the steam and this force defines the friction.

For the model by Meignen et al., it can be seen that the void fraction increases very quickly for the much smaller steam superficial velocity values compared to the model by Ishii. And as it can be seen in Figure 5.6, similar to the model by Ishii, the model by Meignen et al. also highly overestimates the final void/porosity values observed in

CometPC experiments for the superficial water velocity values reached in these experiments.

The assumption of bubbles and steam in continuous form having different velocities in modelling approach by Vujic brings the drastic difference in friction force calculation for the middle flow regions compared to models by Ishii and by Meignen et al. According to this modelling assumption, during bottom flooding, when the steam is in continuous form it rises and escapes the compact liquid melt much faster than the bubbles. As soon as a steam in continuous form exists, meaning for void fraction higher than 0.3, the steam that does not fit into the bubbly regime escapes the liquid rather fast. This is why in Figure 5.6, the curve for the model by Vujic stays almost constant over a broad range in the beginning of the middle section.

At a certain superficial velocity, the entire flow enters a droplet flow regime, for which the friction is calculated the same way for all three models. Therefore, the curves overlap after void fraction of 0.7. However, this void value and the assumption of a droplet flow is adjusted for two-phase flow of water and steam and cannot be representative for the two-phase flow of a heavy fluid and steam. Therefore, although the results with the model by Vujic approaches to the final void/porosity values observed in CometPC experiments, the flow pattern is not representative of the flow patterns that have been observed in bottom cooling experiments.

5.3 Development of the New Interfacial Friction Model for Corium-Steam Two-phase Flow

5.3.1 Description of the Model

The investigations so far in Chapter 5.2 with the existing two-phase flow interfacial friction models from the literature have shown that a new interfacial friction model for the two-phase flow of molten corium and steam is needed for the modelling approach to porosity build-up phenomenon during bottom-cooling that is taken in this work.

The primary points considered in the new model:

- The flow patterns of the two-phase flow should represent the bottom-cooling phenomenon. The morphology of post-test cross sections of the solidified melt from COMET and CometPC experiments indicate that channels are formed during cooling and porosities exist around these channels. In the new model, a two-phase flow regime where bubbles and channels co-exist is introduced. The continuous stream flow is assumed to be in form of channels where the shear force between steam channel and melt film around it is the determining interfacial friction force for void. Drag on the possible melt droplets in these channels is neglected.

- The fast escape of the hot steam from the heavy compact molten material should be represented. Based on the observations and outcome of COMET and CometPC experiments, due to very high steam flow rates during bottom cooling it is assumed that is part of the steam progresses in the melt through preferred paths with less resistance (channels, as seen in the post-test cross-sections of solidified melt) where it would be leaving the melt with higher velocity, compared to bubbles. The new model assumes two different velocity fields for the steam: in the channels the steam has higher velocity than that of bubbles.

- The new model should be suitable for implementation into various multi-phase simulation codes. The final aim of the model development is to improve the capability of complex multi-phase simulation codes for severe accident simulations. Some of these codes have only a single velocity field defined for the gas phase. In addition to defining the models with separate velocities and separate friction forces for steam in different flow regimes, the average velocity and friction factor for steam are also modelled based on the averaging approach by Vujic [61], for implementation into single momentum equation for gas phase while preserving the effect of separate velocity fields.

With these considerations a new two-phase flow interfacial friction force model was developed in this work in order to model the porosity formation during corium cooling by bottom flooding.

Figure 5.7 shows the flow regimes defined for the new interfacial friction force.

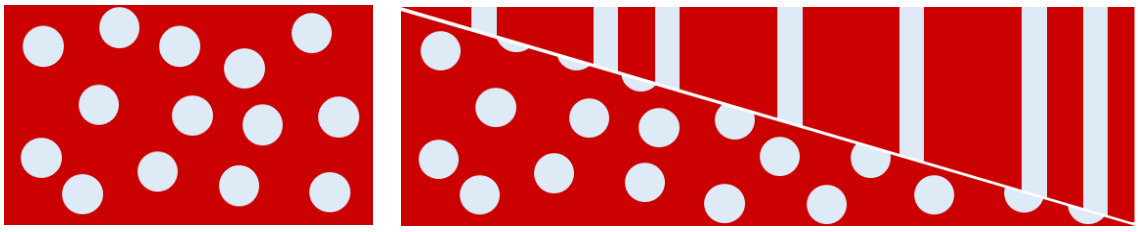

Bubbly Flow
$\alpha \leq 0.3$

Bubbly-Channel Flow
$0.3 < \alpha$

Figure 5.7 Different flow regimes of two-phase flow and flow regime criteria according to new Bubbly-Channel drag force modelling.

As can be seen on Figure 5.7, for void fraction value of 0.3 and smaller the two-phase flow of melt and steam was assumed to be in bubbly flow regime. For void fraction values higher than 0.3, the flow regime was assumed to consist of bubbles and channels.

- **Friction force for bubbly flow, $\alpha \leq 0.3$:**

For bubbly flow region in this model, the same approach is followed as the drag force for bubbly flow region in model by Ishii. Therefore, the equations from Equation (5.11) to Equation (5.16) apply here the same way described in Chapter 5.2.2.

- **Friction force for bubbly-channel flow, $\alpha > 0.3$:**

When the total steam volume fraction (or void fraction), α, exceeds the limit for bubbly flow, it is assumed that the excess void forms continuous channels. In this case the bubbles and channels are in co-existence and the volume fraction of the steam that is in the form of channels is calculated as follows:

$$\alpha_{ch} = \alpha - \alpha_{bb} \tag{5.35}$$

Where, α_{ch} is the steam volume fraction that is in form of continuous channels (or channel void) and α_{bb} is the gas volume fraction that is in form of bubbles (or bubble void), which is taken constant as 0.3.

The new model with channels also assumes that the velocity of the gas in channels (and hence the relative velocity) will be significantly larger than that of bubbles. This assumption requires separate interfacial friction force equation for bubbly flow region and channel flow region, with different relative velocities in quadratic form:

$$F_{mst,bb} = K_{mst,bb} {v_{r,bb}}^2 \tag{5.36}$$

$$F_{mst,ch} = K_{mst,ch} {v_{r,ch}}^2 \tag{5.37}$$

Where $F_{mst,bb}$ is the interfacial friction force for the bubbly regime, $F_{mst,ch}$ is the interfacial friction force for the channel flow regime, $K_{mst,bb}$ is the interfacial friction factor for the bubbly regime, $K_{mst,ch}$ is the interfacial friction factor for channel flow regime, $v_{r,bb}$ is the relative velocity in bubbly regime and $v_{r,ch}$ is the relative velocity in channel flow regime.

The friction factors $K_{mst,bb}$ and $K_{mst,ch}$ are calculated based on the drag coefficient by Ishii for bubbly phase and annular flow shear friction model by Ishii [45] for α_{bb} and α_{ch}.respectively.

As Equation (5.35) indicates, the void fraction for bubbles, α_{bb}, in the bubbly-channel flow region the is 0.3. Therefore, analog to the Equation (2.30), the friction factor $K_{mst,bb}$ can be expressed as follows:

$$K_{mst,bb} = -\frac{3}{8}\frac{0.3}{r_{bb}} C_{D,bb}\rho_m \tag{5.38}$$

Where ρ_m is the density of the melt, r_{bb} is the radius of the steam bubbles (see Equation (2.14)), $C_{D,bb}$ is the drag coefficient for the bubbly flow (see Equation (5.12) and (5.13)).

For the shear stress between continuous steam and the channel wall that is the continuous melt field, Ishii's model for annular flow shear force [45] is adapted. According to this the shear force between melt and steam per volume is as follows:

$$F_{mst,ch} = -2\frac{\alpha_{ch}}{r_{ch}} f_{mst}\rho_{st}|v_{r,ch}|v_{r,ch} \tag{5.39}$$

Where ρ_m is the density of the steam, f_{mst} is the interfacial friction coefficient and r_{ch} is the radius of channels.

In this case the friction factor for channel flow, $K_{mst,ch}$ is expressed as follows:

$$K_{mst,ch} = -2\frac{\alpha_{ch}}{r_{ch}} f_{mst}\rho_{st} \tag{5.40}$$

The interfacial friction coefficient f_{mst} is given by Wallis for rough wavy films as follows [45]:

$$f_{mst} = 0.005[1 + 75(1 - \alpha_{ch})] \tag{5.41}$$

And finally, the radius for channels are modelled in a similar way to bubble radius, but assumed to be larger [45]:

$$r_{ch} = 10\sqrt{\frac{\sigma_m}{g(\rho_m - \rho_{st})}} \tag{5.42}$$

The current two-phase flow modelling in COCOMO3D, and two-phase modellings in some other multi-phase simulation codes consider only a single average velocity of gas phase. That means the sum effect of both flow regimes with their separate friction forces and gas velocities have to be expressed in terms of single velocity field. This can be expressed analog to the friction equations presented in Chapter 2.3.2:

$$F_{mst} = K_{mst}{v_r}^2 \tag{5.43}$$

Where F_{mst} is the total interfacial friction force of the two-phase flow with bubble and channel regime, K_{mst} is the average interfacial friction factor and v_r is the average relative velocity.

The average steam velocity can be defined in terms of steam velocities in bubbly and channel flow regime as follows:

$$v_{st} = \frac{\alpha_{bb} v_{g,bb} + \alpha_{ch} v_{g,ch}}{\alpha} \tag{5.44}$$

Where v_g is the average gas velocity, $v_{g,bb}$ is the gas velocity in bubbly flow region and $v_{g,ch}$ is the gas velocity in channel flow region. Considering that both, bubbly regime steam velocity and channel flow steam velocity, would be significantly larger than the velocity of liquid corium, the liquid velocity in both bubbly and channel regime can be assumed approximately same:

$$v_l = v_{l,b} = v_{l,ch} \tag{5.45}$$

Where v_l is the average liquid velocity, $v_{l,bb}$ is the liquid velocity for bubbly regime and $v_{l,ch}$is the liquid velocity for the channel flow regime. If v_l is subtracted from both sides of the Equation (5.44):

$$v_g - v_l = \frac{\alpha_{bb} v_{g,bb} + \alpha_{ch} v_{g,ch}}{\alpha} - \frac{\alpha}{\alpha} v_l \tag{5.46}$$

And Equation (5.46) rearranged for Equation (5.35) and (5.44), the average relative velocity v_r can be expressed by the relative velocities of the respective regimes as follows:

$$v_r = \frac{\alpha_{bb} v_{r,bb} + \alpha_{ch} v_{r,ch}}{\alpha} \tag{5.47}$$

In order to come to an average expression for the interfacial friction factor, simplified momentum equations for the two flow regions are considered separately:

$$-K_{mst,bb} {v_{r,bb}}^2 = \alpha_{bb} \frac{dp}{dz} + \alpha_{bb} \rho_{st} g \tag{5.48}$$

$$-K_{mst,ch} {v_{r,ch}}^2 = \alpha_{ch} \frac{dp}{dz} + \alpha_{ch} \rho_{st} g \tag{5.49}$$

For uniform density of steam, it can be assumed that the gravitational force $\rho_{st}g$ is uniform in the. The pressure gradient $\frac{dp}{dz}$ for both regions is assumed uniform in radial direction as well. Under these assumptions Equations (5.48) and (5.49) can be rearranged as follows:

$$\alpha_{ch}K_{mst,bb}{v_{r,bb}}^2 = \alpha_{bb}K_{mst,ch}{v_{r,ch}}^2 \tag{5.50}$$

A ratio between relative velocities can be obtained as follows:

$$\frac{v_{r,bb}}{v_{r,ch}} = \sqrt{\frac{\alpha_{bb}K_{mst,ch}}{\alpha_{ch}K_{mst,b}}} = q \tag{5.51}$$

Relative velocity for each region can be expressed for the ratio q and eachother as follows:

$$v_{r,bb} = qv_{r,ch} \tag{5.52}$$

$$v_{r,ch} = \frac{v_{r,bb}}{q} \tag{5.53}$$

The Equations (5.52) and (5.53) are substituted in Equation (5.47) so it would be possible to express the average velocity v_r in terms of separate relative velocities $v_{r,bb}$ and $v_{r,ch}$:

$$\alpha v_r = \alpha_{bb}v_{r,bb} + \alpha_{ch}\frac{v_{r,bb}}{q} \tag{5.54}$$

$$\alpha v_r = v_{r,bb}\left(\alpha_{bb} + \frac{\alpha_{ch}}{q}\right) \tag{5.55}$$

$$v_{r,bb} = \frac{\alpha}{\alpha_{bb} + \frac{\alpha_{ch}}{q}}v_r \tag{5.56}$$

and

$$\alpha v_r = \alpha_{bb}v_{r,ch}q + \alpha_{ch}v_{r,ch} \tag{5.57}$$

$$\alpha v_r = (\alpha_{bb}q + \alpha_{ch})v_{r,ch} \tag{5.58}$$

$$v_{r,ch} = \frac{\alpha}{\alpha_{bb} q + \alpha_{ch}} v_r \tag{5.59}$$

The total friction force for the gas phase is the sum of friction forces for each flow region:

$$F_{mst} = K_{mst} v_r^2 = K_{mst,bb} v_{r,bb}^2 + K_{mst,ch} v_{r,ch}^2 \tag{5.60}$$

Inserting Equations (5.56) and (5.59) into Equation (5.60) gives:

$$K_{mst} v_r^2 = K_{mst,bb} \left(\frac{\alpha}{\alpha_{bb} + \frac{\alpha_{ch}}{q}} \right)^2 v_r^2 + K_{mst,ch} \left(\frac{\alpha}{q\alpha_{bb} + \alpha_{g,ch}} \right)^2 v_r^2 \tag{5.61}$$

Thus, the average friction factor can be expresses as:

$$K_{mst} = K_{mst,bb} \left(\frac{\alpha}{\alpha_{bb} + \frac{\alpha_{ch}}{q}} \right)^2 + K_{mst,ch} \left(\frac{\alpha}{q\alpha_{bb} + \alpha_{ch}} \right)^2 \tag{5.62}$$

5.3.2 Comparison of the new Bubbly-Channel Model Against Other Models and Validation against CometPC Experiments

Prior to implementing the new Bubbly-Channel Model into COCOMO3D code, the friction relation is simulated by the stand-alone simulation code. The Equation (5.28) is solved for the void, α, iteratively as explained in Chapter 5.2.1 with the friction forces of the New Bubbly-Channel Model from Chapter 5.3.1. The material properties of melt and steam, and a mass flux value for cooling water are defined in the stand-alone program as input. A range between 0 and 1 is defined for void fraction and an initial value was set to start the iteration. The superficial velocities of water, j_w, and steam, j_{st}, are calculated by Equations (5.6) and (5.7) respectively as explained in Chapter 5.2.1. Water properties were taken for water at 303 K and 1.2 bar. To realize the pool flow conditions, the initial average mass flux and velocity of the melt pool was set to zero. For the known void fraction, the real velocities of steam, v_s, and melt, v_m, during two phase flow are calculated respectively by Equations (5.8) and (5.9).

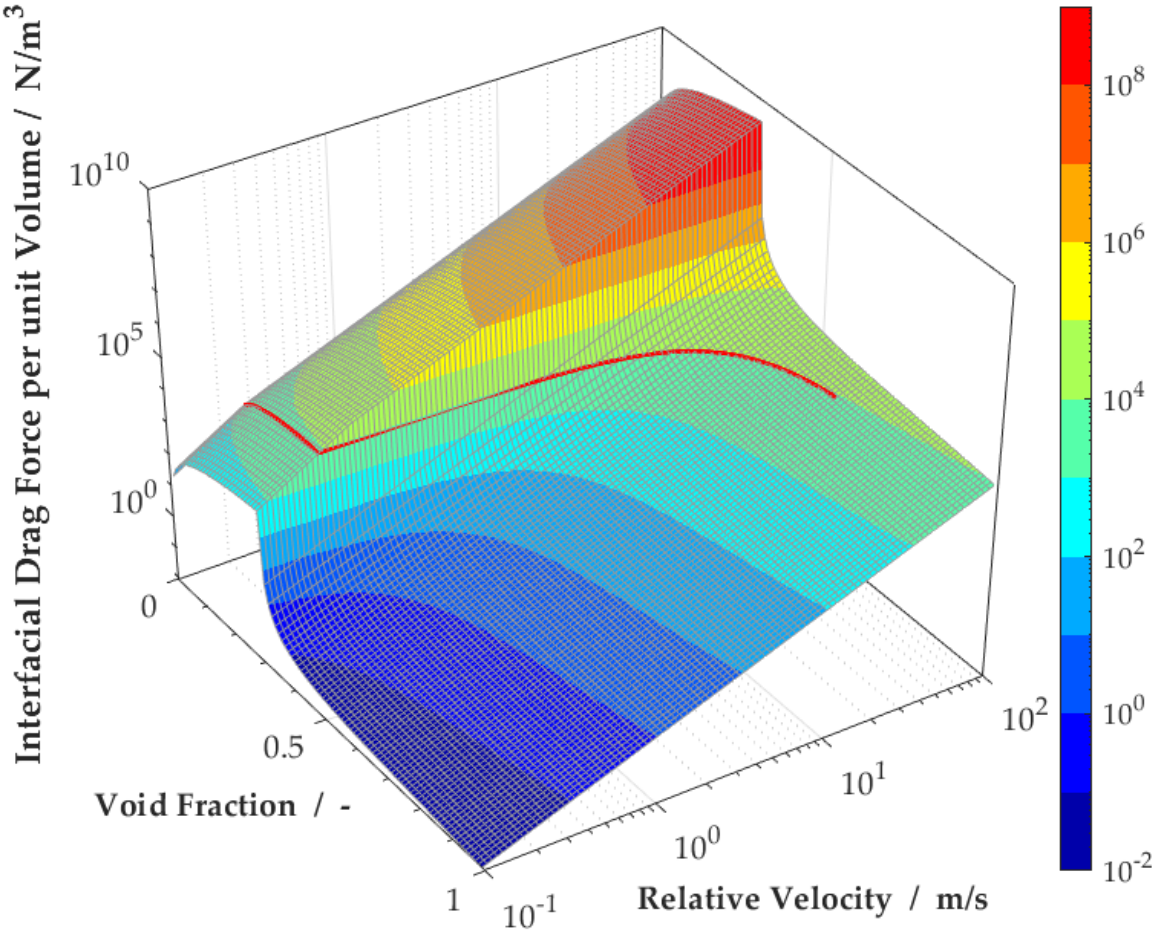

Figure 5.8 Relation between Void - Relative velocity – Interfacial Friction Force according to new Bubbly-Channel Modelling. The values where Simplified Momentum Equation for Melt-Steam Two-Phase flow has solution marked with red line.

Figure 5.8 shows the relation between void fraction, average relative velocity and the interfacial friction force according to new Bubbly-Channel Flow Model. The red line on the dependence plane indicate the values where Equation (5.28) has a solution. It can be seen from the Figure 5.8 that the new model gives higher friction forces in lower void regions where the slow steam bubbles are dragged back. In the higher void regions where channels exist, the interfacial friction force is low due to the modelling of channels and the steam escapes the melt easier. At any void value, higher relative velocities give higher friction forces.

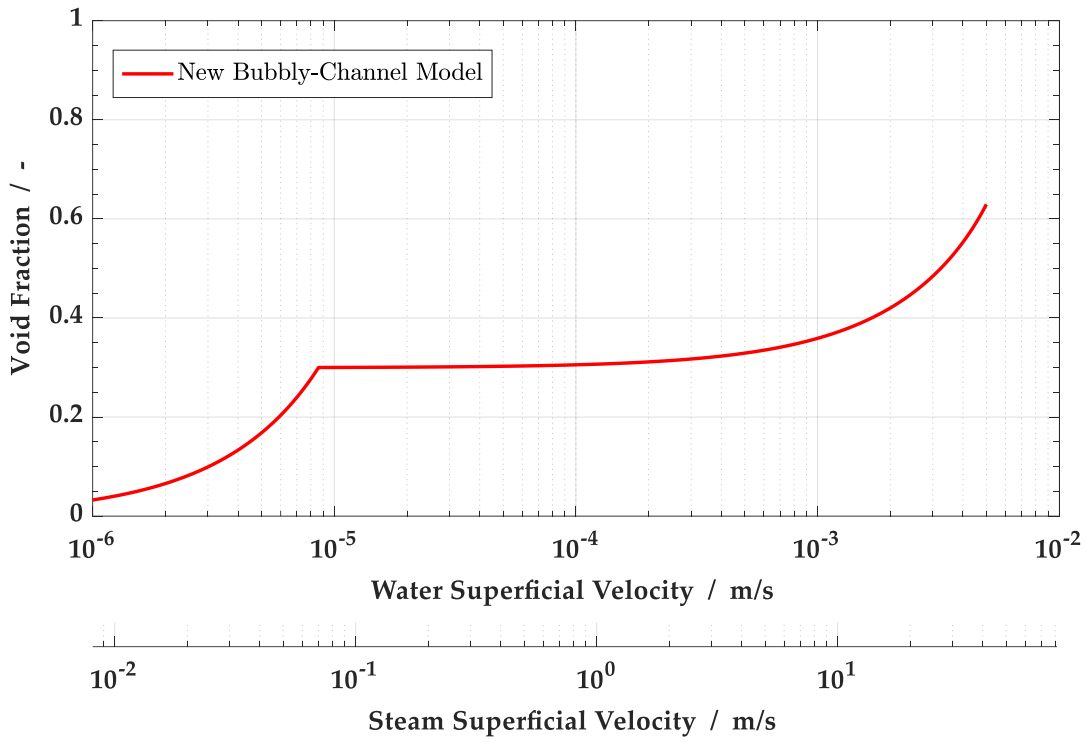

Figure 5.9 Relation between the void fraction in the melt pool and superficial velocity of cooling water (and steam) according to new Bubbly-Channel flow model.

Figure 5.9 shows the relation between the cooling water superficial velocity and void fraction in the melt pool according to new Bubbly-Channel two-phase flow modelling. Figure 5.10 shows the relation between void fraction in melt layer and superficial velocity of cooling water according to new Bubbly-Channel Model in comparison with other models discussed in this work for melt and steam properties and bottom-cooling boundary conditions. As the bubbly flow region is modeled in the same way in all of these models, the void fraction results up the superficial water velocity of approximately $8x10^{-6}$ m/s overlaps on the diagram. As it can be seen in Figure 5.9 and Figure 5.10 in the new bubbly-channel model, the void fraction stays almost constant for a very long time after the bubbly flow limit. The reason for this trend is that, as the mass flux of steam increases, the steam amount that does not fit into the bubble limit anymore leaves the melt with a much higher speed. As opposed to the other models, there is no flow regime transition criterion defined for the gas continuous flow in the new model. As a result of this, the void fraction starts to increase with much higher steam fluxes as the channels increase and sheer forces between many channels and surrounding melt becomes dominating and raise the melt upwards, which is physically better representation of the phenomenon. Moreover, as it can be seen in the Figure 5.10 the new Bubbly-Channel Model represents the average of CometPC experiment results very well.

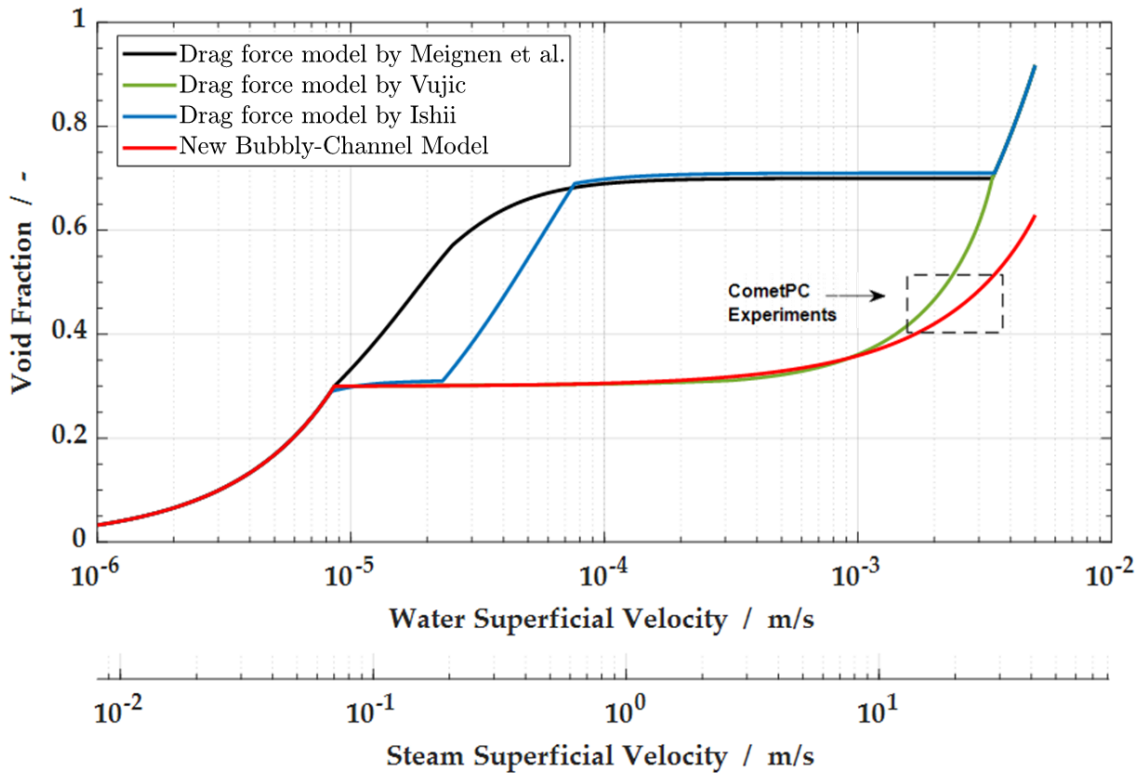

Figure 5.10 Relation between the void fraction and superficial velocity according to new Bubbly-Channel flow model in comparison with other two-phase flow friction models discussed in this work. The cooling water flow rate values and final porosities observed in CometPC experiments are indicated on the diagram with a rectangular region within dashed lines.

Depending on the accident scenario, the real corium in the reactor might have a higher density than the thermite mix used in CometPC experiments. Therefore, a set of stand-alone simulations are performed by varying the density of melt, in order to see its effect on the void fraction with the new model. As it can be seen on the Figure 5.11, for the stand-alone simulation with the new friction model, the melt density has rather insignificant effect on the void fraction.

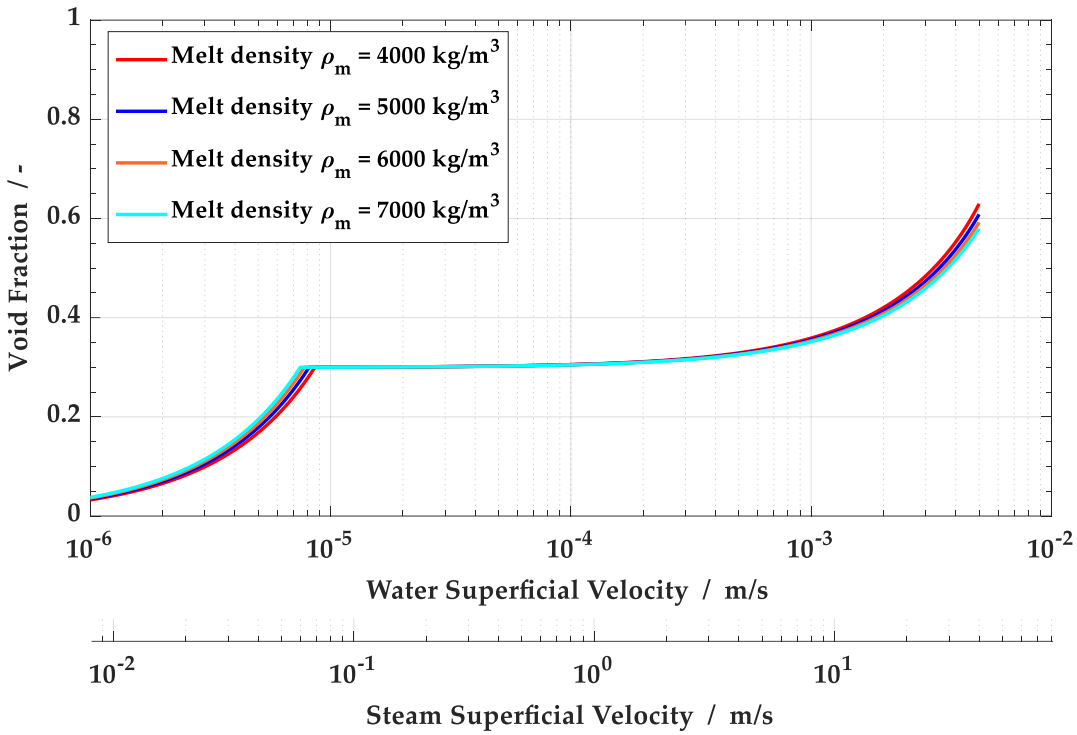

Figure 5.11 Effect of the melt/corium density on the void fraction for the new bubbly-channel flow friction model.

The new friction model provides successfully results as a stand-alone simulation with steam and melt material properties, and is able to represent the porosity values observed in CometPC and COMET research. As a next step, this friction model is implemented to COCOMO3D code in order to simulate the two-phase flow of steam and melt.

5.4 Two-Phase Flow Simulations with the new Bubbly-Channel Model

The new Bubbly-Channel interfacial friction force model was implemented into COCOMO3D code in order to simulate the two-phase flow of steam and melt for bottom flooding. Besides implementing the friction model, the material properties of corium in liquid phase are introduced into the code as they have not been defined in COCOMO3D prior to this work. Since the new model is for the two-phase flow of steam and molten corium, the simulations presented in this chapter show the steam and molten pool interaction. The simulation domain is set in cylindrical coordinates as shown in Figure 5.12, and the pool height and steam inlet geometry were assumed symmetrical in tangential direction around z-axis. This way, the extreme simulation times for the fluid domain could be reduced.

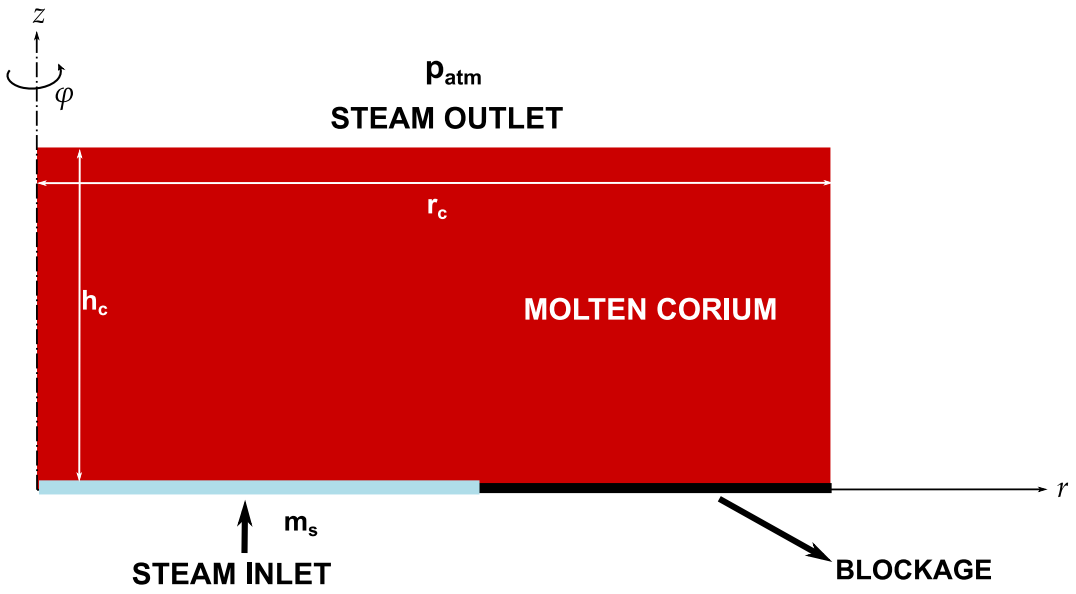

Figure 5.12 COCOMO3D Simulation Domain for the two-phase flow simulation of steam and melt pool.

As it was introduced in Chapter 2.3, the conservation equations for mass, energy and momentum already exist in COCOMO3D. However, as the two-phase flow of melt and steam consists of two different material fluids and not the different phases of the same material, the evaporation-condensation and material transfer between the phases are disabled in the code for these simulations.

As seen on the Figure 5.12, at the inlet, steam mass flux is defined as a boundary condition. The steam mass flux is slowly increased to the full mass flux that is observed when the entire cooling water is evaporated. And at the outlet atmospheric pressure is defined as boundary condition. The blockage seen on the Figure 5.12 is the sacrificial concrete layer between the porous concrete core catcher and melt. During simulations the sacrificial concrete can be assumed completely ablated or partially ablated. Depending on this assumption the blockage shown below the melt pool is altered.

The viscosity terms are neglected in the momentum conservation equations in COCOMO3D. Meaning, except the fluid interface and solid interface the individual fluids on their own are frictionless in their flow. Therefore, the pressure losses that might happen due to fluid nature of molten corium are not reflected in the simulation results. The focus of the simulations is void fraction in the melt layer caused by the steam flow into the melt.

5.4.1 Simulation of CometPC Plus Experiment

The first COCOMO3D simulation that is shown in this section is the simulation of the coolant-molten thermite layer flow from the CometPC Plus experiment. In order to do so the geometry of the thermite melt layer from the experiment is defined as an input. The height of the melt layer, h_c, is 0.5 meter and the radius of the cavity, h_c where the melt was poured is 0.46 meter. The total height of the simulation domain is defined high enough in order to not restrict the upward movement of the melt. The temperature of the melt is given as it was stated in the experiment as 2200 K and as the coolant is assumed completely evaporated the temperature of the steam is assumed to be the same as well. The material properties of melt are taken from the Table 5.2. As the amount of partial opening, meaning the part that sacrificial concrete that was ablated is not clear, it is defined as 50% and in the center of the contact surface. The volume flow rate of the coolant is given as an inlet boundary condition in terms of mass flux in the simulation. The mass flow rate is increased gradually to the maximum amount and kept constant. As the simulation of two-phase flow has a great simulation load and takes very long time periods, the simulation time is restricted to 7 seconds. Which allows simulations to have enough time steps to reach the constant coolant (steam flow rates) in a stable manner and can show the flow pattern under constant flow rate for the defined boundary condition.

Figure 5.13 shows the simulation results of two-phase flow of steam and melt for CometPC Plus experiment at progressive simulation times. The legend and the color scale show the ratio of the liquid volume to total volume in cells. The cells that have only melt in volume (void fraction α=0.0) are shown in dark red and the cells that have only steam in volume (void fraction α=1.0) are shown in dark blue. As the sacrificial concrete at the bottom is assumed partially open in this simulation, it can be clearly seen in the simulation the steam ingression from the one side while part of the lower layer of the melt is still mostly liquid. As the simulation progresses the voids within the melt layer can be seen, which represents the post-test morphology quiet well.

The later time frames of the simulation in Figure 5.13 show liquid volume separated from the melt bulk sustained in the steam room above the liquid. Which is a good representation of the melt dispersion/ejection phenomenon that is known to occur during bottom cooling. As discussed in this work earlier, the violent interaction between melt and steam is observed during bottom cooling. And due to this strong interaction, the flow is unsteady despite the constant flow rates. This unsteady flow is also represented well with the simulations. It is still noticeable that certain areas stay with high liquid fraction (red) where other areas have large voids (blue), which represents the outcome of the COMET research. On the other hand, this pattern is spread enough to enable sufficient cooling for the not fragmented regions.

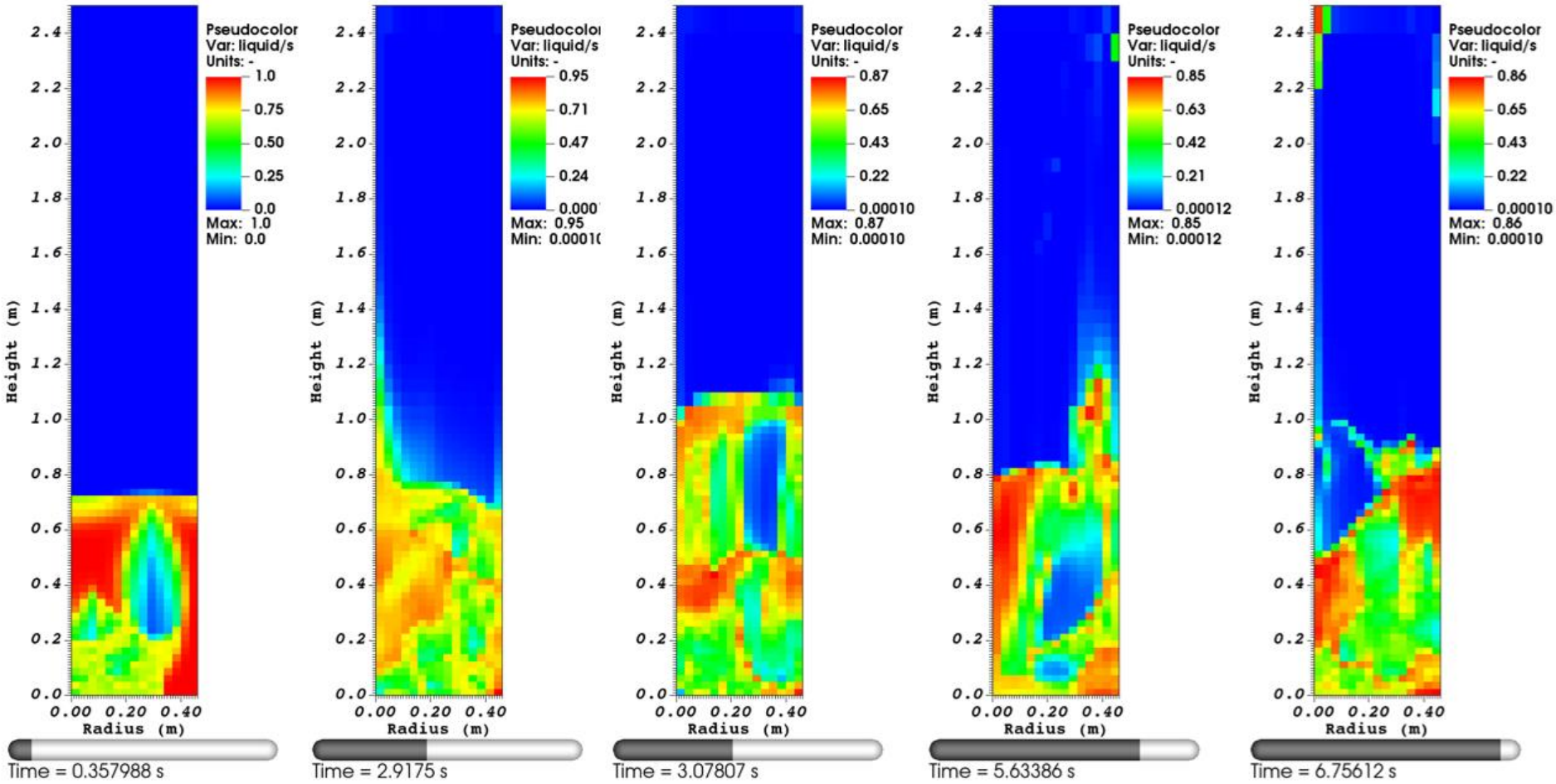

Figure 5.13 Two-Phase flow simulation of molten thermite and steam from CometPC Plus experiment with new Bubbly-Channel interfacial friction law. Legend: Volume ratio of melt

As the flow pattern fluctuates during simulations, it might be difficult to observe the average void value just by looking at the simulation progress. In order to present a better quantification of the average void fraction of the melt pool, the change of the surface level of the melt pool during the two-phase simulation is determined by a separate simulation program. This post-process evaluation determines the position of the mesh boundary in axial direction that has a certain fraction of liquid phase below it for each time step of the simulation.

Figure 5.14 shows the result of this evaluation for the two-phase flow simulation of melt and steam for the CometPC Plus experiment. The red line shows the position of the mesh border on the axial axis (height) where 99% of the total melt volume is below. The yellow line shows the position of the mesh border where 95% of the melt is below. And the blue line on the figure indicates the position of the mesh border where 90% of the liquid volume in the domain is to be found underneath. For example: at around 5.3 seconds of the simulation time, 90% of the melt is below 1.5-meter height in the simulation domain and 99% of the melt volume is below the 2.3-meter height. As it can be noticed, the red and yellow lines also show the ejected particles from the bulk, whereas the blue line represents the bulk surface. This evaluation gives the idea about the steam fraction takes space in the melt. Compared to the original melt height of 0.5 meter it can be concluded that the average void fraction is around 0.45-0.50.

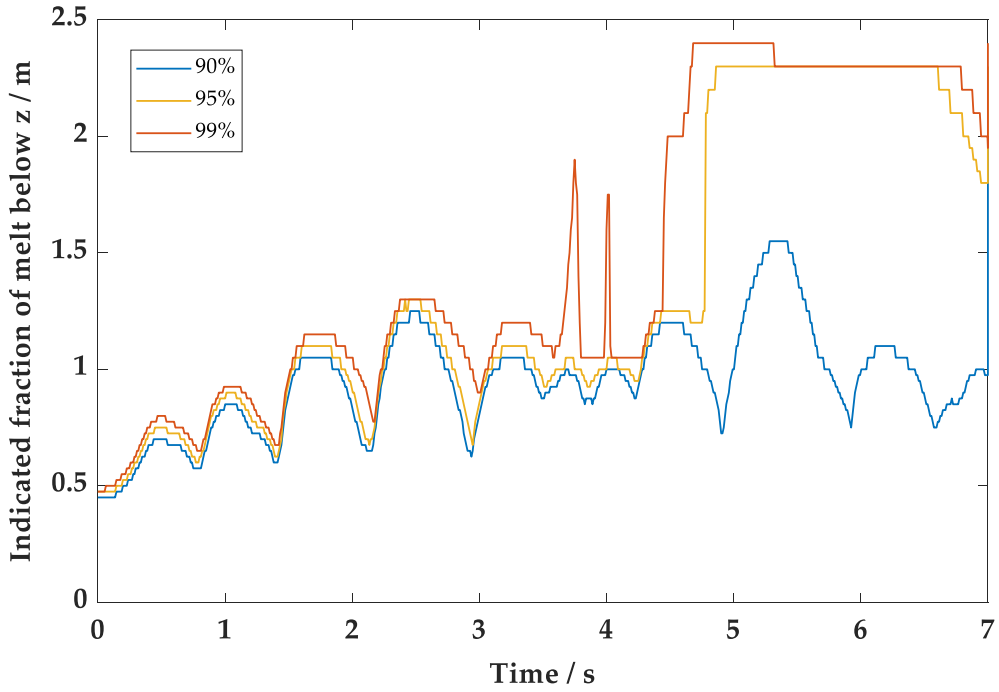

Figure 5.14 Average level of the molten thermite layer as a result of steam ingression from below and two-phase flow for CometPC Plus experiment simulation.

5.4.2 Simulation of Reactor Case

Simulations in this section are performed for a case that might happen during a real accident scenario and different than CometPC experiment boundary conditions.

The height of the molten corium pool to be cooled, h_c, is defined again as 0.5 meter. As the real reactor cavity diameter introduces extremely long simulation times, the diameter is kept the same as the one of CometPC experiments. For the reactor case simulations, the density of the corium is given as 6000 kg/m^3 and the mass flow rate of the coolant is calculated based on 0.0015 m/s superficial velocity of water, which yields to 0.94 kg/s steam mass flow rate. The temperature for the corium is given as 2500 K which is more realistic for the reactor case and the temperature difference between steam and molten corium during two-phase flow is neglected as the corium temperature is expected to dominate. Since there are still uncertainties about the partial opening of the sacrificial concrete one simulation is performed with the assumption of 50% ablated sacrificial concrete and one simulation is performed with completely ablated sacrificial concrete.

Figure 5.15 shows the simulation results for the case where sacrificial concrete is partially ablated. The initial ingression pattern looks identical to the one of CometPC Plus simulations. In the later simulation time points it can be seen that the pattern fluctuations do happen, however the ejection starts earlier. The large voids occur for this simulation case as well, and they seem to be larger than that of CometPC Plus simulation case, which might be the effect of the increased density. This might yield to more compact corium regions. Figure 5.16 shows the post processing evaluation of the simulation result. The red line increasing up to 2.4-meter point around 3 second mark indicates the early occurring of the ejection. Although the average void comes around to 0.5, the surface of the bulk melt in this simulation seems to be more fluctuating.

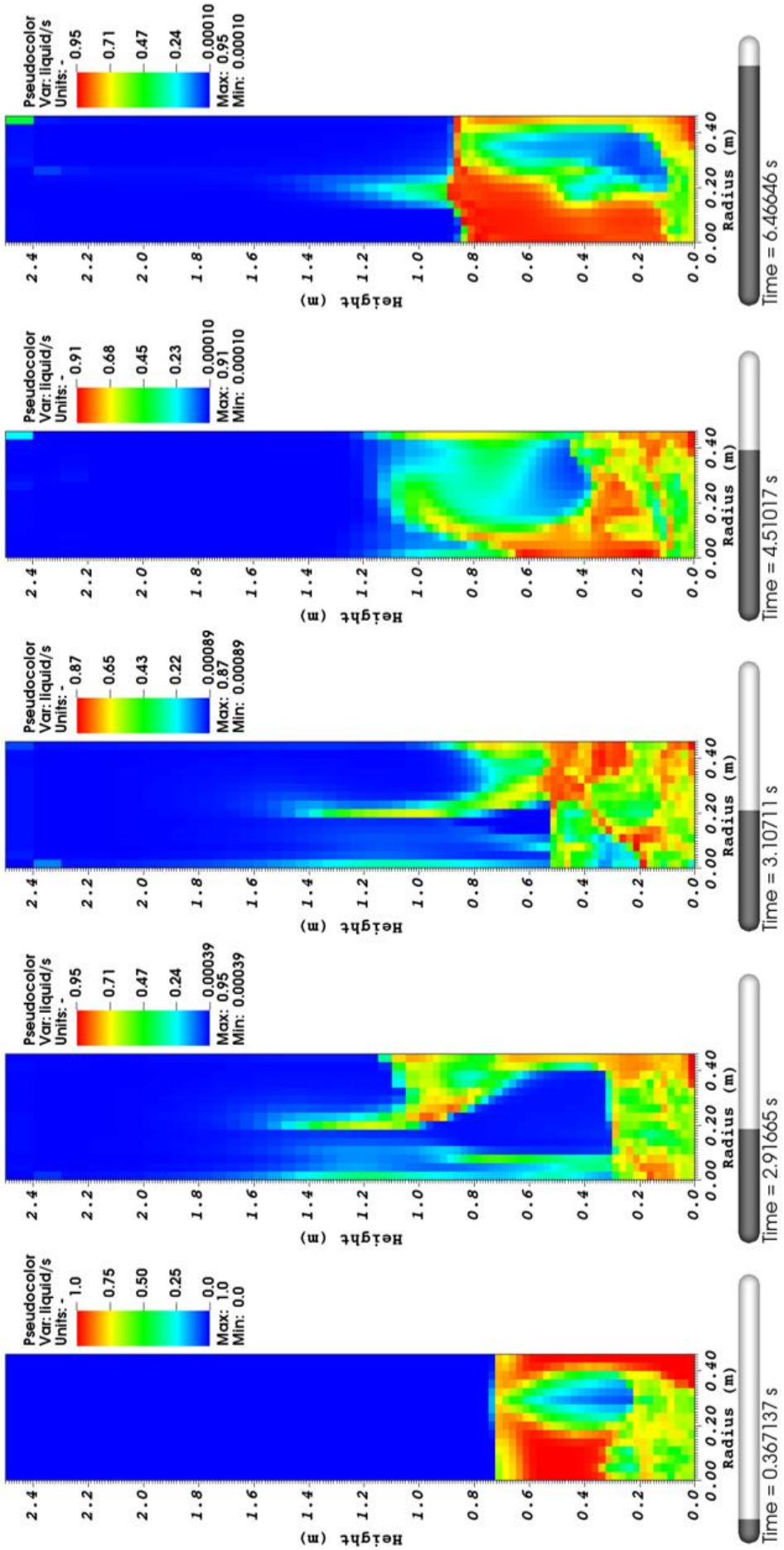

Figure 5.15 Two-Phase flow simulation of molten corium and steam for a reactor scenario with new Bubbly-Channel interfacial friction law. The sacrificial concrete is assumed partially ablated. Legend: Volume ratio of melt.

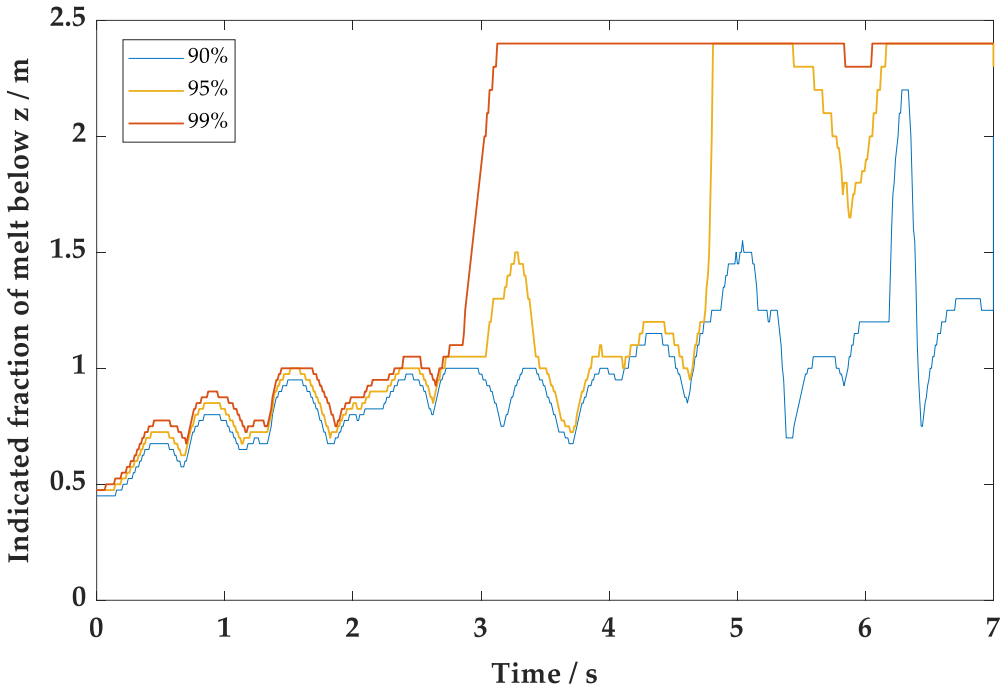

Figure 5.16 Average level of the molten corium layer as a result of steam ingression from below and two-phase flow for a reactor case scenario simulation after partially ablated sacrificial layer.

Figure 5.17 shows the simulation results for the case where sacrificial concrete is completely ablated. For this case, as seen on the figure, the initial ingression of the steam looks like a blanket moving upwards with uniform steam and corium ratios in radial direction. In the later simulation time points a better mixing of the steam and corium is observed as a result of that. However, large voids still do occur but with less compact corium bulks around them. In addition, dispersion/ejection seem to occur for this simulation case rather later. Figure 5.18 shows the post processing evaluation of the simulation results. The void fraction gets higher for this simulation case up to 3.5 second mark in simulation time. In the later time points of the simulation, the positioning of the melt is less fluctuated and overall average void for this simulation case is around 0.50.

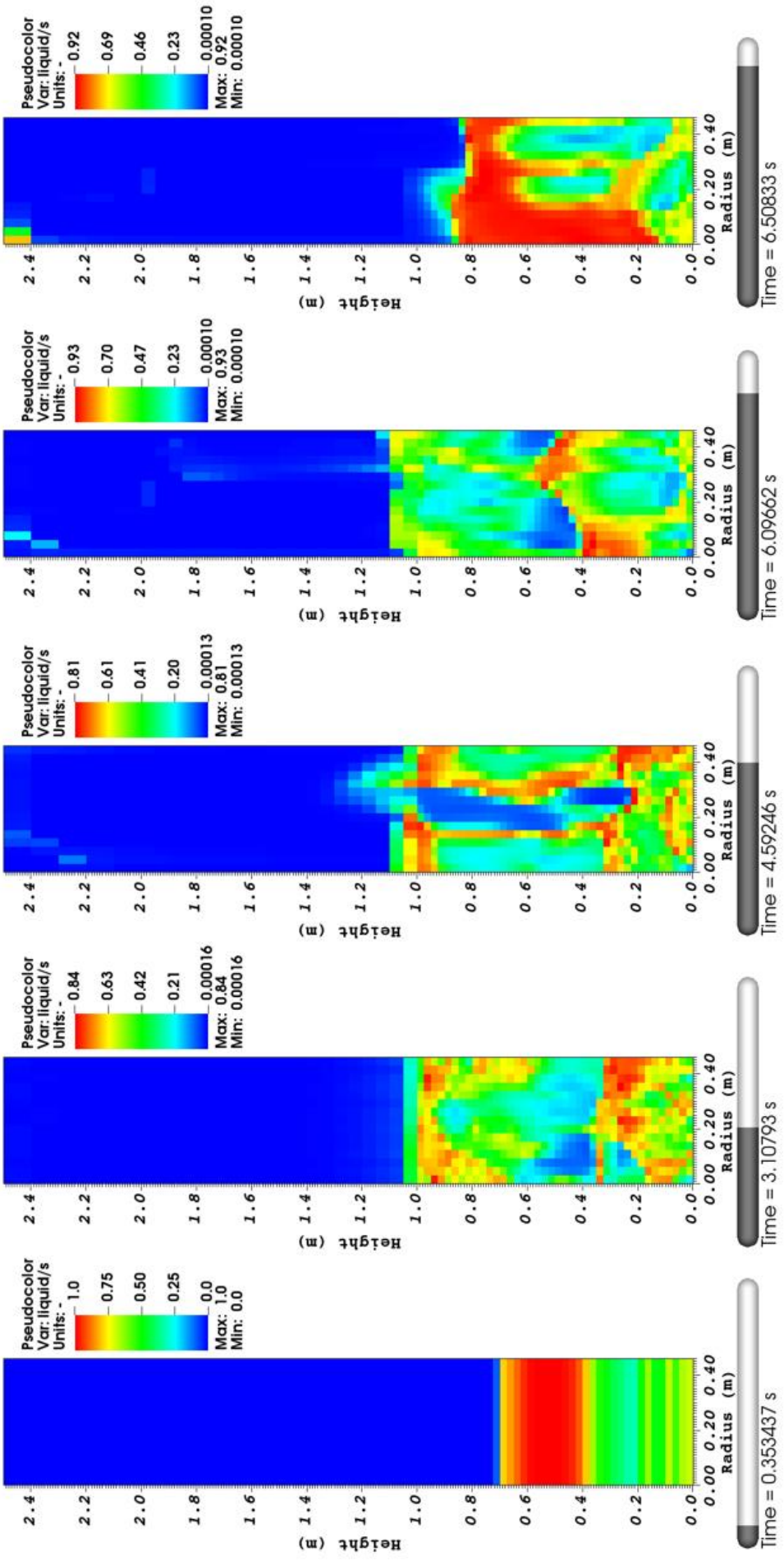

Figure 5.17 Two-Phase flow simulation of molten corium and steam for a reactor scenario with new Bubbly-Channel interfacial friction law. The sacrificial concrete is assumed completely ablated. Legend: Volume ratio of the melt.

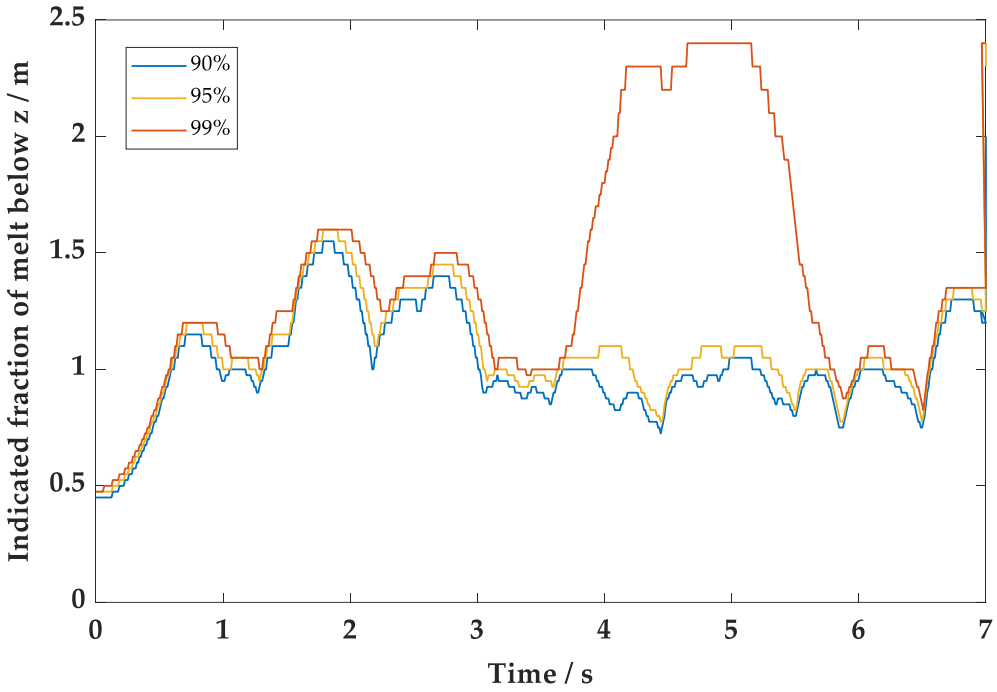

Figure 5.18 average level of the molten corium layer as a result of steam ingression from below and two-phase flow for a reactor case scenario simulation after completely ablated sacrificial layer.

The analysis in this chapter shows that it is possible to model the interaction between steam and molten corium during bottom cooling by two-phase modelling with moving molten corium. Instead of relying on the pressure difference as in previous works, in this current analysis the corium is actually modelled as a liquid that moves in accordance with density, viscosity and the surface tension between steam, resulting in more realistic coolant ingression modelling. The dispersion and ejection of the melt is represented with such modelling as well. The advantage of this approach is that all fragmentation and steam escaping occur with directly applied friction laws. This provides a more realistic information on where and how the final void would form in solidified melt, which is critical for long-term cooling analysis. However, this approach is also challenging as it requires careful consideration of flow region, distribution and flow profile modelling for the friction. As existing two-phase flow interfacial friction force models failed to represent the physics and outcome of the COMET research, a two-phase flow interfacial friction force model is developed by this work, which is able to represent both the bottom cooling phenomenon and the outcome of CometPC experiments successfully.

The ultimate aim of the interfacial friction model development is to be able to simulate the entire severe accident scenario that leads to bottom cooling and consequent corium mitigation ability. Due to the complexity of 3-phase-flow modelling and the time restrictions, this work presents the steam-melt two-phase flow. This leaves room for further development of the current approach, which can be based on the outcome of this work.

6 Summary and Outlook

Stabilization and cooling of corium in the ex-vessel has the utmost importance for terminating the severe accident and preventing radiation release to the environment. The COMET research by KIT has shown that the bottom cooling concept is the most effective in terms of removing heat from the corium, and fragmentation that enables long term cooling of decay heat generated by the corium. Moreover, the porous concrete design variation of the bottom cooling core catcher concept, CometPC, could enable back-fitting of this concept to existing Generation II reactors thanks to its simplistic design. Prior to this work, the porous concrete core catcher concept had been investigated experimentally in a rather small scale compared to reactor geometry. Therefore, a comprehensive investigation of the capability of porous concrete core catcher for providing coolant passively into the molten corium layer in a large reactor geometry was necessary. In terms of interaction between coolant and molten corium, a multi-phase flow model for adequate simulation of corium and steam interaction during bottom flooding had not existed. Since the main effectiveness of the bottom cooling comes from successful fragmentation of the compact corium layer, it was necessary to model molten corium as moving liquid in a multi-phase flow with coolant and determine the coolant space in corium.

This work determined the relation between hydraulic parameters of a porous concrete core catcher for reactor application by coolant flow simulations through porous concrete layers with COCOMO3D code. A generic Generation II PWR design was used as basis for the device dimensions. The investigations showed that for cooling water provided from the side of the bottom layer of the core catcher device, a certain correlation between permeabilities of upper concrete layer and lower concrete layer was necessary for homogenous distribution of sufficient cooling water into the melt layer. The permeability of the porous concrete layers, as well as their thickness had an effect on the pressure losses in the device which have a direct effect on required pressure head for the cooling water storage for the core catcher.

An optimization methodology for the hydraulic parameters of a porous concrete core catcher was developed in this work. This optimization methodology can be applied in-

dependently of the boundary conditions. Through this optimization possible combinations for hydraulic parameters can be determined for a desired outcome or allowed boundary conditions, and the design decisions can be made with the help of the outcome of the optimization. For instance, various concrete type pairings could be chosen for the same aimed cooling water flow rate. Based on the aimed cooling water flow rate, the concrete types for the core catcher could be chosen for suitable passive flooding pressure head. For the design case where the cooling water is provided around the core catcher circumference, reasonable pressure values at the inlet could be realized for the necessary coolant flow rate and distribution into the melt layer. CometPC experiments had shown that when coolant rises towards melt layer with a volume flow rate of 1-2 l/s it causes sufficient break-up in the compact melt layer and cooling. This volume flow rate is in agreement with the required mass flow rate of coolant in order to remove potential decay heat of 40 MW in an accident scenario in a reactor. A rising superficial velocity of 1.5×10^{-3} m/s into the molten corium layer in a reactor can be provided with different concrete layer pairings. One possibility for delivering this superficial velocity with only 10% variation over the surface of the core catcher is a porous core catcher design where the lower and upper concrete layers have equal thickness of 0.16 m, with 1.46×10^{-12} m^2 permeability of the upper layer and 1.96×10^{-9} m^2 permeability of the lower layer, with a circumferential water inlet on the side of the core catcher. For this design example a pressure loss of 104.22 kPa in the core catcher was found. This evaluation showed the major role that the porous concrete types play for the distribution of sufficient coolant for the large reactor geometry.

Besides the ideal case, the design limitations for the back-fitting conditions were investigated as well. For back-fitting, a restricted singular channel water inlet on the side of the lower layer of the core catcher was assumed. A singular inlet channel causes very high mass flow rates at the inlet region of the core catcher, which raised the question of adequacy of the linear friction law (permeability) used for flow through porous concrete. High velocities of fluid will result in non-negligible inertia, hence a quadratic relation between flow rate and pressure losses (passability). Underestimating the friction losses along the porous concrete could lead to insufficient cooling water supply in an application. Therefore, it was necessary to perform single inlet simulations for reactor geometry with non-linear adequate friction relations of porous concretes.

The literature shows that the friction law that applies to fluid flow through porous concrete is determined almost exclusively by measurements. Based on this, an experimental set-up was built explicitly for this work. In this set-up, the pressure losses against water flow rates of porous concrete samples from actual CometPC experiments were measured by falling head method. The results indeed showed a non-linear dependency between pressure losses in the samples and flow rate of water. The permeability and passability values obtained from this measurement results, and the relation between them were applied in COCOMO3D simulation for the restricted single inlet case. The simulations showed that a uniform distribution of the coolant into the melt layer from below over the entire contact surface with sufficient flow rates to remove the heat is possible even

with a singular water inlet connection. However, the corresponding pressure difference along the core catcher was very high. Furthermore, the permeability and passability values that realizes this could either cause structural problems or could be difficult to manufacture. In conclusion, it was found that increasing the area of the water inlet and providing it uniformly from the perimeter of the porous core catcher device is more feasible approach for the reactor application.

Another advantage of measuring the permeability and passability of the samples from concretes used in CometPC experiments was that it provided an insight into the pressure losses within the system. By means of COCOMO3D a simulation domain was created with CometPC Plus experiment data in order to determine the pressure loss in the concrete layer during CometPC experiments, its relation to the progress of the cooling and to compare this pressure loss with the effective overpressure of the cooling water. The now known porous concrete permeability and passability was applied to the simulation with boundary conditions and geometry from the experiment. Although there were still some uncertainties from the nature of the experiment, it was clear that a significant pressure loss is imposed by the melt layer. This specific evaluation once again showed how necessary it was to actually model the porosity formation in corium and to model the corium as a moving liquid.

For modelling of fragmentation/porosity formation in molten corium by bottom flooding, a new interfacial friction model for two-phase flow of molten corium and steam was developed in this work. Corium-coolant flow that occurs during bottom flooding is a highly complex multi-phase flow. For the modelling approach in this work, it was assumed that the initial two-phase flow between molten corium and steam, where the steam penetrates into compact corium and creates flow patterns due to movement of molten liquid and steam, was the deciding phenomenon for the final porosity of the solidified corium.

As the initial interaction between molten-corium and steam occurs when the corium temperature is still very high, the temperature difference between the steam in interaction with molten corium was neglected compared to high temperatures of the melt. Therefore, melt and steam were assumed to be in thermal-equilibrium and the focus was interfacial momentum transfer between liquid corium and steam. As a pre-assessment, the applicability of the most common interfacial friction forces used in literature for water and steam two-phase flow were evaluated for corium and steam properties under bottom-cooling conditions with a stand-alone simulation code. Compared to the final porosity values of 45%-53% observed as a result of bottom cooling experiments it was clear that the standard interfacial friction forces for two-phase flow highly underestimate the friction between molten corium and steam under bottom cooling conditions.

A new interfacial friction force modelling for liquid corium-steam two phase flow was developed in this work. The new friction model was based on drag force modelling by Ishii and defined two flow regions during bottom flooding; bubbly flow for void fraction

less than 0.3 and bubbly-channel co-flow region for void fraction greater than 0.3. Moreover, two different velocities for steam were defined for bubbly flow and for channel flow, which is a more accurate representation of steam leaving the compact melt faster in form of a continuous channel.

The bubbly-channel interfacial friction model was validated against the outcome of the CometPC experiments (final porosity values of 45%-53%), for the steam inflow velocities of 15 – 38 m/s reached in the experiments, with a stand-alone simulation code. This new friction model and liquid properties of corium were implemented in COCOMO3D for two-phase flow simulations of liquid corium and steam. The simulation of CometPC Plus experiment was successfully recreating the morphology of the post-test cross-section and final porosity of the solidified thermite. The simulations with reactor case scenarios which can slightly differ from the CometPC experiments were consistent with average void fraction observed during simulation and with the morphology of the flow patterns. As the partial opening amount of sacrificial concrete varied in CometPC experiments, two cases were simulated for reactor case: the first one where the sacrificial concrete is partially (50%) ablated, the second one where the sacrificial concrete is completely ablated. For the case where, sacrificial concrete was simulated as completely ablated, a better mixing of the steam and corium was observed.

Instead of relying on the local pressure differences for fragmentation modelling as in prior works, this work modeled the corium as an actual liquid so it could move in accordance with its viscosity, density and surface tension with steam. This was a significant improvement this work contributed to the fragmentation modelling for bottom cooling. Thanks to the two-phase modelling the coolant ingression into to melt was simulated more realistically so that the effects of limitations such as partial opening of sacrificial layer could be observed. Moreover, the two-phase flow simulation in COCOMO3D could replicate the dispersion and melt ejection phenomenon that occurred in CometPC experiments which is expected to have influence on the final porosity of the melt layer. This dispersion phenomenon was observed in reactor case simulations as well.

Although the new interfacial friction model for two-phase flow was validated against CometPC experiment results, due to the complexity of these experiments the validation was only possible against a range. Due to uncommon material properties and boundary conditions of molten corium and steam two phase flow, it was not possible to find other experiments to validate the new friction law at this time. It is recommended for future works to perform two phase flow experiments with similar viscosity, density and surface tension to that of molten corium and steam so the new two-phase friction law could be validated against more specific experiment data. Moreover, the two-phase flow modelling of molten corium and steam should be extended in the future to three phase flow of molten corium, water and steam where the evaporation and condensation phenomena during corium interaction could be represented as well. This way, the entire process of corium cooling and solidification by bottom flooding could be simulated.

References

[1] International Energy Agency (IEA), "World Energy Outlook 2019," IEA Publications, Paris, France, 2018.

[2] International Atomic Energy Agency (IAEA), "Nuclear Power Reactors in the World," International Atomic Energy Agency, Vienna, Austria, 2019.

[3] Institut de Radioprotection et de Surete Nucleare IRSN, „Nuclear Power Reactor Core Melt Accidents - Current Stage of Knowledge," edp Sciences, France, 2015.

[4] International Nuclear Safety Advisory Group (INSAG-10), "Defence in Depth in Nuclear Safety," International Atomic Energy Agency, Vienna, Austria, 1996.

[5] B. R. Sehgal, Nuclear Safety in Light Water Reactors / Severe Accident Phenomenology, Oxford, UK: Academic Press - Elsevier, 2012.

[6] U. S. Nuclear Regulatory Commision, Office of Nuclear Regulatory Research, "Three Mile Island Accident of 1979 Knowledge of Management Digest, Overview," Washington, U. S. A. , 2016.

[7] U. S. Nuclear Regulatory Commission, "Backgrounder on the Three Mile Island Accident," 2018.

[8] International Atomic Energy Agency (IAEA), "The Fukushima Daiichi Accident - Report by the Director General," IAEA, Vienna, Austria, 2015.

[9] Tokyo Electric Power Company, Inc. (TEPCO), "Fukushima Nuclear Accident Analysis Report," Tokyo, Japan, 2012.

[10] U. S. Nuclear Regulatory Commission, "GE BWR4 Advanced Technology Manual / Chapter 7.1 Fukushima Dai-ichi Earthquake and Tsunami Event," 2014.

[11] American Nuclear Society Standarts Comittee Working Group ANS-5.1, „American National Standard Decay Heat Power in Light Water Reactors,“ American Nuclear Society, Illinois, USA, 2014.

[12] M. T. Farmer, B. W. Spencer, D. J. Kilsdonk and R. W. Aeschlimann, "Results of MACE Corium Coolability Experiments M0 and M1b," in *Proceedings of 8th International Conference on Nuclear Engineering (ICONE-8)*, Baltimore, Maryland, USA, 2000.

[13] M. T. Farmer and B. W. Spencer , "Status of the CORQUENCH Model for Calculation of Ex-Vessel Corium Coolability by an Overlying Water Layer," in *OECD (NEA) CSNI Workshop on Ex-Vessel Debris Coolability*, Karlsruhe, Germany, 1999.

[14] C. C. Chu, J. J. Sienicki, B. W. Spencer, W. Frid and G. Löwenhielm, "Ex-vessel melt coolant interactions in deep water pool: studies and accident management for Swedish BWRs," *Nuclear Enggineering Design,* pp. 159-213, 2 April 1995.

[15] Nuclear Energy Agency (NEA) - OECD, "State-of-the-Art Report on Molten Corium Concrete Interaction and Ex-Vessel Molten Core Coolability," OECD Publications, Boulogne-Billancourt, France, 2017.

[16] M. Fischer, „Main conceptual features of the EPR melt retention concept,“ in *Proceedings of OECD Workshop on Ex-Vessel Debris Coolability*, Karlsruhe, Germany, 1999.

[17] S. V. Svetlov, V. V. Bezlepkin, I. V. Kukhtevich, S. V. Bechta, V. S. Granovsky, V. B. Khabensky, V. G. Asmolov, V. B. Proklov, A. S. Sidorov, A. B. Nedoresov, V. F. Strizhov, V. V. Gusarov and Y. P. Udalov, "Core Catcher for TianWan NPP with VVER-1000 Reactor. Concept, Design and Justification.," in *Proceedings of 11th International Conference on Nuclear Engineering (ICONE-11)*, Tokyo, Japan, 2003.

[18] General Electric - Hitachi Nuclear Energy, "ESBWR Certification Probabilistic Risk Assesment Rev. 6," 2010.

[19] H. Alsmeyer and W. Tromm, "Experiments for a core catcher concept based on fragmentation," in *Proceedings of the International Topical Meeting on Advance Reactor Safety (ARS'94)*, Pittsburgh, PA, USA, 1994.

[20] H. Alsmeyer and W. Tromm, "The COMET concept for cooling core melt: evaluation of the experimental studies and use in the EPR," Report FZKA 6186, EXV-CSC(99)-D036, Forschungszentrum Karlsruhe, Germany, 1999.

[21] H. Alsmeyer and W. Tromm, "Concept of a core cooling system and experiments performed," *Nuclear Engineering and Design,* pp. 69-72, 1995.

[22] W. Tromm and H. Alsmeyer, "Experiments for a core catcher concept based on water addition from below," *Nuclear Engineering and Design,* pp. 437-445, 1995.

[23] H. Alsmeyer, T. Cron, G. Merkel, S. Schmidt-Stiefel, W. Tromm and T. Wenz, "Melt cooling by bottom flooding: The Experiment CometPC-H3," Forschungszentrum Karlsruhe, Germany, 2003.

[24] H. Alsmeyer, T. Cron, G. Merkel, S. Schmidt-Stiefel, W. Tromm and T. Wenz, "Melt Cooling by Bottom flooding: The Experiments CometPC-H4 and H5," Forschungszentrum Karlsruhe GmbH, Karlsruhe, Germany, 2004.

[25] C. Journeau and H. Alsmeyer, "Validation of the COMET Bottom-Flooding Core-Catcher with Prototypical Corium," in *Proceedings of International Congress on Advances in Nuclear Power Plants (ICAPP) '06*, Reno, NV, USA, 2006.

[26] J. J. Foit, M. Bürger, C. Journeau, H. Alsmeyer and W. Tromm, "Quenching of Melt Layer by Bottom Injection of Water in the COMET Core-Catcher Concept," in *The 3rd European Review Meeting on Severe Accident Research (ERMSAR-2008)*, Nesseber, Bulgaria, 2008.

[27] B. Fluhrer, J. Foit, T. Cron, M. Vervoortz and T. Wenz, "The MIT3BAR experiment to investigate the coolability of a simulated core melt with a modified CometPC concept," Karlsruhe Institute of Technology, Karlsruhe, Germany, 2016.

[28] D. Paladino, S. A. Theerthan and B. R. Sehgal, "Decobi: Investigation of Melt Coolability with Bottom Coolant Injection," *Progress in Nuclear Engineering,* pp. 161-206, 2002.

[29] S. Lomperski and M. T. Farmer, "Experimental investigation of corium quenching at elevated pressure," *Nuclear Enginnering Design,* pp. 905-917, 2007.

[30] S. Lomperski and M. T. Farmer, "Experimental evcaluation of the water ingression mechanism for corium cooling," *Nuclear Engineering and Design,* pp. 905-917, 2007.

[31] S. Lomperski and M. T. Farmer, "Performance testing of engineered corium cooling systems," *Nuclear Engineering Design,* pp. 311-320, 2012.

[32] H. Alsmeyer, H. Benz, T. Cron, W. Tromm, T. Wenz and F. Ferderer, "CometPC: First resuts for a simplified cooling concept based on porous concrete," in *Proceedings of the OECD Workshop on Ex-Vessel Debris Coolability*, Karlsruhe, Germany, 1999.

[33] W. Tromm and H. Alsmeyer, "Ex-Vessel Corium Cooling By Passive Water Addition Through Porous Concrete," in *Proceeding of International Congress on Advences in Nuclear Power Plants*, Nice, France, 2001.

[34] W. Widmann, M. Bürger and G. Lohnert, "Theoretical Investigations of the COMET Concept for Ex-Vessel Core Melt Retention," in *Proceedings of The International Congress on Advances in Nuclear Power Plants (ICAPP'04)*, Pittsburgh, PA, USA, 2004.

[35] W. Widmann, M. Bürger, G. Lohnert, H. Alsmeyer and W. Tromm, "Experimental and thoretical investigations on the COMET concept for ex-vessel core melt retention," *Nuclear Engineering and Design,* pp. 2304-2327, 2006.

[36] S. Rahman, Coolability of Corium Debris Under Severe Accident Conditions in Light Water Reactors, PhD Thesis, Stuttgart: Institute of Nuclear Technology and Energy Systems (IKE), University of Stuttgart, 2013.

[37] J. Bear, Dynamics of Fluids in Porous Media, New York: Dover Publications Inc., 1972, pp. 148-151.

[38] J. Bear, Modeling Phenomena of Flow and Transport in Porous Media, Switzerland: Springer, 2018, pp. 266-267.

[39] F. A. L. Dullien, „Single phase flow through porous media and pore structure," *The chemical engineering journal, Volume 10, Issue1,* pp. 1-34, 1975.

[40] I. F. Macdonald, M. S. El-Sayed, K. Mow and F. A. L. Dullien, "Flow Through Porous Media - the Ergun Equation Revisited," *Industrial & Engineering Chemistr Fundamentals,* pp. 199-208, 1979.

[41] S. Ergun, "Fluid flow through packed columns," *Chemical Engineering Progress,* pp. 89-94, 1952.

[42] M. Ishii and T. Chawla, "Local Drag Laws in Dispersed Two-phase Flow," Argonne National Laboratory, IL, USA, 1979.

[43] M. Ishii and N. Zuber, "Drag Coefficient and Relative Velocity in Bubbly, Droplet and Particulate Flows," *The American Institute of Chemical Engineers Journal,* pp. 843-855, September 1979.

[44] M. Ishii and K. Mishima, "Two-Fluid model and hydrodynamic constitutive relations," *Nuclear Engineering and Design,* pp. 107-126, 11 November 1984.

[45] M. Ishii and T. Hibiki, Thermo-Fluid Dynamics of Two-Phase Flow (Second Edition), New York, NY, USA: Springer, 2011.

[46] C. S. Brooks, T. Hibiki and M. Ishii, "Interfacial drag force in one-dimensional two-fluid model," *Progress in Nuclear Energy,* pp. 57-68, 12 July 2012.

[47] W. H. Amarasooriya and T. G. Theofanous, "Premixing of steam explosions: a three-fluid model," *Nuclear Engineering and Design,* pp. 23-39, 1991.

[48] R. Meignen, S. Picchi, J. Lamome, B. Raverdy, S. C. Escobar and G. Nicaise, "The challenge of modeling fuel–coolant interaction: Part I – Premixing," *Nuclear Engineering and Design,* pp. 511-527, 2014.

[49] N. Zuber and J. A. Findlay, "Average volumetric concentration in two-phase flow systems," *The Journal of Heat Transfer,* 1965.

[50] M. Ishii, "One-dimensional drift-flux model and constitutive equations for relative motion between phases in various two-phase flow regimes," Argonne National Laboratory, Illinois, USA, 1977.

[51] I. Kataoka and M. Ishii, "Prediction of Pool void Fraction by new drift flux correlation," Argonne National Laboratory, Illinois, USA, 1986.

[52] B. Tourniaire, E. Dufour and B. Spindler, "Foam formation in oxidic pool with application to MCCI real material experiments," *Nuclear Enginering and Design,* pp. 1971-1978, 6 May 2009.

[53] C. Journeau and J.-F. Haquet, "Void fraction for gas bubbling in shallow viscous pools - application to molten core concrete interactions," in *Proceedings of ICONE13 (13th International Conference on Nuclear Engineering)*, Beijing, China, 2005.

[54] G. Pohlner, M. Buck and S. Rahman, "Modeling and Validation Basis of JEMI code," Institute of Nuclear Technology and Energy Systems (IKE), University of Stuttgart, Stuttgart, 2013.

[55] A. Berkhan, M. Buck, G. Pohlner and S. Rahman, "Modeling and Validation Basis of the MEWA code," Insiture of Nuclear Technology and Energy Systems (IKE), University of Stuttgart, Stuttgart, 2013.

[56] G. Pohlner, Z. Vujic, M. Bürger and G. Lohnert, "Simulation of melt jet breakup and debris bed formation in water pools with IKEJET/IKEMIX," *Nuclear Engineering and Design,* pp. 2026-2048, 2006.

[57] M. Buck, M. Bürger, S. Rahman and G. Pohlner, "Validation of the MEWA Model for Quenching of a Severely Damaged Reactor Core," in *Joint OECD/NEA EC/SARNET2 Workshop on In-Vessel Coolability*, Paris, France, 2009.

[58] M. Buck, Modeling of the Late Phase of Core Degradation in Light Water Reactors, PhD Thesis, Stuttgart: Institute of Nuclear Technology and Energy Systems (IKE), University of Stuttgart, 2007.

[59] W. Schmidt, Influence of Multidimensionality and Interfacial Friction on the Coolability of Fragmented Corium, PhD Thesis, Stuttgart: Institute of Nuclear Technology and Energy Systems (IKE), University of Stuttgart, 2004.

[60] M. Bürger, M. Buck, W. Schmidt and W. Widmann, "Validation and application of the WABE Code: Investigations of constitutive laws and 2D effects on debris," *Nuclear Engineering and Design,* pp. 2164-2188, 2006.

[61] Z. Vujic, Improvement and Verification of Steam Explosion Models and Codes for Application to Accident Scenarios in Light Water Reactors, PhD Thesis, Stuttgart: Institute of Nuclear Technology and Energy Systems (IKE), University of Stuttgart, 2008.

[62] M. Buck and G. Pohlner, "Contribution to first Annual Progress Report of the MIT3BAR Project," Institut of Nuclear Technology and Energy Systems, Stuttgart, 2014.

[63] D. H. Nguyen, N. Sebaibi, M. Boutouil, L. Leleyter and F. Baraud, "A modified method for the design of pervious concrete mix," *Construction and Building Materials,* pp. 271-282, 2014.

[64] A. Ibrahim, E. Mahmoud, M. Yamin and V. Patibandla, "Experimental study on Portland cement pervious concrete mechanical and hydrological properties," *Construction and Building Materials,* pp. 524-529, 2014.

[65] National Institute of Standarts and Technology, „NIST Chemistry WebBook, Isothermal Properties for Water," U.S. Department of Commerce, Gaithersburg, Maryland, 2018.

[66] B. Huang, L. N. Mohammad, A. Raghavendra and C. Abadie, "Fundamentals of permeability in asphalt mixtures," in *Proceedings of The Annual Meeting of the Association of Asphalt Paving Technologies*, Chicago, Illinois, 1999.

[67] M. U. Maguesvari and V. L. Narasimha, "Studies on Characterization of Pervious Concrete for Pavement Applications," *Procedia - Social and Behavioral Sciences,* pp. 198-207, 2013.

[68] R. Zhong and K. Wille, "Material design and characterization of high performance pervious concrete," *Construction and Building Materials,* pp. 51-60, 6 August 2015.

[69] C. Journeau, J.-F. Haquet, B. Spindler, C. Spengler and J. Foit, "The VULCANO VE-U7 Corium spreading benchmarking," *Progress in Nuclear Energy,* no. 48, pp. 215-234, 2006.

[70] C. Journeau and J.-F. Haquet, "Convection heat transfer anisotropy in a bubbling viscous pool-Application to molten core-concrete interaction," *Nuclear Engineering and Design,* pp. 389-394, 27 October 2009.

[71] T. Zeiser, Simulation und Analyse von durchströmten Kugelschütungen in engen Rohren unter Verwendung von Hochleistungsrechnern, PhD Thesis, Erlangen: Universität Erlangen-Nürnberg, 2008.

[72] H. Freund, T. Zeiser, F. Huber, E. Klemm, G. Brenner, F. Durst and G. Emig, "Numerical simulations of a single phase reacting flows in randomly packed fixed-bed reactors and experimental validation.," *Chemical Engineering Science,* pp. 903-910, 2003.

[73] Y. Qin, H. Yang, Z. Deng and J. He, "Water Permeability of Pervious Concrete is Dependent on the Applied Pressure and Testing Methods," *Advences in Material Science and Engineering,* 2015, Article ID 404136.

[74] J. Yang and G. Jiang, "Experimental study on properties of pervious concrete pavement materials," *Cement and Concrete Research,* pp. 381 - 386, 13 August 2003.

[75] W. Martin III, „Impact of vertical porosity distribution on the permeability of pervious concrete," *Construction and Building Materials,* pp. 78-84, 14 March 2014.

[76] M. D. M. Innocentini, V. R. Salvini, A. Macedo and V. C. Pandolfelli, "Prediction of Ceramic Foams Permeability Using Ergun's Equation," *Materials Research , Vol2, No. 4,* pp. 283-289, 1999.

[77] B. Huang, H. Wu, X. Shu and E. G. Burdette, "Leboratory evalution of permeability and strength pf polymer-modeified pervious concrete," *Construction and Building Materials,* pp. 818 - 823, 15 October 2010.

[78] F. M. White, Fluid Mechanics, 7th Editon, New York, USA: McGraw-Hill, 2011.

[79] D. A. Barbarossa, „Messung der Wasserdurchlässigkeit von porösem Beton mit veränderlichem hydraulischen Gefälle, Bachelor Thesis," IKE, University of Stuttgart, Stuttgart, 2017.

[80] T. Sevon, C. Journeau and L. Ferry, "VULCANO VB-U7 experiment on interaction between oxidic corium and hematite-containing concrete," *Annals of Nuclear Energy,* pp. 224-229, 10 May 2013.

[81] C. Journeau, P. Piluso, J. F. Haquet, E. Boccaccio, V. Saldo, J. M. Bonnet, S. Malaval, L. Carenini and L. Brissonneau, "Two-dimensional interaction of oxidic corium with concretes: The VULCANO VB test series," *Annals of Nuclear Energy,* pp. 1597-1613, 26 August 2009.

[82] C. Journeau, P. Piluso, J. F. Haquet, L. Brissonneau and V. Aubert-Saldo, "Behaviour of nuclear reactor pit concretes under severe accident conditions," in *Proceedings of CONSEC '07 Concrete Under Severe Conditions* , Tours, France, 2007.

[83] K. Mikityuk, P. Coddington and R. Chawla, "Developement of a Drift-flux Model for Heavy Liquid Metal / Gas Flow," *Journal of Nuclear Science and Technology,* pp. 600-607, July 2005.

[84] J.-C. Casan and M. L. Corradini, "Study of void fraction and mixing immiscible liquids in a pool configuration by an upward gas flow," *Nuclear Technology,* pp. 104-119, 1992.

Appendix A: Further Simulation Results on Hydraulic Properties Porous Concrete Core Catcher

Single Effect Simulations – Influence of the Concrete Layer Thickness

As a part of the single effect simulations performed in Chapter 3.4, the influence of relative thickness of the concrete layers on the pressure loss in the core catcher and water distribution was investigated as well. The input for the simulation is described in Chapter 3.4 and shown in Table 3.5.

Figure A.1 shows the simulation with thicker upper concrete layer. The simulation domain and the cross-section figure are similar to the those of Figure 3.4 and Figure 3.6. The total pressure difference within the core catcher system is 159.32 kPa. Although the total height of the system is the same, since the height of the low porosity layer is higher than that of reference case (Figure 3.6) the pressure difference is higher. Based on the white arrows on the left-hand side that represent the volume flow rate of cooling water, not a drastic change in the flow distribution is noticeable.

Figure A.2 shows the simulation with thinner upper concrete layer. In this case, the total pressure difference within the core catcher system is decreased to approximately 52.72 kPa. The lower permeability layer height ratio is only one fourth of the total height of the device, so this low-pressure difference along the system as a result of less friction losses is in accordance with expectancy in this case.

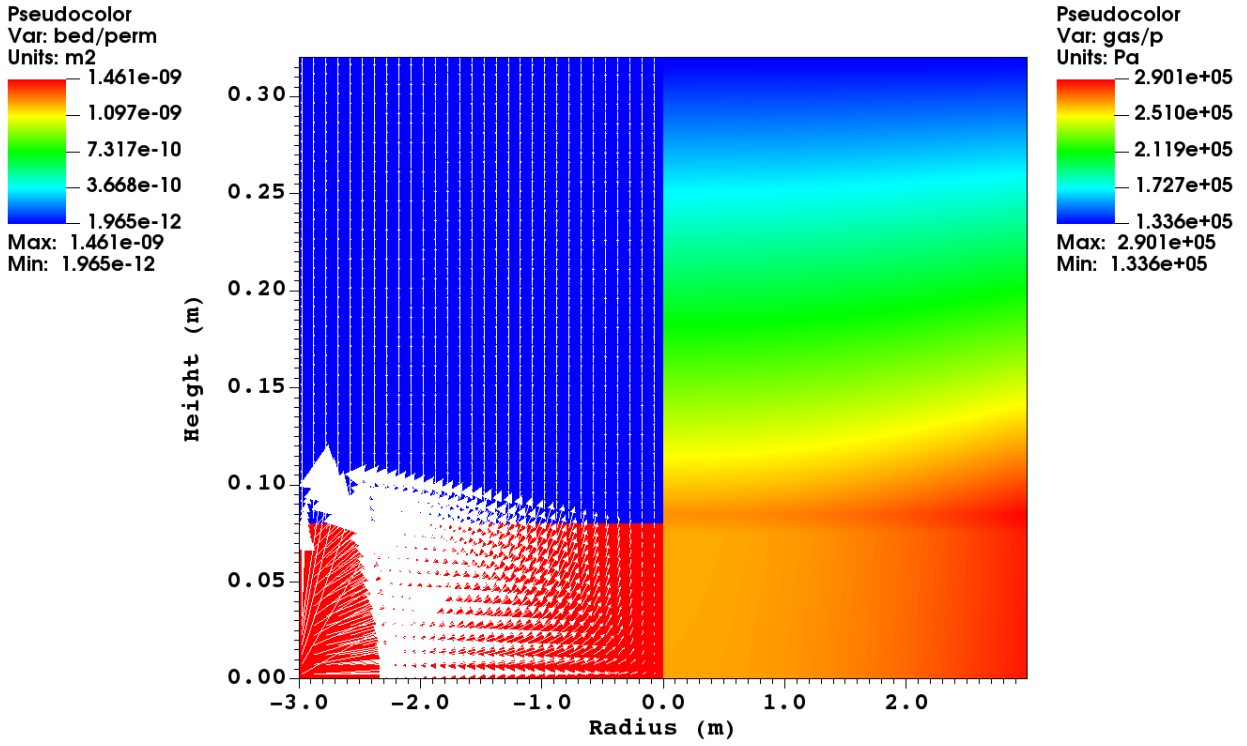

Figure A.1 Simulation results for the water flow through porous concrete layers for thicker upper concrete layer. Left: permeability and vectoral representation of the cooling water flow. Right: Pressure distribution.

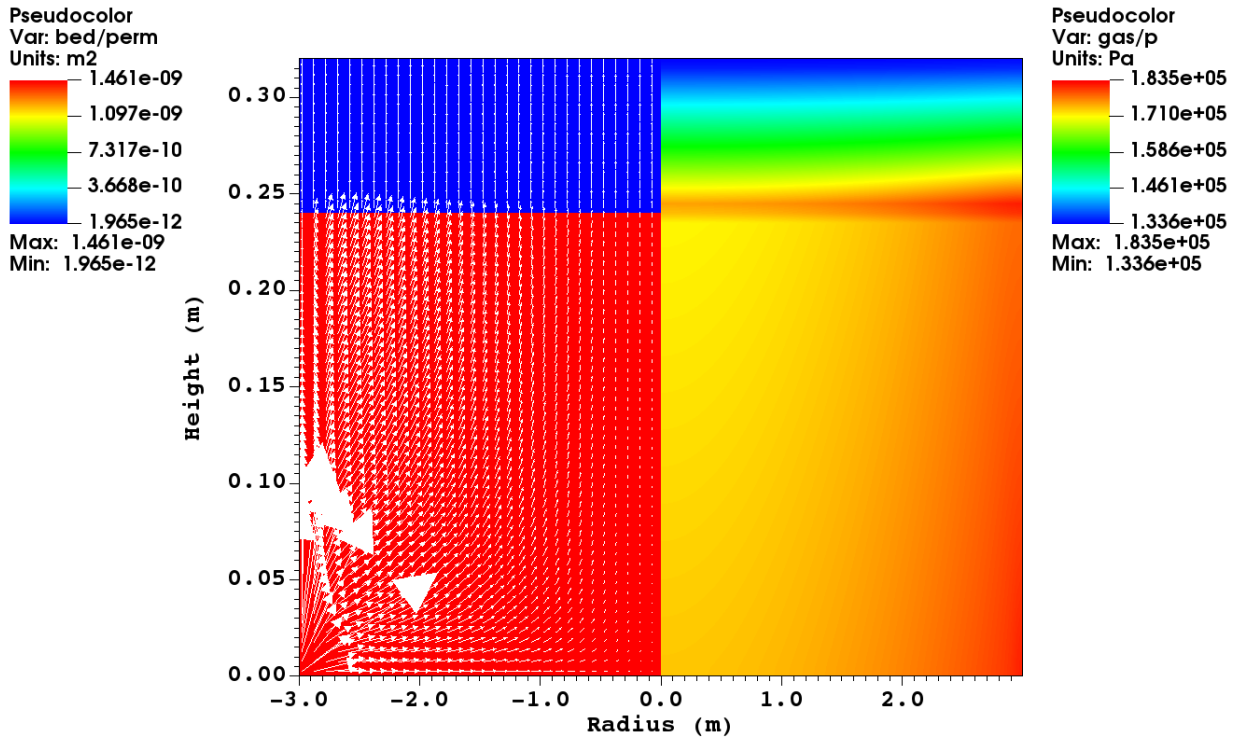

Figure A.2 Simulation results for the water flow through porous concrete layers for altered concrete layer thicknesses. Left: permeability and vectoral representation of the cooling water flow. Right: Pressure distribution.

Distribution of the superficial water velocity on the top surface of upper concrete layer for the thinner upper layer and thicker upper layer cases are shown in Figure A.3 in comparison with the superficial water velocity distribution for the uniform reference case from Figure 3.7. The uniformity of the superficial water velocity changes slightly when other parameters were kept the same in the simulation. Although the permeability values are the same for each layer for the compared simulations, the change in height has an effect on the overall pressure losses within the system, hence an effect on the radial distribution of the water, although the average flow rates are the same.

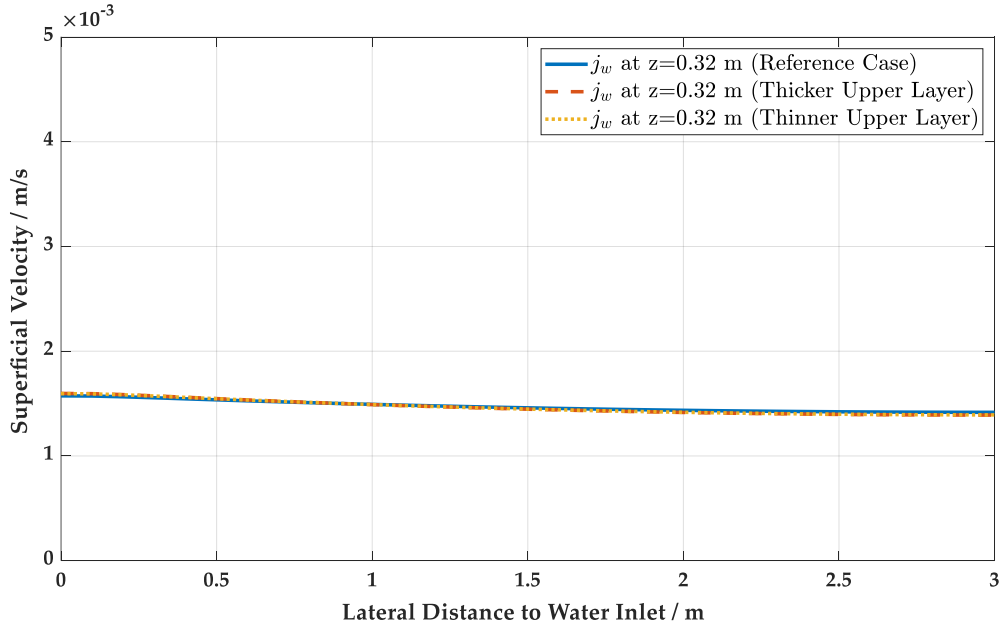

Figure A.3 Superficial velocity of the cooling water at z=0.32 m (the contact surface of corium and upper concrete layer) in axial direction for altered porous concrete layer thicknesses, in comparison with the superficial velocity of the cooling water from reference case.

Single Effect Simulations – Influence of the Water Flow Rate

As a part of the single effect simulations performed in Chapter 3.4, the influence of the water flow rate on the pressure loss in core catcher and water distribution was investigated as well. The input for the simulation is described in Chapter 3.4 and shown in Table 3.5.

The simulation result for higher cooling water mass flow rate case is shown on Figure A.4. The total pressure difference within the core catcher system is increased to 115.4 kPa. Compared to reference case a drastically higher pressure difference along the core catcher is observed. This increase in pressure difference is the result of increased mass flow rate at the entrance of the system that causes higher pressure losses.

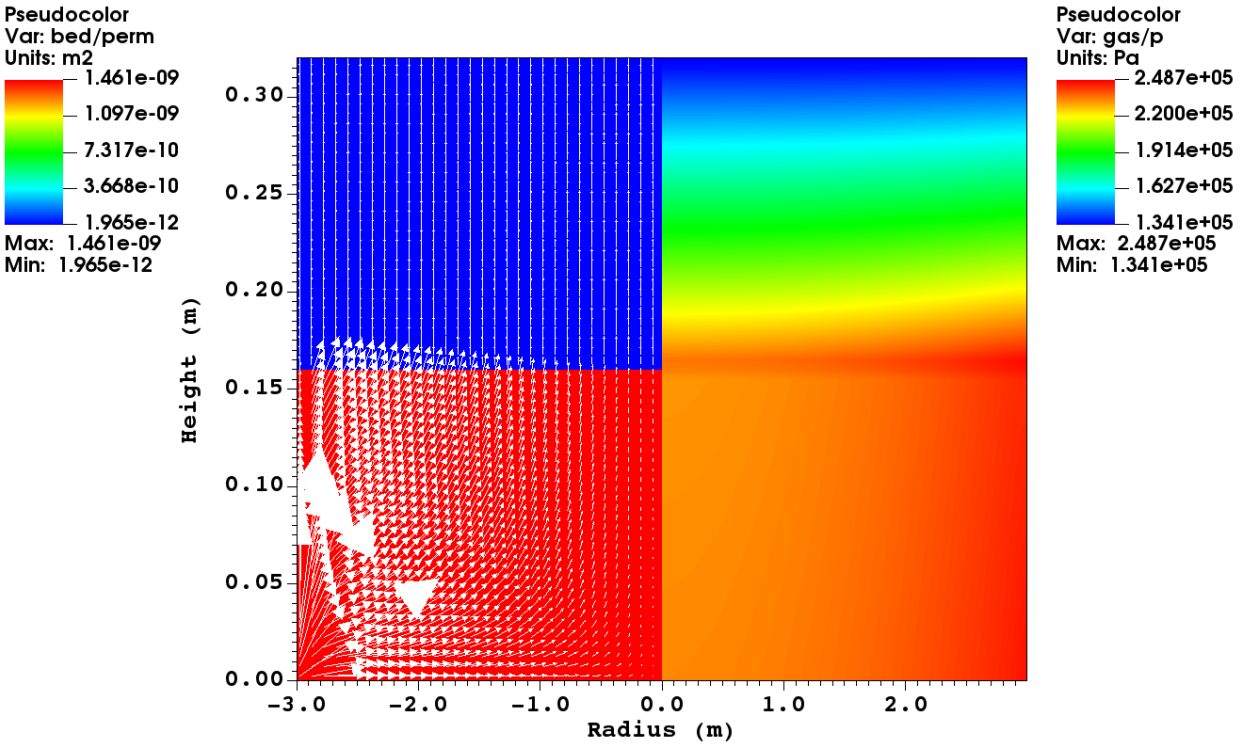

Figure A.4 Simulation results for the water flow through porous concrete layers for higher mass flow rate. Left: permeability and vectoral representation of the cooling water flow. Right: Pressure distribution.

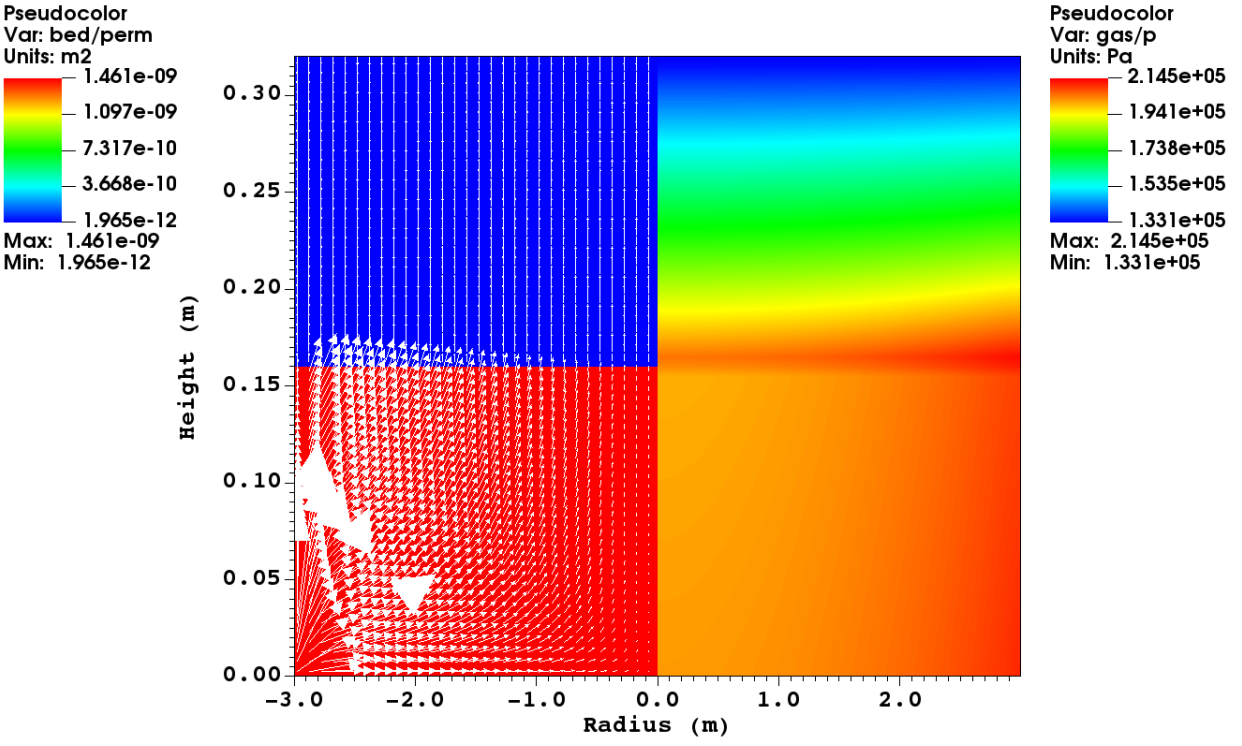

Figure A.5 Simulation results for the water flow through porous concrete layers for lower mass flow rate. Left: permeability and vectoral representation of the cooling water flow. Right: Pressure distribution.

For the lower mass flow rate of the cooling water, compared to reference case, the pressure difference along the core catcher is decreased to 80 kPa as seen in the Figure A.5.

The diagram in the Figure A.6 shows that the superficial water velocity distributions for altered mass flow rate cases are same to the one of uniform reference case, only equally higher or lower at every point due to the higher or lower mass flow rate as an input.

It can be concluded based on these simulations with altered mass flow rate through porous concrete system that the total pressure difference in the system is proportional to the mass flow rate. Importantly, the uniformity of the superficial velocity is not affected by that.

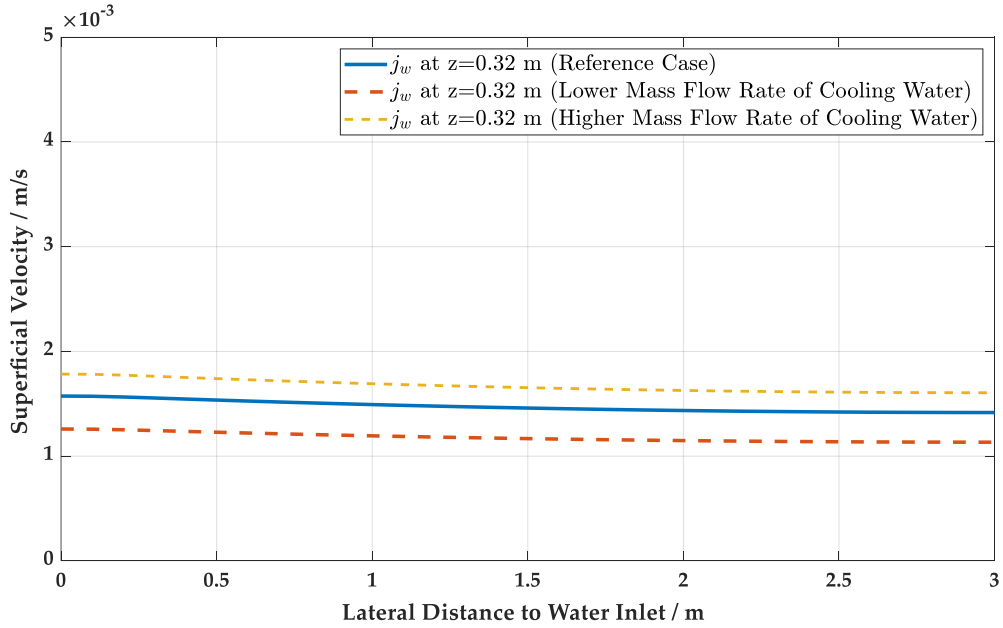

Figure A.6 Superficial velocity of the cooling water at z=0.32 m (the contact surface of corium and upper concrete layer) in axial direction for new mass flow rate, in comparison with the superficial velocity of the cooling from reference case.

Optimization Simulations – Comparison of all Optimized Cases

A comprehensive comparison of the change in total pressure difference in the core catcher system with changing permeability of lower layer for various coolant mass flow rates through the system and for various height ratios of concrete layers are shown in Figure A.7. The diagram shows only pressure difference values up to 120 kPa. The upper layer permeabilities that are fulfilling each optimization criterion when paired with the lower layer permeability in this diagram for each case can be found in Chapter 3, Figure 3.11 and Figure 3.13.

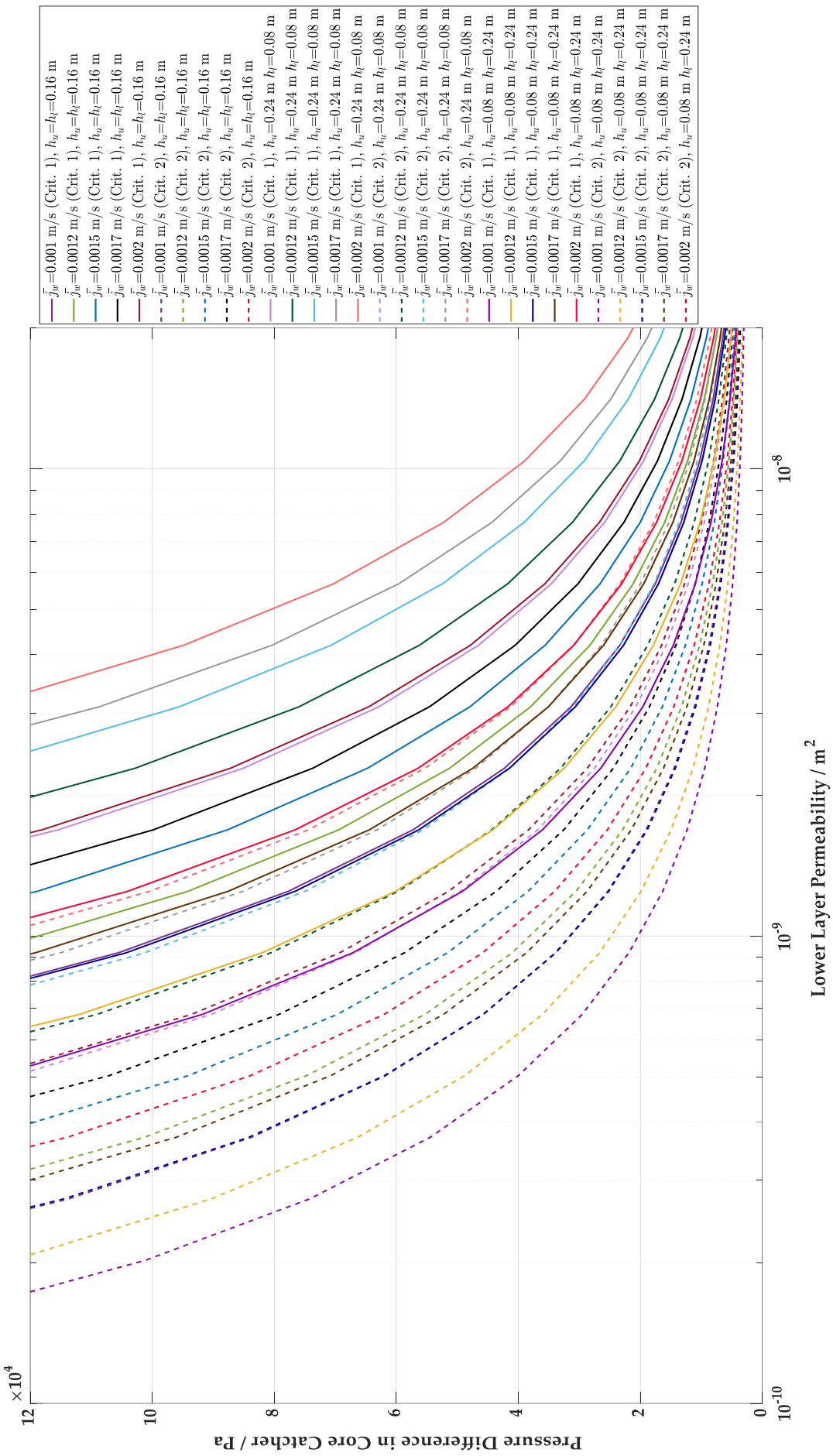

Figure A.7 Change in pressure difference in the core catcher in relation to lower layer permeability for different layer thickness ratios and different mass flow rates of coolant. Solid line: Crit. 1 is fulfilled, dashed line: Crit. 2 is fulfilled,

Appendix B: Uncertainty Analysis of Permeability Measurements and Error Propagation

Uncertainty Analysis

The total uncertainty of the measurements that were performed in Chapter 4, arises from systematic uncertainty and random uncertainty of the measured values. Systematic uncertainty is the measurement uncertainty of the pressure transducers as stated by the manufacturer and does not depend on the measurement method or conditions. Random uncertainty lies within the variation of repeated measurements of the same sample and gives an idea about the reproducibility of used measurement method. These uncertainties of the measured values will be reflected on the quantities that depend on the measured values and this effect can be determined by error propagation.

The total standard uncertainty of systematic uncertainty (u_{syst}) and random uncertainty (u_{rand}) of a measured value X is called combined uncertainty (u_c) and it can be calculated as follows:

$$u_c(X) = \sqrt{u_{syst}(X)^2 + u_{rand}(X)^2} \tag{B.1}$$

The measurement uncertainty of the pressure sensors that are used in this work to measure relative pressure and differential pressure are given in Table B.1 as stated by the manufacturer.

Measurements with each sample were repeated multiple times in order to determine reproducibility and the random uncertainty of the measured value. Since the measurements were transient and not performed in steady state, it was inherently challenging to perform statistical analysis of the repetitions. Once the beginning time of the measurements was assigned, for each repeated measurement the pressure value at t=5 s and the pressure value at the end of the experiment (at t=175 s for F1, t=195 s for F2, t= 30 s for C1 and t=30 s for C2) were used for statistical analysis.

Table B.1 Uncertainty of pressure sensors as given by the manufacturer (FS: Full Scale).

Sensor	Measurement Range	Uncertainty	
Pressure Transducer 1 (Relative Pressure) Keller PR-23	0-1 bar	0.1% FS	±0.001 bar
Pressure Transducer 2 (Differential Pressure) Keller PD-33X	1 bar	0.1% FS	±0.001 bar

For each sample, the measured pressure differences within the exact time frame were used as the measurement value for analysis. These measured pressure values are summarized in Table B.2. The pressure values seen on the table are given in bar. p_{rel} is the pressure value measured by Pressure Transducer 1, which corresponds to the value of $p_1 - p_0$ from Chapter 4. p_{dif} is the pressure value measured by Pressure Transducer 2, which corresponds to the value of $p_2 - p_1$ from Chapter 4.

The uncertainty of values obtained from repeated measurements is characterized by standard deviation of measured pressure value, which for the same sample is calculated as follows:

$$u_{rand}(X) = \sqrt{\frac{\sum_{i=1}^{n}(X_i - X_m)^2}{n-1}} \tag{B.2}$$

Where X_i is pressure difference for designated time frame for each repeated measurement, X_m is the arithmetic average of these pressure values and n is the repetition number which is 10 for coarse samples and 11 for fine samples. This standard deviation of reproducibility was calculated for both p_{rel} and p_{dif}. It should be noted that this statistical uncertainty of the measurement is based on the total amount of pressure changes measured by each sensor during entire measurement. However, it represents the uncertainty of transient pressure data points and any minor change in this uncertainty for transient points is for this data range and measurement frequency neglectable. In order to obtain total standard uncertainty, both measurement uncertainties should be in form of standard deviation of normal distribution. Systematic measurement uncertainty of the sensor given by the manufacturer has uniform distribution and can be transformed to standard uncertainty as follows:

$$u_{syst}(X) = \frac{Sensor\ Uncertainty}{\sqrt{3}} \tag{B.3}$$

Table B.2 Repeated measurements for porous concrete samples. (Pressure values in bar)

F1											
$p_{rel}\ (t = 5\ s)$	0.47457	0.4759	0.47502	0.47474	0.4755	0.4774	0.47584	0.47581	0.47586	0.47594	0.47448
$p_{rel}\ (t = 175\ s)$	0.00526	0.00595	0.00627	0.00585	0.00635	0.00673	0.00655	0.00679	0.00714	0.00745	0.00689
$p_{dif}\ (t = 5\ s)$	0.50075	0.50215	0.50204	0.50055	0.50142	0.50467	0.50202	0.50253	0.50232	0.5027	0.50198
$p_{dif}\ (t = 175\ s)$	0.03454	0.03507	0.03579	0.03548	0.0361	0.03699	0.03656	0.0371	0.03725	0.0378	0.03711
F2											
$p_{rel}\ (t = 5\ s)$	0.4755	0.47649	0.47575	0.47937	0.4794	0.47691	0.47955	0.47803	0.47621	0.47723	0.47744
$p_{rel}\ (t = 195\ s)$	0.00261	0.00339	0.00362	0.00428	0.00462	0.00484	0.00613	0.00637	0.00602	0.00589	0.00564
$p_{dif}\ (t = 5\ s)$	0.50284	0.50355	0.50398	0.50664	0.50751	0.50443	0.50695	0.50526	0.50453	0.5045	0.50485
$p_{dif}\ (t = 195\ s)$	0.03168	0.03217	0.0329	0.03372	0.03379	0.03405	0.0354	0.03565	0.03529	0.03493	0.03494
C1											
$p_{rel}\ (t = 5\ s)$	0.37835	0.37944	0.3789	0.3816	0.38067	0.38101	0.37925	0.37883	0.37781	0.37783	-
$p_{rel}\ (t = 30\ s)$	0.0282	0.02962	0.02942	0.02981	0.02996	0.02986	0.02943	0.02956	0.02946	0.02944	-
$p_{dif}\ (t = 5\ s)$	0.4025	0.40261	0.40176	0.4041	0.40501	0.40677	0.40196	0.40073	0.40122	0.40027	-
$p_{dif}\ (t = 30\ s)$	0.0549	0.05566	0.05551	0.05597	0.05624	0.05588	0.05535	0.05555	0.05519	0.05508	-
C2											
$p_{rel}\ (t = 5\ s)$	0.38479	0.39102	0.38728	0.39071	0.39352	0.3897	0.38932	0.39055	0.39515	0.38361	-
$p_{rel}\ (t = 30\ s)$	0.04827	0.05071	0.04916	0.05051	0.05159	0.04998	0.0499	0.04749	0.05148	0.04737	-
$p_{dif}\ (t = 5\ s)$	0.40776	0.41404	0.4119	0.4143	0.41673	0.41355	0.41249	0.41427	0.41809	0.40679	-
$p_{dif}\ (t = 30\ s)$	0.07421	0.07679	0.07524	0.0759	0.07783	0.07637	0.07617	0.07338	0.07773	0.07329	-

In this work, the total uncertainties of the measured values are evaluated for 95% confidence level, which corresponds to 1.98 times the total standard uncertainty. Table B.3 shows the total measurement uncertainty of each measured pressure for all samples as relative uncertainty ($u_c(X)/X$) with 95% confidence level.

Table B.3 Total measurement uncertainty (relative) of measured values for each sample.

	F1	F2	C1	C2
$u_c\left(p_{rel}\right)/p_{rel}$	±0.41%	±0.65%	±0.70%	±1.49%
$u_c\left(p_{dif}\right)/p_{dif}$	±0.46%	±0.64%	±1.05%	±1.49%

Propagation of Uncertainty (Error Propagation)

The uncertainty of a parameter Y that is depending on measured values $X_1, X_2, \dots, X_n$ can carry their uncertainties.

The commonly used simplified error propagation formula of independent measured values is as follows:

$$u_C(Y) = \sqrt{\left[\frac{\partial Y}{\partial X_1}u(X_1)\right]^2 + \left[\frac{\partial Y}{\partial X_2}u(X_2)\right]^2 + \left[\frac{\partial Y}{\partial X_n}u(X_n)\right]^2} \tag{B.4}$$

The parameters used for determining the permeability and passability, i.e. superficial velocity and pressure gradient, were evaluated from measured values of p_{rel} and p_{dif} respectively, which makes them dependent on these measured values.

Permeability k and passability η values determined in Chapter 4 are dependent on superficial velocity j and one-dimensional pressure gradient $\Delta p/h$ as given by Equation (2.7). The superficial velocity j (or the velocity v for the case of an empty pipe) depends on the measured p_{rel} values as given by Equations (4.4) and (4.5). The pressure gradient depends on the measured p_{dif} values as given by Equation (4.7). When these correlations are solved by Equation (B.4) the absolute and relative uncertainties for permeability and passability values for each sample are obtained. These values can be seen in Table B.4.

Table B.4 Relative and absolute uncertainty of determined permeability and passability of each sample based on the measurements.

	F1	F2	C1	C2
$u_c\ (k)/k$	±0.62%	±0.91%	±1.26%	±2.10%
$u_c\ (k)$	±1.30828x10^{-11} m^2	±1.72084x10^{-11} m^2	±5.15243x10^{-10} m^2	±1.25054x10^{-9} m^2
$u_c(\eta)/\eta$	±0.77%	±1.11%	±1.64%	±2.57%
$u_c(\eta)$	±6.34627x10^{-8} m^{-1}	±7.88929x10^{-8} m^{-1}	±3.01918x10^{-6} m^{-1}	±4.5176x10^{-6} m^{-1}

Appendix C: Drift Flux Models for Heavy Liquid from Literature to Determine the Void Fraction

As a part of the investigations performed in Chapter 5, an extensive literature survey was performed in order to find two-phase flow interfacial momentum exchange closure models that potentially could be used for two phase flow liquid corium and steam.

There are only very few models that are validated against heavy liquid-gas two phase flow experiments with material properties similar to that of liquid corium and steam. However, these experiments were performed in narrow pipes with very low gas velocities compared to bottom cooling conditions. Moreover, these models have void limitations introduced in them in order to fit to the experiment range they were developed for. All of these models are based on drift flux modelling with some adaptations in order to fit experiment geometry or boundary conditions.

Void fraction values calculated for melt and steam properties by stand-alone simulation program with drift velocity model by Mikityuk [83] and drift velocity model by Casan & Corradini [84] are shown on Figure C.1. Results for drift velocity model by Ishii, which was already presented in Chapter 5 can be seen on the figure for comparison as well. These two models are defined for the applicability range of $\alpha = 0.0 - 0.4$.This limitation can be clearly seen on the figure as well. The water flow range an final porosity range observed from CometPC experiments were indicated as a rectangular region on Figure C.1, and the models of Mikityuk and Casan & Corradini are overestimating the friction between the phases. Not only because of underestimating the friction forces, but also due to very specific applicability range of these and similar models from literature, they were not suitable for interfacial momentum transfer modelling of molten corium-steam two-phase flow

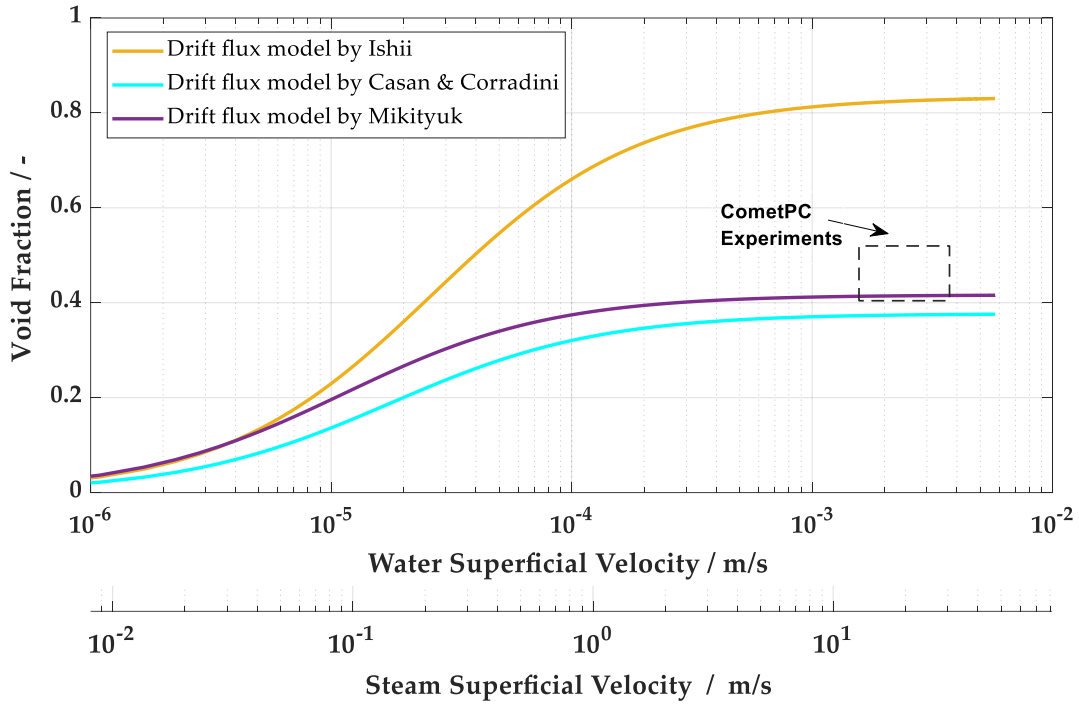

Figure C.1 Void fraction of liquid corium-steam two phase flow with drift flux models for Heavy Liquid by Casan & Corradini and by Mikityuk in comparison with drift flux model by Ishii. CometPC outcome range is indicated with dashed rectangular region.

Institut für Kernenergetik und
Energiesysteme

Universität Stuttgart
Pfaffenwaldring 31

D- 70569 Stuttgart